Electro Optical Circuit Architecture for Photonic Signal Processing

Abu Jahid

Thesis submitted in partial fulfillment of the requirements for the
Masters in Applied Science degree in Electrical and Computer Engineering

School of Electrical Engineering and Computer Science
Faculty of Engineering
University of Ottawa

Abstract

Microwave photonic applications in the terahertz (THz) region of the spectrum are attracting increasing attention due to the need to find solutions for next-generation (5G/6G) wireless communication systems capable of handling unprecedented data rates. It is crucial to develop millimeter-wave (mm-wave) (30-300GHz) fiber supported transport networks. One of the key questions is, which carrier frequency generation technique will be the most suitable for THz signals above 300 GHz; electronics-based or photonics-based. Since the backbone of the wireless networks is composed by very high-capacity fibre optic cables, the microwave photonic approach has the ultimate advantage of seamless integration with existing optical fibre networks. Although the cost effectiveness is still an open question, simplistic base station architecture with simplified antenna units and high optical component reuse is necessary for enabling a compatible mobile network backhaul. For THz applications a broadband electro-optic modulator (EOM) with a frequency response extending to the sub-terahertz range, high power handling, and very low nonlinear distortions, is required. The objective of this thesis is to study the feasibility of photonic integration and, proof of concept implementations with the effective use of optical components with reduced energy consumption, reduced footprint and offer speed beyond all-electronic implementations.

The first study presents a coherent electro-optic photonic integrated circuit deploying generalized Mach-Zehnder interferometer (GMZI) substituting $N\times1$ combiner by an optical $N\times N$ discrete Fourier transform (DFT) in order to generate a regularly spaced frequency comb. The proposed design comprises of 1×N splitter that feeds light into a parallel array of N electro-optic phase modulators electrically driven by RF signal with a progressive phase shift $\frac{2\pi}{N}$ with their phase modulated optical outputs processed by an $N\times N$ optical DFT. A pragmatic design approach and analytical formulation for implementing MMI based optical DFT in photonic networks composed of waveguide splitters, combiners, and phase-shift elements with necessary circuit diagram for even and odd dimensions are presented.

Recently, there has been impressive progress toward ultra-wide band low voltage EOM. The heterogeneous approach of utilizing silicon nitride on lithium niobate waveguide integrated on a single chip is demonstrated for the best optical modulation performance that opens a wide range of opportunities for universal linear optical networks, chip-scale MWP systems, ultra-speed switching of optical communications. Finally, the third study describes the architecture for compact on-chip spectrometry targeting high resolution across the entire C-band to measure the spectral profile of WDM signals reliably and accurately in fixed and flex-grid architectures. The design architecture of technologically viable compact on-chip high-resolution wideband spectrometer such as Mach-Zehnder delay interferometers (MZDI), 2×2 directional couplers and multimode interference couplers is presented and verified by software simulation using an industry standard tool. The components simulations that supported the assessment of the feasibility of a spectrometer compliant with the specification made use of the LioniX asymmetric double strip (ADS) waveguide and the low-cost photolithography.

Acknowledgements

First and foremost, my sincere gratitude goes to ALLAH, The Almighty God, the most Beneficent and Merciful. All praises are due to Him for giving His unlimited Mercy and Blessings throughout my MASc work.

I wish to express my heart-felt thanks and deepest appreciation to my supervisor, Professor Dr. Trevor J. Hall, for his excellent supervision, invaluable advice, insightful discussions, continuous skilled guidance, encouragement, and patience throughout this journey. Despite his busy schedule, he always managed to schedule a meeting when needed and I greatly value his uncomplaining proofreading and polishing of all my papers. Without his continuous guidance this thesis would not have been possible. He has been my motivation to strike hard in every challenge since I am working with him. I am lucky to work under such an extremely talented and knowledgeable person's supervision. A special appreciation goes to Peng Liu who has introduced me to the industrial environment and mentored me in exploring industry practices of photonic circuits, testing and measurements and I graciously acknowledge his contribution in enhancing my expertise. I also would like to thank all the members of PTLab for their constant effort to maintain a supportive workplace with friendly environment where I could work vigorously. Thank you to all the thesis examiners who have agreed to be part of the committee during this pandemic period.

Last but not the least, I want to express gratefulness to my parents and all family members for their selfless love, prayers and support for which I am being able to pursue my aspirations diligently.

Table of Contents

Abstract ii
Acknowledgements iii
Table of Contents iv
List of Tables vi
List of Figures vii
List of Acronyms ix

Chapter 1. Introduction

1.1 Background and motivation 1
1.2 Objectives 3
1.3 Structure of the Thesis 3

Chapter 2. Advances in Integrated Heterogeneous Electro-Optic Modulator

2.1 Introduction 5
2.2 Theory 5
2.3 Operations of Optical DFT Network 8
2.4 Realization of DFT Using MMI Coupler 12
2.5 Simulation Results and Verification 18
2.6 Summary 21

Chapter 3. Generalized RF Photonic Integrated Circuit Architecture

3.1 Introduction 21
3.2 Theory 21
3.3 Literature Review 24
3.4 Electro Optic (EO) Modulation 26
3.4.1 Evolution of LN EO Modulators 27
3.4.2 Phase Shifter in Integrated LN Modulators 28
3.4.3 MZI Design in Integrated LN Modulators 29
3.5 Simulation Results 30
3.6 Research Opportunities and Roadmap 31
3.7 Summary 32

Chapter 4. High Resolution Panoramic C band on-chip Spectrometer

4.1 Introduction ……... 35
4.2 Theory …… 36
4.3 Spectrometer Circuit Architecture ……. 37
4.4 Integration Platform ……... 39
4.5 Technological Validation & Integration Feasibility …….. 39
4.6 Directional Coupler and MMI Coupler ……. 43
4.7 Simulation Results ……. 46
4.8 Layout …… 47
4.8.1 Die Templates ……. 48
4.8.2 Mask Cross-sections …… 49
4.8.3 Design Rule Checks ……. 50
4.9 LioniX ADS PDK Modeling ……. 51
4.9.1 Waveguides ……. 51
4.9.2 Phase Modulators …… 51
4.9.3 Heater Lead ……. 51
4.9.4 Splitters and Couplers ……. 51
4.10 Summary …… 53

Chapter 5. Conclusions

5.1 Summary & Conclusions …….. 54
5.2 Future Scope …….. 56

Appendix I. MMI DFT Equivalence ……... 57
Appendix II. Script for the Complete Spectrometer Circuit Design Layout …….. 67

Bibliography …… 90

List of Tables

Table 3.1: Material property of AlN for photonics integrated circuit …….. 27

Table 4.1. Detail design specifications of the proposed circuit architecture ….. 40

Table 4.2: Optimum design specifications for 3dB MMI couplers ……. 46

List of Figures

Figure 2.1 Schematic diagram of 1×*N* splitter and *N*×*N* DFT composed of *N* parallel phase modulators …… 8
Figure 2.2 Schematic diagram of 8×8 DFT coupler comprised of 2×2 and 4×4 DFT network …… 11
Figure 2.3 Realization of 2×2 DFT using 2×2 MMI …….. 13
Figure 2.4 Realization of 4×4 DFT using 4×4 MMI …….. 14
Figure 2.5 8×8 optical DFT network; (a) Realization of 8×8 DFT using 8×8 MMI (b) Simplified architecture of 8×8 optical DFT network without crossover 15
Figure 2.6 Schematic diagram for monitoring the output optical spectrum using OSA of 1 GHz resolution bandwidth …… 16
Figure 2.7 Realization of 3×3 DFT using 3×3 MMI ……... 17
Figure 2.8 Simulated optical spectrum of 8×8 DFT without MMI errors ……... 18
Figure 2.9 Simulated optical spectrum of 8×8 DFT with MMI design errors … 19
Figure 2.10 Optical SHSR as a function of RF drive's phase errors between the MZMs for 8×8 MMI …… 20

Fig. 3.1 Thin Flim Litium Niobate devices and cross-sectional views ……... 27
Figure 3.2 Hybrid TFLN optical modulator …… 29
Figure 3.3 Comparison of core thickness without ridge under different boundary conditions (BC) …… 30
Figure 3.4 Impact of ridge width on TE mode, mode loss and confinement factor under different BC …… 30
Figure 3.5 Mode loss vs core thickness …… 30
Figure 3.6 Percentage of TE mode vs core thickness …….. 30
Figure 3.7 Effect of bending loss with curvature …..……. 31
Figure 3.8 Percentage of TE mode varying core thickness …… 31
Figure 3.9 Mode loss vs ridge thickness ……..... 31
Figure 3.10 Confinement factor with ridge thickness …….. 31
Figure 3.11 Mode loss vs radius of curvature …… 32
Figure 3.12 Simulated mode confinement factor in LiNbO3 as a function of Si3N4 strip width and LN film thickness for the fundamental TE mode …… 32
Figure 3.13 TFLN hybrid modulator optical waveguide ……. 32
Figure 3.14 TFLN layout in FIMMWAVE ……. 32
Figure 3.15 Intensity mode profile of given TFNL hybrid modulator …… 32

Figure 4.1 Illustration of the spectrometer 38
Figure 4.2: (a) Tunable Ring Resonator, AWG and DSP; (b) Tracking of RR comb (grey arrows) & AWG output (peaked curves) ……. 38

Figure 4.3 Definition of the cross-sectional parameters of ADS waveguide. The thicknesses of lower strip, the gap and the upper strip are 75 nm, 100 nm and 175 nm, respectively. The black area is Si (silicon) substrate while the yellow area (cladding) is SiO_2 (silica) and red parts (cores) are Si_3N_4 (silicon nitride)… 40
Figure 4.4 (a) Schematic diagram of a RR; (b) power coupling between the ports of a directional coupler as a function of spatial separation; (c) zoom-in view of the power coupling at the cross port as a function of spatial separation…….. 41
Figure 4.5 Group index of fundamental TE-like mode versus wavelength over the C-band ……. 42
Figure 4.6 Schematic of basic directional coupler …….. 43
Figure 4.7 A schematic of 3dB coupler covering the c-band for ADS waveguide 44
Figure 4.8 Splitting ratio of a 50:50 directional coupler versus wavelength for ADS waveguides and TE polarisation ……. 44
Fig. 4.9 Splitting ratio of the straight section of a 3dB directional coupler versus vacuum wavelength over the c-band for ADS waveguides and TE polarisation… 45
Figure 4.10 Optical intensity profile for MMI couplers…… 45
Figure 4.11 VPI schematic of a spectrometer circuit architecture ……..... 46
Figure 4:12 (a) Power splitting of a 3 dB DC scanning the C-band for ADS waveguides; (b-c) power splitting ratio of a DC. ……. 46
Figure 4.13 A simulation of the proposed spectrometer circuit. (a) Upper MZDI selected phase of scanning cycle; (b) lower MZDI selected phase of scanning cycle; (c) full scanning cycle …… 47
Figure 4.14 Wafer map showing the place of the blocks on the wafer; outside the blocks alignment marks is added. Inside each block, a process control features set (pcf) is placed on a suitable place ……. 48
Figure: 4.15 16 mm × 16 mm die template ……. 49
Figure 4.16 Cross-Section of the LioniX International TriPleX Asymmetric double-stripe waveguide with a silicon nitride core and silicon oxide cladding… 50
Figure 4.17 Fitting the PIC layout into die template …… 51
Figure 4.18 A complete layout for a single component …… 52
Figure 4.19 A complete GDSII layout ……. 53

List of Acronyms

ADS	Asymmetric Double Strip
AlN	Aluminum Nitride
AWG	Arrayed Waveguide Gratings
BER	Bit Error Rate
CMOS	Complementary Metal-Oxide-Semiconductor
CW	Continuous Wave
DFT	Discrete-Fourier Transform
DRC	Design Rule Checking
EOM	Electro-optic Modulator
EON	Elastic Optical Network
FSR	Free Spectral Range
FWHM	Full Width Half Maximum
GMZI	Generalized Mach-Zehnder Interferometer
LNOI	Lithium Niobate-on-Insulator
MEMS	Micro Electro Mechanical Systems
MMI	Multimode Interference
mmWave	Millimeter wave
MPW	Multi Project Wafer
MWP	Microwave Photonics
MZDI	Mach-Zehnder Delay Interferometer
MZM	Mach–Zehnder Modulator
OFDM	Orthogonal Frequency Division Multiplexing
OPM	Optical Performance Monitoring
OSA	Optical Spectrum Analyzer
PD	Photodetector
PDK	Process Development Kit
PIC	Photonic Integrated Circuit
PM	Phase Modulator
ROADM	Reconfigurable add-drop Multiplexer
RR	Ring Resonator
SDN	Software Defined Networking
SN	Silicon Nitride
SOI	Silicon-on-Insulator
SSC	Spot Size Convertors
TE	Transverse Electric
TFNL	Thin-film Lithium Niobate
TM	Transverse Magnetic
TO	Thermo-optic
WDM	Wavelength-Division Multiplexing

CHAPTER 1

Introduction

1.1 Background and motivation

Over decades and across all levels of optical networks, the global internet traffic has experienced continuous growth at an enormous rate [1]. The ever-increasing data traffic and super broadband services such as high-definition video streaming, high-speed internet, video calling, cloud computing and Internet of things (IoT) have revolutionized the telecommunication network framework. Fiber communication has already been manifested as a future-proof infrastructure to provide wideband, high frequency, low loss, low cost, longer reach and interference immune signal distribution [2]. The wireless mobile consumers also demand high-speed operation alongside the flexibility of the mobility of transponder and broadcasting capabilities to realize ubiquitous connectivity. Consequently, present wireless local networks must provide increased transmission capacity while maintaining sufficient coverage [3]. The industry now talks of Pbit/s capacity optical networks. The first concern of industry is the cost of hardware, yet energy consumption has risen to second place, and the key to both cost and energy reduction is photonic integration. To meet this ever-increasing demand, digital coherent transmission technology was invented for long-haul communication links, allowing networks to approach the Shannon limit, which is the highest feasible capacity of optical fibers. [4] [5]. This technique is projected to make inroads into the quickly developing, capacity-hungry short-range links, such as metro and data-center interconnects, where an in-phase/quadrature (IQ) modulator must operate in a small space with low loss, low drive voltages, and huge bandwidths.

The ever-growing data traffic and super broadband services demanded by the end users have led the wireless communication network to undergo rapid development in terms of capacity, bandwidth, cost and mobility. 5G wireless and optical communications are converging in terms of technology and methods. Spectrally efficient advanced modulation formats long used in wireless to relieve a crowded RF spectrum are now being used in coherent optical communications systems to relieve what has now become a similarly crowded optical spectrum. RF photonic systems have been implemented until recently using fiber-coupled discrete components but considerations of stability, compactness, and cost calls for integrated photonics.

An estimated 5.1 billion people are using internet in 2021, which reflects the yearly average growth of 10% of the internet users [6]. Tremendous Internet growth due to technological advancement and competition among operators and the consequent demand for high speed applications are calling for high transmission capacity with sufficient coverage area butut the mobility offered by the mobile broadband services adds the choice of flexibility. That is why, while the fixed broadband subscriptions have continued to grow at a modest rate, a year-on-year growth rate of 18.4% has been observed for mobile broadband subscription [6].

As a result of the transition from incoherent to coherent optical systems, a revolution in optical and wireless communication technologies is underway. Meshes of Mach–Zehnder interferometers could be used to perform a variety of advanced optical functions, including fundamental quantum technology testing and arbitrary linear optical processors for communications [7]. The fundamental challenge of implementing MachZehnder interferometer (MZI) based optical processors for communications within a coherent optical framework is phase controlling in a complex circuit architecture due to extreme short wavelength of light. As a consequence, the system performance is substantially degraded by a little imperfection of optical components. With the evolution of optical component technology, optical fiber can be interconnected to integrated elements through planner optical waveguide in a photonic integrated circuit platform. The advancement of tight path length tolerance and component symmetries enables circuit designers to develop robust photonic integrated circuit which is impractical with discrete components.

An optical switching matrix with a rapid switching speed, wide bandwidth, non-blocking throughput, low crosstalk, and low loss is in high demand due to the exponential development of traffic in telecommunications, the Internet, data centers, and the Internet of Things. An optical modulator is a key building block for photonic integrated circuits (PICs) because it has a wide range of applications in both analog and digital systems, including on-chip RF photonics, telecommunication networks, passive millimeter wave imaging systems, data communication, high-speed signal processing, frequency comb generation, and quantum information processing. The ability to directly integrate lithium niobate (LN) and silicon nitride (SN) with photonic platforms based on silicon nitride waveguides with oxide cladding opens up a slew of new possibilities for chip-scale microwave photonics (MWP) systems, optical communications switch networks, universal linear optical networks, and nonlinear photonics. Furthermore, the hybrid approach of utilizing LN on SN waveguide platform enables important new applications such as modulators, frequency conversions that require picosecond class wavelength tuning speeds on dense wavelength division multiplexing grids under 100 GHz, faster optical modulators (above 100 gigabauds), picosecond class photonic space switching, and all-photonic processing for artificial intelligence and quantum computing.

The ability to configure network functions, protocols, and make optimal use of spectrum is made possible by monitoring the state of the optical network. Up-to-date network telemetry is required for capacity scaling, network or component fault recovery, and network reconfiguration through performance prediction and planning. An integrated solution for a high resolution (sub-GHz) spectrometer to monitor the power in fixed- and flex-grid architectures across the entire C band 1530 nm to 1565 nm remains challenging. A variety of different approaches to the problem of spectral sensing with high resolution across a wide band have been disclosed but when scaled to combine acceptable resolution with wideband operation their practical implementation is most often not feasible due to excessive cost, loss and footprint. This research focused on photonic circuits and subsystems that leverage continued advances in photonic integrated circuits including hybrid integration of active optoelectronic, electro-optic, and electronic devices.

1.2 Objectives

The aim of this thesis is to explore the advanced photonics system architectures that offer ultra-speed beyond all-electronic implementations, substantially reduced energy consumption, and/or reduced footprint with the potential for commercialization. The focus of this work is on designing coherent EO circuits for photonics applications, validating their theoretical functionalities through industry standard software tools and analyzing feasibility check for integrated implementation. The specific objectives are:

- To develop all optical digital filtering device for next generation optical communications and microwave-photonics (MWP) functions.
- To demonstrate the heterogeneous approach of utilizing silicon nitride on lithium niobate waveguide integrated on a single chip for chip-scale MWP systems, universal linear optical networks, ultra high-speed switching of optical communications.
- To develop the design of a commercially viable compact on-chip high-resolution wideband optical spectrometer to measure the spectral profile of WDM signals over C-band.

1.3 Structure of the Thesis

The thesis has been structured into five chapters to demonstrate the research objectives mentioned above.

Chapter 1 describes the motivation and the background of the research addressing the potential challenges of the previous work done in the topics. This chapter also summarizes the key objectives of the thesis.

Chapter 2 presents a coherent electro-optic photonic integrated circuit deploying generalized Mach-Zehnder interferometer (GMZI) substituting $N\times1$ combiner by an optical $N\times N$ discrete Fourier transform (DFT) in order to perform a regularly spaced frequency comb. A generalized transfer matrix scheme is applied to model the envisioned framework which is examined by simulation results contemplated an industry approved standard software tool. With the potential benefits of component and circuit symmetries and tight optical path length control, the proposed architecture has the potential to eliminate the presence of optical de-multiplexing filter at the output of an optical comb generator and can be easily integrated in any material platform. The proposed architecture is demonstrated for both even and odd dimensions of MMI configurations which has no restriction on the number of inputs.

Chapter 3 discusses the recent advancements heterogeneous approach of hybrid silicon nitride on lithium niobate waveguide modulator integrated on a single chip for universal optical networks. This chapter focused on the implementation challenges, mitigation approaches, and plausible future research scopes.

Chapter 4 outlines the architecture of small on-chip spectrometry targeting high resolution over the full C-band to analyze the spectral profile of WDM signals reliably and precisely in fixed and flex-grid topologies. The components simulations that supported the assessment of the feasibility of a spectrometer compliant with the specification made use of the LioniX asymmetric double strip (ADS) waveguide. The fabrication expected access to multi-project wafer MPW runs for test structures, followed by a custom wafer run for fabrication of prototypes for demonstration, in order to make efficient use of resources.

Chapter 5 summarizes the findings in the thesis, makes conclusions and offers recommendations for further work.

FIMMWAVE/FIMMPROP (Photon Design), VPI Photonics, OptiSim, Opti BPM, Opto Designer (Synopsys), Klayout, Rsoft software are used to simulate all the considerations throughout the thesis. It sets the industry standard for software and services supporting end-to-end Photonic Design Automation (PDA) and Optical Equipment Configuration (OEC). It enables modeling multiscale integrated circuits with lengths of photonic components ranging from a few microns to several centimeters on the same chip. These software offers dynamic models of active, dynamically tunable, advanced wide-spectrum, and passive elements such as semiconductor lasers and LEDs, modulators, switches, delay lines, detectors, directional couplers, filters, branches, MMIs, ring resonators, star couplers, and waveguides. These can be interconnected in any permutation to design devices and photonic circuits. The spectral dynamics of laser sources and semiconductor optical amplifiers, careful modeling of external optical modulators and their electronic drive circuitries is important to characterize photonic circuits presented in this thesis with respect to large signal dynamics, noise characteristics, side-mode suppression, tuning behavior, and modulation response.

CHAPTER 2

Generalized RF Photonic Integrated Circuit Architecture

2.1 Introduction

There has been a number of publications over the last decade are carried out in the context of electro-optic circuit architectures for RF signal generation. This chapter presents a coherent electro-optic photonic integrated circuit deploying generalized Mach-Zehnder interferometer (GMZI) substituting $N\times1$ combiner by an optical $N\times N$ discrete Fourier transform (DFT) in order to generate a produce spaced frequency comb. A generalized transfer matrix scheme is applied to design the envisioned framework which is examined by using an industry approved standard software tool. Provisioning of N spatially separated phase correlated subcarriers for all OFDM technique offers terabit data demands through providing multi-carriers for augmented transmission in the context of microwave photonic applications. The architecture subsumes all MZI-based architectures in the prior art given an appropriate selection of output port(s) and dimension *N,* although the principal application envisaged is phase-correlated subcarrier generation for next-generation optical transmission systems. For example, the simulation of a 4×4 DFT realized by a combination of 180˚ optical hybrids implemented as 2×2 MMI couplers. A novel extension of the proposed circuit architecture is also presented, by choosing the 3×3 optical Discrete Fourier Transform (DFT) network using a combination of a properly chosen phase shifters and a single 3×3 MMI coupler. With the added benefits of component and circuit symmetries and tight optical path length control, the proposed architecture has the potential to eliminate the presence of optical de-multiplexing filter at the output of an optical comb generator and can be easily integrated in any material platform that exhibits linear electro-optic phase modulation effect such as lithium niobate, III-V or hybrid structure. The proposed architecture is demonstrated for both even and odd dimensions of MMI configurations which has no restriction on the number of inputs. Based on the output ports and circuit dimension (N), the proposed circuit architecture can be employed for frequency conversion, frequency multiplication, SSB modulation, and phase correlated subcarrier creation. For experimental confirmation, an integrated circuit based on silicon photonics technology that is readily available in the lab is used.

2.2 Theory

To tackle the ever-increasing demand in transmission capacity due to diverse type of ultrafast applications, the paradigm of high-speed optical coherent deployment has drawn intensive attention nowadays in the context of optical communication system. Optical orthogonal frequency division multiplexing (OFDM) based coherent optical communication is one of the promising candidates for realizing high spectral efficiency, and large-capacity system through multiplexing multiple orthogonally subcarriers in optical domain. The coherent optical OFDM (CO-OFDM) can be scaled terabit transmission speed by envisioning number of orthogonal subcarriers and

adaptive modulation scheme. In addition, CO-OFDM technique has the potential of large tolerance to fiber impairments generated by polarization mode dispersion and chromatic dispersion [8], [9]. The transmission capacity is considerably reduced by the data rate and energy consumption of signal processing unit as well as analog-to-digital conversion (ADC) unit. However, many approaches predominantly depend on signal processing devices which leads to a bottleneck to augmented lower cost implementation providing higher capacity [8]. The real-time single carrier capacity of OFDM transmitter has difficulty to reach terabit speed [10].

Over the past few decades, several research works have been carried out to describe the applications of MZI based RF photonic circuits in the field of microwave communications [11]–[14]. Authors proposed [11] a simple circuit design approach comprises of N-parallel phase modulators driven with 2π/N incremental phase shifts for eliminating unwanted harmonics. The phase relations between the ports of MMI couplers is presented in the literature [15] to incorporate the static optical phase shift for these circuits, thereby restricting the use of static DC-bias supply to the electrooptic (EO) modulators and the corresponding adverse drift issues. The fundamental challenge of implementing MachZehnder interferometer (MZI) based optical processors for communications within a coherent optical framework is phase controlling in a complex circuit architecture due to extreme short wavelength of light. As a consequence, the system performance is substantially degraded by a little imperfection of optical components [16], [17]. With the evolution of optical component technology, optical fiber can be interconnected to integrated elements through planner optical waveguide in a photonic integrated circuit platform. The advancement of tight path length tolerance and component symmetries enables circuit designers to develop robust photonic integrated circuit which is impractical with discrete components [18].

The realization of MZI based RF photonic circuits using optical DFT network has been pointed out on the subject of microwave photonics [19]. In order to achieve high speed data rate and spectral efficiency, a multi-carrier transmission format such as OFDM technique is required over a single carrier modulation scheme. The envisioned design objective is to generate *N* sub channels for modern optical transmission systems contemplating all optical domain OFDM technique aiming to achieve terabit data speed. The fundamental limitation of OFDM based broadband optical communications is the impediment to process the OFDM signals all optically. An integrated photonic device enabling to multiplex modulated OFDM signals in optical domain composed of inverse fast Fourier transform (IFFT) is demonstrated in [20]. The key limitation of studies [20], [21] is that all the generated subcarriers from the optical comb source are extracted from the same output port. Therefore, an optical demultiplexer (DMUX) is required to filter the subcarriers generated from the same output port for modulation. Owing to the temperature sensitivity and short tuning range of optical DMUX filter, the system performance is significantly deteriorated in conjunction with complicated design architecture. However, the concept of complementary phase shifter is introduced in [22] as a solution of the aforementioned restrictions, but this design can only produce two subcarriers which is insufficient to tackle the enormous growth of data demand.

As an indication of these limitations, the realization of optical DFT device functioning all optically is inevitably promising. The development of DFT network is essential to filter OFDM signals in optical domain as well as overcome the electrical switching speed and minimizing power dissipation. However, the deployment of traditional bandpass filtering for demultiplexing these sub-channels results in high optical signal-to-noise ratio (OSNR) penalty because of their overlapping spectra and thereby instigate of endeavoring DFT filters. The first study of an optical DFT used as the combiner of generalized MZI (GMZI) is pointed out in the literature [23] to overcome this barrier. According to [23], a universal subcarrier generation methodology is explicitly demonstrated to perform an Nth order optical DFT using an all optical OFDM (AO-OFDM) technique. The design of 4×4 DFT using 2×2 3dB MMI couplers is clearly illustrated with the analytical approach. Authors in [24] reported the design architecture of 4×4 DFT network using a 4×4 MMI coupler with necessary phase shifters.

Author in [25] reported a planner lightwave circuit (PLC) OFDM demultiplexer consisting of a 4×4 MMI based DFT circuit and following to the design architecture, adaptive dispersion control characteristics with phase change of phase shifters is studied in [26]. It's become a challenging design issue of higher order DFT, size and minimization of fabrication errors while implementing DFT circuit scalability. An optical demultiplexer for channels separation in OFDM systems is used to perform DFT operation as an alternative option of the conventional bandpass filter proposition illustrated in [8]. However, the DFT operations is performed by suitable adjustment of delay lines, phase shifters on delay lines and MMI couplers. Rahim *et. al.* [8] investigated the design of scalable DFT network comprising a cascaded operations of two and four ports GMZI using M-ports MMI couplers. The 300 GHz free spectral range (FSR) of the filter is modeled to demultiplex 8 OFDM sub-channels to achieve 1.2 Tb/s bit rate.

Following to the work [8], Rahim *et. al.* in [27] designed a 16 channel DFT filter using multistage cascaded 4×4 MMI couplers in the context of silicon photonics, but the performance of only a single port is shown to demonstrate its feasibility. Reference [28] proposed a design architecture of 8-channel demultiplexer comprising of cascaded 2×2 and 4×4 MMI couplers, delay lines and phase shifters. Zhou [29] presented a 16×16 MMI that is used to realize the 8x8 DFT. However, phase errors in the delay lines due to fabrication process or imprecise adjustment of the phase shifters leads to inter-cell interference (ICI) since the subcarriers do not follow the orthogonality. The prime objective of this report is to analyze a coherent EO circuit design using GMZI that generates N spatially distinct phase correlated subcarriers harmonically where $N\times N$ optical DFT replaces its $N\times 1$ combiner. In particular, this study presents a novel extension of a generalized photonic integrated circuit architecture incorporating a single $N\times N$ MMI coupler to implement $N\times N$ DFT of even configurations (i.e., even input ports and even output ports) and odd configurations also. For example, a 8×8 MMI coupler with suitable phase shifters represents the conventional 8×8 optical DFT network.

The proposed circuit consist of N parallel electro-optic phase modulators driven by the same RF source with a progressive phase shift of $\frac{2\pi}{N}$; optical feeds from a $1\times N$ splitter and terminated by a

$N \times N$ optical DFT network. Owing to the generation of N spatially disjoint phase correlated subcarriers, the proposed circuit architecture can be implemented in multi-carrier transmission while satisfying terabit data rate demands anticipated in practice. In addition, the mathematical formulation of MMI-DFT equivalence and the circuit design approach of higher order discrete Fourier optics circuit is illustrated employing a generalized form of MMI coupler. The proposed circuit architecture operates with carriers frequency shift of $q\Omega$ (where angular frequency Ω in Hz) emitted from output port q module N as evident from the transfer matrix analysis. Thereafter, the analytical model is validated by simulation under the presence of practical impairments. As a consequence of the validation of theoretical derivation by the numerical simulation, a precise DFT can be realized evidently. This device has the potential to allow digital filtering in optically and enables the easy integration of all optical OFDM transmission systems.

2.3 Operations of Optical DFT Network

Discrete Fourier Transform (DFT) has been considered as a vital technology for signal processing in OFDM communication systems. It is widely believed that an optical DFT can be implemented through an appropriate combination of waveguides and couplers.

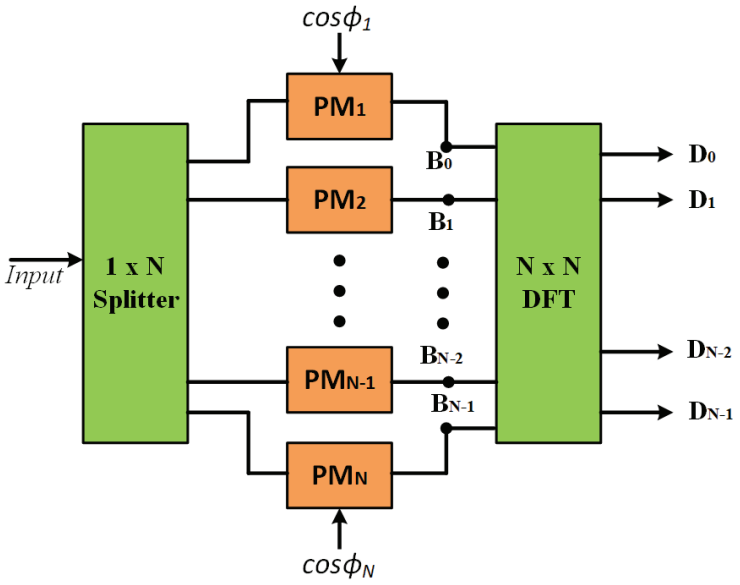

Figure 2.1: Schematic diagram of splitter and DFT composed of an array of N parallel phase modulators.

There are several approaches to realize the optical DFT, such as use of star couplers, planner lightwave circuits (PLC), and MMI couplers [30], [31]. The optical DFT filter can pass a set of discrete amplitudes through optical waveguides or a single mode fiber network. In this approach, a set of discrete arrays of coherent optical input amplitudes are applied into an integrated optical network and the discrete signal is taken through N identical output fibers. A decomposition into $log_2 N$ stages of $M \times M$ DFT hybrid ($2 < M \leq N$) approach that are realized by $(360/M)^o$ is proposed in [32] aiming to reduce the number of required waveguide cross-overs and phase shifters. The

operations DFT networks can be contemplated using star couplers [33], static phase shift elements assisted MMI couplers [29] and a mesh of MZI including any linear transformation [18]. Note that MMI coupler based optical DFT has less complex structure and much easier for integration in comparison with other approaches. Low power requirements, small footprint, coping to the transmission data rate inspired to ameliorate photonic integrated circuit delivering DFT operation based on MMI couplers [25], optical delay interferometers [28], [34] and Arrayed Waveguide Gratings (AWGs) [35]. However, these works suffer lack of scalability towards higher order of DFT circuit as it requires large number of coupling elements including phase error effects.

The general circuit architecture depicted in Fig. 2.1 consisting of a 1×N uniform optical splitter that excites N parallel EO waveguide phase modulators whose outputs collected together by a passive coherent optical N×N DFT networks. The light emitted at the final output stage with complex amplitude can be denoted as d_q. The separation of N OFDM sub-channels d_0 to d_{N-1} can be expressed as by applying a discrete Fourier transformation:

$$d_q = \frac{1}{\sqrt{N}} \sum_{p=0}^{N-1} b_p e^{-ipq\frac{2\pi}{N}}, \qquad q = 0, 1, ..., N-1 \tag{2.1}$$

where b_p is the complex amplitudes of incoming light to the optical DFT ports, p and q are integers that identifies ports index.

Assume an external RF source drive each phase modulator (PM) with a phase shift of $\frac{2\pi}{N}$-can be expressed as:

$$V_p = V_{RF} cos[\Omega t + p(2\pi/N)] \tag{2.2}$$

where Ω is the angular frequency of RF supply.

On the other hand, the output light of PMs with a complex amplitude b_p can be defined as:

$$b_p = \frac{1}{\sqrt{N}} e^{i\pi\frac{v_p}{v_\pi}} \tag{2.3}$$

where v_π is the half-wave voltage. According to the Jacobi-Angier expansion:

$$e^{i\gamma cos\theta} = \sum_{q=-\infty}^{\infty} i^q J_q(\gamma) e^{iq\theta} \tag{2.4}$$

where $\gamma = \pi\frac{v_{RF}}{v_\pi}$ denotes the peak optical phase shift. Invoking Eq. (1), (3) and (4), we obtain:

$$d_q = \frac{1}{\sqrt{N}} \sum_{p=0}^{N-1} \sum_{m=-\infty}^{\infty} i^m J_m(\gamma) e^{im\Omega t} e^{ip(m-q)2\pi/N} \tag{2.5}$$

Re-ordering the summations to give:

$$d_q = \sum_{m=-\infty}^{\infty} i^m J_m(\gamma) e^{im\Omega t} \frac{1}{\sqrt{N}} \sum_{p=0}^{N-1} e^{i(m-q)2p\pi/N} \tag{2.6}$$

Noting that

$$\frac{1}{\sqrt{N}}\sum_{p=0}^{N-1} e^{i(m-q)2p\pi/N} = 0, \qquad m \neq q, \quad mod \;\; N$$
$$\frac{1}{\sqrt{N}}\sum_{p=0}^{N-1} e^{i(m-q)2p\pi/N} = 1, \qquad m = q, \quad mod \;\; N \tag{2.7}$$

Finally, Eq. (6) can be written as follows:

$$d_q = \sum_{r=-\infty}^{\infty} i^{(q+rN)} J_{(q+rN)}(\gamma) e^{i(q+rN)\Omega t} \tag{2.8}$$

It can be observed that all the harmonic orders equivalent modulo *N* to the output port number q exit that port. The operation of circuit architecture presented in Fig. 2.1 offers many applications pertaining to a suitable choice of exit ports and dimension (*N*) of phase modulators, for example, RF multiplication [36], single sideband modulation (SSB) [37], in phase and quadrature phase (IQ) modulation [22], [38], electro-optic frequency conversion [15], [39], [40], and spatially separated frequency comb generation [23].

For example, a 8×8 DFT coupler network is desired with a transmission matrix given by:

$$D_{88} = \frac{1}{\sqrt{8}} \begin{bmatrix} z^0 & z^0 & z^0 & z^0 & z^0 & z^0 & z^0 & z^0 \\ z^0 & z^1 & z^2 & z^3 & z^4 & z^5 & z^6 & z^7 \\ z^0 & z^2 & z^4 & z^6 & z^8 & z^{10} & z^{12} & z^{14} \\ z^0 & z^3 & z^6 & z^9 & z^{12} & z^{15} & z^{18} & z^{21} \\ z^0 & z^4 & z^8 & z^{12} & z^{16} & z^{20} & z^{24} & z^{28} \\ z^0 & z^5 & z^{10} & z^{15} & z^{20} & z^{25} & z^{30} & z^{35} \\ z^0 & z^6 & z^{12} & z^{18} & z^{24} & z^{30} & z^{36} & z^{42} \\ z^0 & z^7 & z^{14} & z^{21} & z^{28} & z^{35} & z^{42} & z^{49} \end{bmatrix}$$

where $z = exp(\pm i\frac{2\pi}{8})$. This may be rewritten as:

$$D_{88} = \frac{1}{\sqrt{8}} \begin{bmatrix} (z^2)^0 & (z^2)^0 & (z^2)^0 & (z^2)^0 & (z^2)^0 & (z^2)^0 & (z^2)^0 & (z^2)^0 \\ (z^2)^0 z^0 & (z^2)^0 z^1 & (z^2)^0 z^2 & (z^2)^0 z^3 & (z^2)^0 z^4 & (z^2)^0 z^5 & (z^2)^0 z^6 & (z^2)^0 z^7 \\ (z^2)^0 & (z^2)^1 & (z^2)^2 & (z^2)^3 & (z^2)^0 & (z^2)^1 & (z^2)^2 & (z^2)^3 \\ (z^2)^0 z^0 & (z^2)^1 z^1 & (z^2)^2 z^2 & (z^2)^3 z^3 & (z^2)^0 z^4 & (z^2)^1 z^5 & (z^2)^2 z^6 & (z^2)^3 z^7 \\ (z^2)^0 & (z^2)^2 & (z^2)^4 & (z^2)^6 & (z^2)^0 & (z^2)^2 & (z^2)^4 & (z^2)^6 \\ (z^2)^0 z^0 & (z^2)^2 z^1 & (z^2)^4 z^2 & (z^2)^6 z^3 & (z^2)^0 z^4 & (z^2)^2 z^5 & (z^2)^4 z^6 & (z^2)^{14} z^7 \\ (z^2)^0 & (z^2)^3 & (z^2)^6 & (z^2)^9 & (z^2)^0 & (z^2)^3 & (z^2)^6 & (z^2)^9 \\ (z^2)^0 z^0 & (z^2)^3 z^1 & (z^2)^6 z^2 & (z^2)^9 z^3 & (z^2)^0 z^4 & (z^2)^3 z^5 & (z^2)^6 z^6 & (z^2)^9 z^7 \end{bmatrix}$$

Note that 4×4 DFT coupler network can be extracted from the aforementioned transfer matrix

$$\frac{1}{\sqrt{8}} \begin{bmatrix} (z^2)^0 & (z^2)^0 & (z^2)^0 & (z^2)^0 \\ (z^2)^0 & (z^2)^1 & (z^2)^2 & (z^2)^3 \\ (z^2)^0 & (z^2)^2 & (z^2)^4 & (z^2)^6 \\ (z^2)^0 & (z^2)^3 & (z^2)^6 & (z^2)^9 \end{bmatrix} \equiv \frac{1}{\sqrt{2}} D_{44}$$

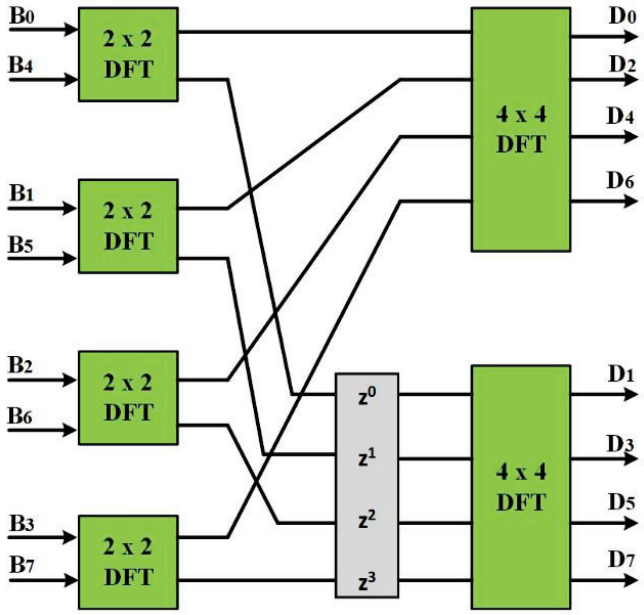

Figure 2.2: Schematic diagram of 8×8 DFT coupler comprised of 2×2 and 4×4 DFT network.

$$\frac{1}{\sqrt{8}}\begin{bmatrix}(z^2)^0z^0 & (z^2)^0z^1 & (z^2)^0z^2 & (z^2)^0z^3\\ (z^2)^0z^0 & (z^2)^1z^1 & (z^2)^2z^2 & (z^2)^3z^3\\ (z^2)^0z^0 & (z^2)^2z^1 & (z^2)^4z^2 & (z^2)^6z^3\\ (z^2)^0z^0 & (z^2)^3z^1 & (z^2)^6z^2 & (z^2)^9z^3\end{bmatrix} = \frac{1}{\sqrt{8}}\begin{bmatrix}(z^2)^0 & (z^2)^0 & (z^2)^0 & (z^2)^0\\ (z^2)^0 & (z^2)^1 & (z^2)^2 & (z^2)^3\\ (z^2)^0 & (z^2)^2 & (z^2)^4 & (z^2)^6\\ (z^2)^0 & (z^2)^3 & (z^2)^6 & (z^2)^9\end{bmatrix}\begin{bmatrix}z^0 & 0 & 0 & 0\\ 0 & z^1 & 0 & 0\\ 0 & 0 & z^2 & 0\\ 0 & 0 & 0 & z^3\end{bmatrix}$$

$$\equiv \tfrac{1}{\sqrt{2}}\ D_{44}\,\text{diag}([z^0, z^1, z^2, z^3])$$

Similarly,

$$\frac{1}{\sqrt{8}}\begin{bmatrix}(z^2)^0z^4 & (z^2)^0z^5 & (z^2)^0z^6 & (z^2)^0z^7\\ (z^2)^0z^4 & (z^2)^1z^5 & (z^2)^2z^6 & (z^2)^3z^7\\ (z^2)^0z^4 & (z^2)^2z^5 & (z^2)^4z^6 & (z^2)^{14}z^7\\ (z^2)^0z^4 & (z^2)^3z^5 & (z^2)^6z^6 & (z^2)^9z^7\end{bmatrix} = -\frac{1}{\sqrt{8}}\begin{bmatrix}(z^2)^0z^0 & (z^2)^0z^1 & (z^2)^0z^2 & (z^2)^0z^3\\ (z^2)^0z^0 & (z^2)^1z^1 & (z^2)^2z^2 & (z^2)^3z^3\\ (z^2)^0z^0 & (z^2)^2z^1 & (z^2)^4z^2 & (z^2)^6z^3\\ (z^2)^0z^0 & (z^2)^3z^1 & (z^2)^6z^2 & (z^2)^9z^3\end{bmatrix}$$

$$\equiv -\tfrac{1}{\sqrt{2}}\ D_{44}\,\text{diag}([z^0, z^1, z^2, z^3])$$

However, the second order DFT is similar to 3-dB antisymmetric coupler with a scattering matrix.

$$D_{22} = \frac{1}{\sqrt{2}}\begin{bmatrix}1 & 1\\ 1 & -1\end{bmatrix}$$

The transfer matrix of 4×4 DFT (D_{44}) can be defined as follows:

$$D_{44} = \frac{1}{\sqrt{4}}\begin{bmatrix}1 & 1 & 1 & 1\\ 1 & -i & -1 & i\\ 1 & -1 & 1 & -1\\ 1 & i & -1 & -i\end{bmatrix}$$

Fig. 2.2 represents the 8×8 DFT coupler architecture composed of a combination of 2×2 and 4×4 DFT network. A 2×2 MMI transmission matrix is re-phasing equivalent to D_{22}. A 4×4 DFT MMI transmission matrix is re-phasing permutation equivalent to D_{44}. Account must be taken of the re-

phasing and permutations. However, re-ordering and re-phasing of output ports most likely can be neglected and the re-phasing phase shifts consolidated with other phase shifts. The ordering of the inputs above suits differential drive MZI – the D_{22} couplers are then the output couplers of the MZI. The transpose of the above network may be used as the input coupler (it may be partially equipped if only one input is used). The rephrasing phase shifts within the MZI arms then conveniently cancel. Note the path length of all the links in the diagram above are taken as zero. In practice, this means paths between stages must be matched. The cross-over interconnect above is in that respect in convenient. One can implement crossovers using MMIs and other coupler structures and the phase-shifts incurred are in principle predictable and can be compensated.

2.4 Realization of DFT Using MMI Coupler

The realization of optical DFT network ease the applications of all optical signal processing techniques. The DFT operations involved in subdividing of N input array with an appropriate phase shifter fed into $N \times N$ MMI and then the desired N different output signal is extracted via a suitable value of phase shifters. We derived an analytical formula of transfer matrix for the MMI couplers that resembles with the transform matrix of DFT by placing suitable phases shifters at the input and output ports. In other words, by properly adjusting the phase shifters, the DFT network can be realized all in optical domain based on MMI couplers. The MMI-DFT equivalence expressions in terms of transmission matrix for even dimensions are given below.

For N even, the elements of the transmission matrix T_{MMI} of a standard uniform split ratio MMI coupler are:

$$\{T_{MMI}\}_{v\mu} = \frac{1}{\sqrt{N}} e^{-i\alpha} \begin{cases} exp[i(\frac{v-\mu}{2})^2 \frac{\pi}{N}], & (v-\mu) \quad even \\ -exp[i(\frac{v+\mu+1}{2})^2 \frac{\pi}{N}], & (v-\mu) \quad odd \end{cases} \tag{2.9}$$

where α represents the loss factor. For sake of simplicity, the term loss factor is ignored for rest of the analysis. Set:

$$\{\Gamma\}_{v\mu} = \begin{cases} exp[-i(\frac{v}{2})^2 \frac{\pi}{N}], & v \quad even \\ -exp[-i(\frac{v+1}{2})^2 \frac{\pi}{N}], & v \quad odd \end{cases} \tag{2.10}$$

$$\{\Gamma\}_{\mu\mu} = \begin{cases} exp[-i(\frac{\mu}{2})^2 \frac{\pi}{N}], & \mu \quad even \\ -exp[-i(\frac{\mu+1}{2})^2 \frac{\pi}{N}], & \mu \quad odd \end{cases} \tag{2.11}$$

De-phase:

$$\{\Gamma T_{MMI} \Gamma\}_{v\mu} = \frac{1}{\sqrt{N}} \begin{cases} exp[-i(\frac{\mu}{2})^2 \frac{\pi}{N}] exp[i(\frac{v-\mu}{2})^2 \frac{\pi}{N}] exp[-i(\frac{\mu}{2})^2 \frac{\pi}{N}], & v \; even, \mu \; even \\ exp[-i(\frac{\mu}{2})^2 \frac{\pi}{N}] exp[i(\frac{v+\mu+1}{2})^2 \frac{\pi}{N}] exp[-i(\frac{\mu+1}{2})^2 \frac{\pi}{N}], & v \; even, \mu \; odd \\ exp[-i(\frac{v+1}{2})^2 \frac{\pi}{N}] exp[i(\frac{v+\mu+1}{2})^2 \frac{\pi}{N}] exp[-i(\frac{\mu+1}{2})^2 \frac{\pi}{N}], & v \; odd, \mu \; even \\ exp[-i(\frac{v+1}{2})^2 \frac{\pi}{N}] exp[i(\frac{v-\mu}{2})^2 \frac{\pi}{N}] exp[-i(\frac{\mu+1}{2})^2 \frac{\pi}{N}], & v \; odd, \mu \; odd \end{cases}$$

Simplifying:

$$\{\Gamma T_{MMI}\Gamma\}_{v\mu} = \frac{1}{\sqrt{N}} \begin{cases} exp[-i\frac{v\mu}{4}\frac{2\pi}{N}], & v\ even, \mu\ even \\ exp[i\frac{v(\mu+1)}{4}\frac{2\pi}{N}], & v\ even, \mu\ odd \\ exp[i\frac{\mu(v+1)}{4}\frac{2\pi}{N}], & v\ odd, \mu\ even \\ exp[-i\frac{(v+1)(\mu+1)}{4}\frac{2\pi}{N}], & v\ odd, \mu\ odd \end{cases}$$

Now set $z = exp(-i\frac{2\pi}{N})$

Consequently, the matrix of powers of z that compose the de-phased transmission matrix is:

$$\begin{bmatrix} 0 & 0 & 0 & 0 & 0 & 0 & 0 & 0 & 0 & 0 & 0 & 0 & 0 & 0 & 0 & 0 \\ 0 & -1 & 1 & -2 & 2 & -3 & 3 & -4 & 4 & -5 & 5 & -6 & 6 & -7 & 7 & -8 \\ 0 & 1 & -1 & 2 & -2 & 3 & -3 & 4 & -4 & 5 & -5 & 6 & -6 & 7 & -7 & 8 \\ 0 & -2 & 2 & -4 & 4 & -6 & 6 & -8 & 8 & -10 & 10 & -12 & 12 & -14 & 14 & -16 \\ 0 & 2 & -2 & 4 & -4 & 6 & -6 & 8 & -8 & 10 & -10 & 12 & -12 & 14 & -14 & 16 \\ 0 & -3 & 3 & -6 & 6 & -9 & 9 & -12 & 12 & -15 & 15 & -18 & 18 & -21 & 21 & -24 \\ 0 & 3 & -3 & 6 & -6 & 9 & -9 & 12 & -12 & 15 & -15 & 18 & -18 & 21 & -21 & 24 \\ 0 & -4 & 4 & -8 & 8 & -12 & 12 & -16 & 16 & -20 & 20 & -24 & 24 & -28 & 28 & -32 \\ 0 & 4 & -4 & 8 & -8 & 12 & -12 & 16 & -16 & 20 & -20 & 24 & -24 & 28 & -28 & 32 \\ 0 & -5 & 5 & -10 & 10 & -15 & 15 & -20 & 20 & -25 & 25 & -30 & 30 & -35 & 35 & -40 \\ 0 & 5 & -5 & 10 & -10 & 15 & -15 & 20 & -20 & 25 & -25 & 30 & -30 & 35 & -35 & 40 \\ 0 & -6 & 6 & -12 & 12 & -18 & 18 & -24 & 24 & -30 & 30 & -36 & 36 & -42 & 42 & -48 \\ 0 & 6 & -6 & 12 & -12 & 18 & -18 & 24 & -24 & 30 & -30 & 36 & -36 & 42 & -42 & 48 \\ 0 & -7 & 7 & -14 & 14 & -21 & 21 & -28 & 28 & -35 & 35 & -42 & 42 & -49 & 49 & -56 \\ 0 & 7 & -7 & 14 & -14 & 21 & -21 & 28 & -28 & 35 & -35 & 42 & -42 & 49 & -49 & 56 \\ 0 & -8 & 8 & -16 & 16 & -24 & 24 & -32 & 32 & -40 & 40 & -48 & 48 & -56 & 56 & -64 \end{bmatrix}$$

Unlike MZI-based and a hybrid architecture of MMI-based all optical DFT network, the proposed circuit design does not need any cascaded structures. The key advantage of this simplified method is that it can significantly reduce fabrication efforts for the higher order DFT points. For example, the number of MZI including phase shifters are needed of $Nlog2(N)/2$ for N points DFT. On the other hand, one MMI coupler with suitable choice of phase shifters with N input/output ports is sufficient to implement N points DFT in all optically. However, the phase shifter arrays can be characterized by the two diagonal matrixes that are multiplied on both sides of MMI coupler matrix, M. The detailed illustration and mathematical formulation of the realization of n-DFT using n^{th} order MMI coupler is presented in Appendix I.

***Equivalence mod N=2**:*

$$\begin{bmatrix} 0 & 0 \\ 0 & -1 \end{bmatrix} \equiv \begin{bmatrix} 0 & 0 \\ 0 & 1 \end{bmatrix} \Rightarrow \Gamma T_{MMI}\Gamma = \frac{1}{\sqrt{2}}\begin{bmatrix} z^0 & z^0 \\ z^0 & z^1 \end{bmatrix} = \frac{1}{\sqrt{2}}D_2, \quad M_2 = \frac{1}{\sqrt{2}}\begin{bmatrix} 1 & -i \\ -i & 1 \end{bmatrix} \rightarrow 2 \times 2 \ \ 3dB \text{ MMI coupler}$$

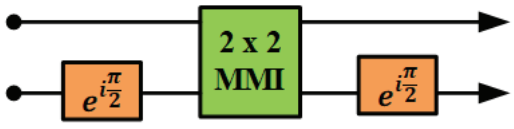

Figure 2.3: Realization of 2×2 DFT using 2×2 MMI.

***Equivalence mod N=4**:*

$$\begin{bmatrix} 0 & 0 & 0 & 0 \\ 0 & -1 & 1 & -2 \\ 0 & 1 & -1 & 2 \\ 0 & -2 & 2 & -4 \end{bmatrix} \equiv \begin{bmatrix} 0 & 0 & 0 & 0 \\ 0 & 3 & 1 & 2 \\ 0 & 1 & 3 & 2 \\ 0 & 2 & 2 & 0 \end{bmatrix} \Rightarrow \Gamma T_{MMI} \Gamma = \frac{1}{\sqrt{4}} \begin{bmatrix} z^0 & z^0 & z^0 & z^0 \\ z^0 & z^3 & z^1 & z^2 \\ z^0 & z^1 & z^3 & z^2 \\ z^0 & z^2 & z^2 & z^0 \end{bmatrix}$$

Re-order columns then rows and finally unwrap powers:

$$\begin{bmatrix} z^0 & z^0 & z^0 & z^0 \\ z^0 & z^1 & z^2 & z^3 \\ z^0 & z^3 & z^2 & z^1 \\ z^0 & z^2 & z^0 & z^2 \end{bmatrix} \Rightarrow \begin{bmatrix} z^0 & z^0 & z^0 & z^0 \\ z^0 & z^1 & z^2 & z^3 \\ z^0 & z^2 & z^0 & z^2 \\ z^0 & z^3 & z^2 & z^1 \end{bmatrix} \equiv \begin{bmatrix} z^0 & z^0 & z^0 & z^0 \\ z^0 & z^1 & z^2 & z^3 \\ z^0 & z^2 & z^4 & z^6 \\ z^0 & z^3 & z^6 & z^9 \end{bmatrix} = D_4$$

Figs. 2.3 and 2.4 demonstrates the realization of 2×2 DFT using 2×2 MMI and 4×4 DFT using 4×4 MMI respectively. However, the validation of the presented mathematical model for 8×8 DFT using 8×8 MMI is illustrated with insightful comments in result analysis section. Likewise, the circuit design for 8×8 DFT, all others lower and higher order DFT based on MMI can be explained in a similar way.

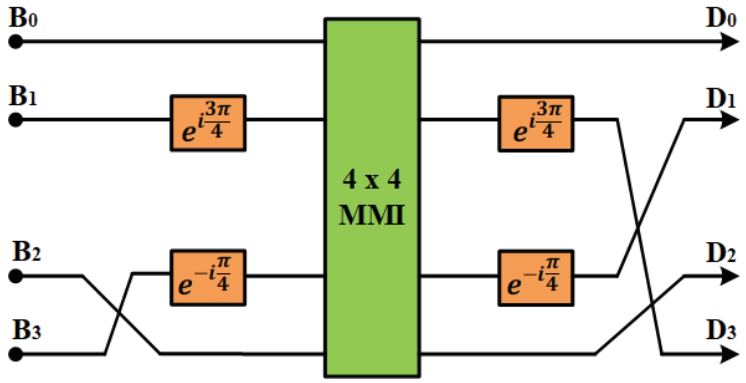

Figure 2.4: Realization of 4×4 DFT using 4×4 MMI.

***Equivalence mod N=8**:*

$$\begin{bmatrix} 0 & 0 & 0 & 0 & 0 & 0 & 0 & 0 \\ 0 & -1 & 1 & -2 & 2 & -3 & 3 & -4 \\ 0 & 1 & -1 & 2 & -2 & 3 & -3 & 4 \\ 0 & -2 & 2 & -4 & 4 & -6 & 6 & -8 \\ 0 & 2 & -2 & 4 & -4 & 6 & -6 & 8 \\ 0 & -3 & 3 & -6 & 6 & -9 & 9 & -12 \\ 0 & 3 & -3 & 6 & -6 & 9 & -9 & 12 \\ 0 & -4 & 4 & -8 & 8 & -12 & 12 & -16 \end{bmatrix} \equiv \begin{bmatrix} 0 & 0 & 0 & 0 & 0 & 0 & 0 & 0 \\ 0 & 7 & 1 & 6 & 2 & 5 & 3 & 4 \\ 0 & 1 & 7 & 2 & 6 & 3 & 5 & 4 \\ 0 & 6 & 2 & 4 & 4 & 2 & 6 & 0 \\ 0 & 2 & 6 & 4 & 4 & 6 & 2 & 0 \\ 0 & 5 & 3 & 2 & 6 & 7 & 1 & 4 \\ 0 & 3 & 5 & 6 & 2 & 1 & 7 & 4 \\ 0 & 4 & 4 & 0 & 0 & 4 & 4 & 0 \end{bmatrix}$$

Re-order columns then rows and finally unwrap powers:

$$\Gamma T_{MMI}\Gamma = \frac{1}{\sqrt{8}}\begin{bmatrix} z^0 & z^0 & z^0 & z^0 & z^0 & z^0 & z^0 & z^0 \\ z^0 & z^7 & z^1 & z^6 & z^2 & z^5 & z^3 & z^4 \\ z^0 & z^1 & z^7 & z^2 & z^6 & z^3 & z^5 & z^4 \\ z^0 & z^6 & z^2 & z^4 & z^4 & z^2 & z^6 & z^0 \\ z^0 & z^2 & z^6 & z^4 & z^4 & z^6 & z^2 & z^0 \\ z^0 & z^5 & z^3 & z^2 & z^6 & z^7 & z^1 & z^4 \\ z^0 & z^3 & z^5 & z^6 & z^2 & z^1 & z^7 & z^4 \\ z^0 & z^4 & z^4 & z^0 & z^0 & z^4 & z^4 & z^0 \end{bmatrix} \Rightarrow \begin{bmatrix} z^0 & z^0 & z^0 & z^0 & z^0 & z^0 & z^0 & z^0 \\ z^0 & z^1 & z^2 & z^3 & z^4 & z^5 & z^6 & z^7 \\ z^0 & z^7 & z^6 & z^5 & z^4 & z^3 & z^2 & z^1 \\ z^0 & z^2 & z^4 & z^6 & z^0 & z^2 & z^4 & z^6 \\ z^0 & z^6 & z^4 & z^2 & z^0 & z^6 & z^4 & z^2 \\ z^0 & z^3 & z^6 & z^1 & z^4 & z^7 & z^2 & z^5 \\ z^0 & z^5 & z^2 & z^7 & z^4 & z^1 & z^6 & z^3 \\ z^0 & z^4 & z^0 & z^4 & z^0 & z^4 & z^0 & z^4 \end{bmatrix}$$

$$\Rightarrow \begin{bmatrix} z^0 & z^0 & z^0 & z^0 & z^0 & z^0 & z^0 & z^0 \\ z^0 & z^1 & z^2 & z^3 & z^4 & z^5 & z^6 & z^7 \\ z^0 & z^2 & z^4 & z^6 & z^0 & z^2 & z^4 & z^6 \\ z^0 & z^3 & z^6 & z^1 & z^4 & z^7 & z^2 & z^5 \\ z^0 & z^4 & z^0 & z^4 & z^0 & z^4 & z^0 & z^4 \\ z^0 & z^5 & z^2 & z^7 & z^4 & z^1 & z^6 & z^3 \\ z^0 & z^6 & z^4 & z^2 & z^0 & z^6 & z^4 & z^2 \\ z^0 & z^7 & z^6 & z^5 & z^4 & z^3 & z^2 & z^1 \end{bmatrix} \equiv \begin{bmatrix} z^0 & z^0 & z^0 & z^0 & z^0 & z^0 & z^0 & z^0 \\ z^0 & z^1 & z^2 & z^3 & z^4 & z^5 & z^6 & z^7 \\ z^0 & z^2 & z^4 & z^6 & z^8 & z^{10} & z^{12} & z^{14} \\ z^0 & z^3 & z^6 & z^9 & z^{12} & z^{15} & z^{18} & z^{21} \\ z^0 & z^4 & z^8 & z^{12} & z^{16} & z^{20} & z^{24} & z^{28} \\ z^0 & z^5 & z^{10} & z^{15} & z^{20} & z^{25} & z^{30} & z^{35} \\ z^0 & z^6 & z^{12} & z^{18} & z^{24} & z^{30} & z^{36} & z^{42} \\ z^0 & z^7 & z^{14} & z^{21} & z^{28} & z^{35} & z^{42} & z^{49} \end{bmatrix} = D_8$$

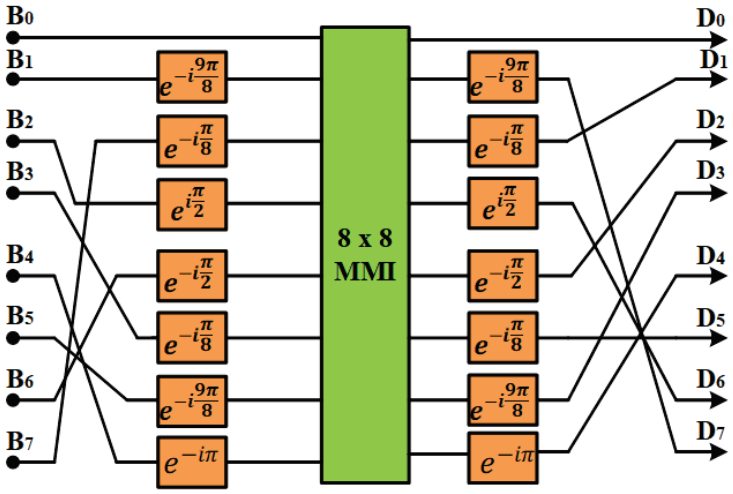

(a) Realization of 8×8 DFT using 8×8 MMI

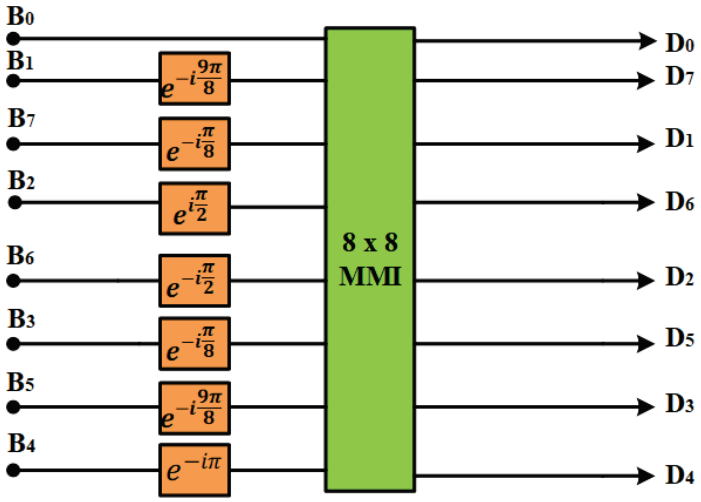

(b) Simplified architecture of 8×8 Optical DFT network without crossover.

Figure 2.5: 8×8 optical DFT network

Fig. 2.5a depicts an 8×8 DFT network using 8×8 MMI coupler with suitable phase shifter in the suitable position. The waveguide intersection at the input side can be easily ignored by interchanging the RF drive signal among the phase modulators. Likewise, the output crossover is not mandatory as shown in Fig. 2.5b for implementation if the harmonics at the particular output port is known and the phase factor can be eliminated where the overall phase carriers are irrelevant. However, Fig. 2.6 shows the cascaded Y-branches are used as 1×8 splitter which can also be replaced by using 8×8 MMI with proper choice of phase values and the simulation results can be monitored by optical spectrum analyzer (OSA). The transfer matrix of 8×8 MMI can be written as:

$$M_{88} = \frac{1}{\sqrt{8}} \begin{bmatrix} 1 & -\xi & \xi & -i & i & \xi & -\xi & -1 \\ -\xi & 1 & -i & \xi & \xi & i & -1 & -\xi \\ \xi & -i & 1 & \xi & \xi & -1 & i & \xi \\ -i & \xi & \xi & 1 & -1 & \xi & \xi & i \\ i & \xi & \xi & -1 & 1 & \xi & \xi & -i \\ \xi & i & -1 & \xi & \xi & 1 & -i & \xi \\ -\xi & -1 & i & \xi & \xi & -i & 1 & -\xi \\ -1 & -\xi & \xi & i & -i & \xi & -\xi & 1 \end{bmatrix}$$

where $\xi = exp(-i\frac{\pi}{8})$. If the values of phase shifter are set according to Fig. 2.5a and after the necessary shuffling between columns and rows, the transfer matrix of 8×8 DFT can be written as:

$$\begin{bmatrix} D_0 \\ D_7 \\ D_1 \\ D_6 \\ D_2 \\ D_5 \\ D_3 \\ D_4 \end{bmatrix} = \frac{1}{\sqrt{8}} \begin{bmatrix} 1 & 1 & 1 & 1 & 1 & 1 & 1 & 1 \\ 1 & e^{-i\pi/4} & -i & e^{-i3\pi/4} & -1 & e^{-i\pi/4} & i & e^{-i3\pi/4} \\ 1 & -i & -1 & i & 1 & -i & -1 & i \\ 1 & e^{-i3\pi/4} & i & e^{-i\pi/4} & -1 & e^{-i3\pi/4} & -i & e^{-i\pi/4} \\ 1 & -1 & 1 & -1 & 1 & -1 & 1 & -1 \\ 1 & e^{-i\pi/4} & -i & e^{-i3\pi/4} & -1 & e^{-i\pi/4} & i & e^{-i3\pi/4} \\ 1 & i & -1 & -i & 1 & i & -1 & -i \\ 1 & e^{-i3\pi/4} & i & e^{-i\pi/4} & -1 & e^{-i3\pi/4} & -i & e^{-i\pi/4} \end{bmatrix} \begin{bmatrix} B_0 \\ B_1 \\ B_7 \\ B_2 \\ B_6 \\ B_3 \\ B_5 \\ B_4 \end{bmatrix}$$

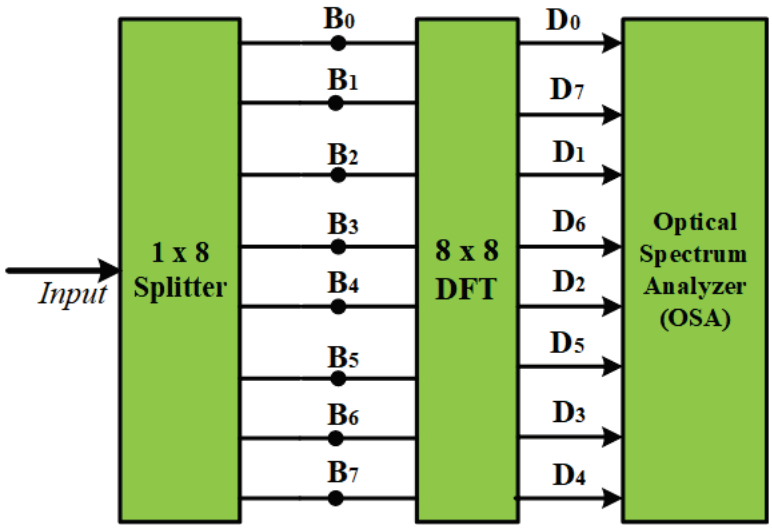

Figure 2.6: Schematic for monitoring the output optical spectrum using OSA of 1 GHz bandwidth.

Note that a uniform distribution of amplitude and phase of an input signal applied to DFT network resulting spatial frequency shifting of subcarriers of $p\omega_{RF}$ module N, where p is the output port number and ω_{RF} is the angular frequency of RF source to drive the phase modulators with a progressive $\frac{2\pi}{N}$ phase shift.

Thereafter, a transfer matrix analysis is conducted for further simplification of this architecture and demonstrate operational functionality with carrier frequency shift $q\omega_{RF}$ emitted from output port q modulo N. Reference [29] proposed the optical DFT elements incorporated with a single MMI coupler augmented by static phase shift element. An implementation of linear transformation operation using a mesh MZI in optical DFT is presented in [18]. It has been established the transmission matrix of a $N\times N$ MMI is permutation-phase equivalent to a $N\times N$ DFT for N=2, 4, 6, 8, 12, 16. As explained beforehand, the analysis of odd dimensions MMI-DFT expansions is carried out in the following subsection.

***Equivalence mod N=3**:*

$$T_{MMI} = \frac{1}{\sqrt{3}}\begin{bmatrix} -z & z & -z^3 \\ z & -z^3 & z \\ -z^3 & z & -z \end{bmatrix} = -z\frac{1}{\sqrt{3}}\begin{bmatrix} 1 & -1 & z^2 \\ -1 & z^2 & -1 \\ z^2 & -1 & 1 \end{bmatrix}$$

where $z = exp(i\frac{\pi}{3})$, $\Gamma = diag([1, -1, z^{-2}])$, and $w = exp(i\frac{2\pi}{3})$

De-phase:

$$\Gamma T_{MMI}\Gamma = -z\frac{1}{\sqrt{3}}\begin{bmatrix} 1 & 1 & 1 \\ 1 & z^2 & z^{-2} \\ 1 & z^{-2} & z^{-4} \end{bmatrix} \equiv -z\frac{1}{\sqrt{3}}\begin{bmatrix} w^0 & w^0 & w^0 \\ w^0 & w^1 & w^{-1} \\ w^0 & w^{-1} & w^{-2} \end{bmatrix}$$

Equivalence mod N:

$$\begin{bmatrix} w^0 & w^0 & w^0 \\ w^0 & w^1 & w^{-1} \\ w^0 & w^{-1} & w^{-2} \end{bmatrix} \equiv \begin{bmatrix} w^0 & w^0 & w^0 \\ w^0 & w^1 & w^2 \\ w^0 & w^2 & w^1 \end{bmatrix}$$

Unwrap powers:

$$\begin{bmatrix} w^0 & w^0 & w^0 \\ w^0 & w^1 & w^2 \\ w^0 & w^2 & w^1 \end{bmatrix} \equiv \begin{bmatrix} w^0 & w^0 & w^0 \\ w^0 & w^1 & w^2 \\ w^0 & w^2 & w^4 \end{bmatrix} = D_3$$

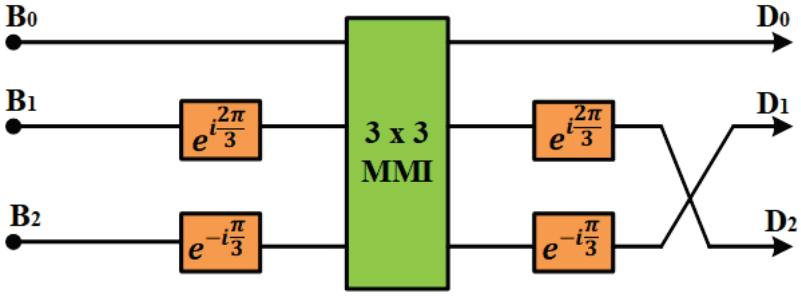

Figure 2.7: Realization of 3×3 DFT using 3×3 MMI.

The realization of 3×3 DFT using 3×3 MMI is depicted in Fig. 2.7. It has been established that the transmission matrix of standard uniform split $N \times N$ MMI coupler is permutation-phase equivalent to a $N \times N$ DFT for $N = 5, 7$. Note that extension of higher order MMI based DFT is straightforward.

2.5 Simulation Results and Verification

A continuous wave (CW) DFB laser with a power of 10 mW and operating at 1550 nm wavelength is used as an optical source in the simulation process. A 10 GHz RF drive signal having a peak amplitude of $V_{RF} = 0.125\ V_\pi$ (V_π is the half-wave voltage of the phase modulator) is applied to the phase modulators with suitable phase shift and a suitable phase shifter value is set to the phase each modulator. The concept of 8×8 DFT under even configuration is justified employing industry standard VPI photonics software tool. Fig. 2.8 and Fig. 2.9 represents the optical spectrum of theoretical assumption. It is widely accepted that MMI suffers phase deviations in practice with respect to the ideal case and these deviations results to non-ideal DFT behavior. In other words, the phase deviations and power imbalances among MMI ports leads to fabrication error. Because of power imbalances and phase inaccuracy between MMI ports due to fabrication flaws and problems in the path length of the electrical waveguides that connect the RF source and phase modulator electrodes, the circuit's correct function may diverge from ideal. Assume that all the circuit components experience similar impairments. To account for the MMI design errors, we consider 0.5^o to 2^o phase error range and 0.7% power imbalance of an ideal MMI (sufficient of simulated results with errors [24]) among the output ports and loaded for all MMI ports.

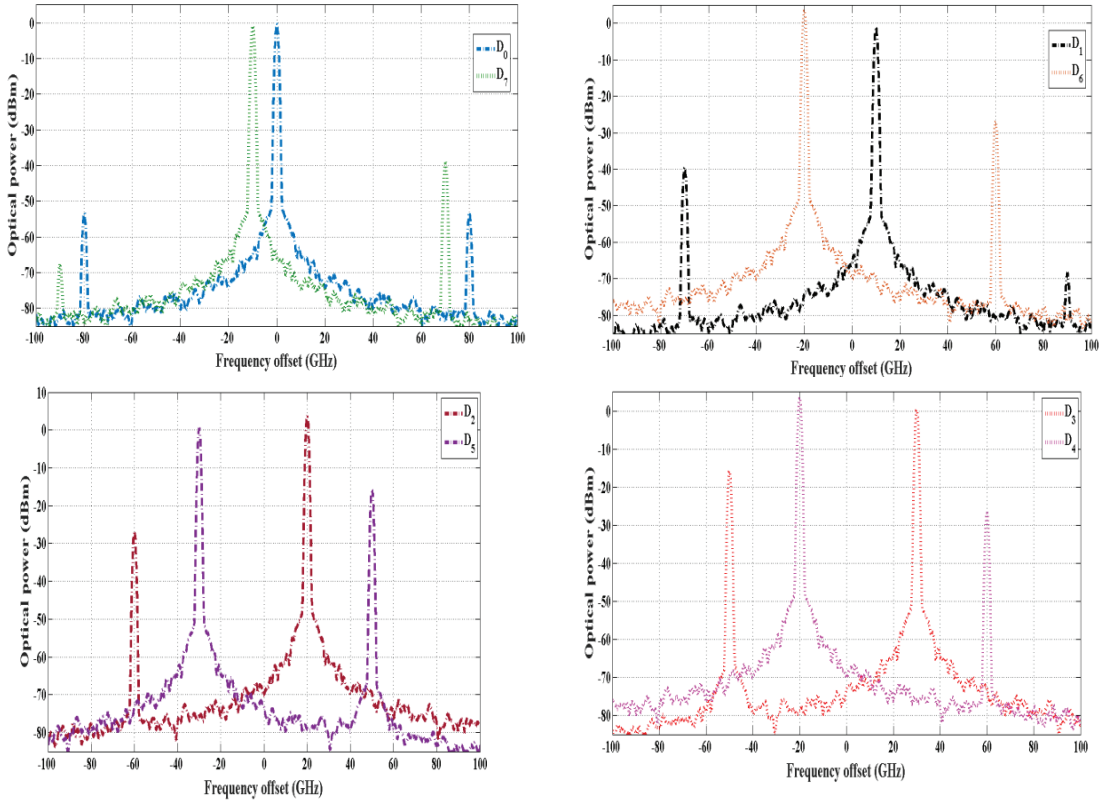

Figure 2.8: Optical spectrum of 8×8 DFT without considering MMI errors.

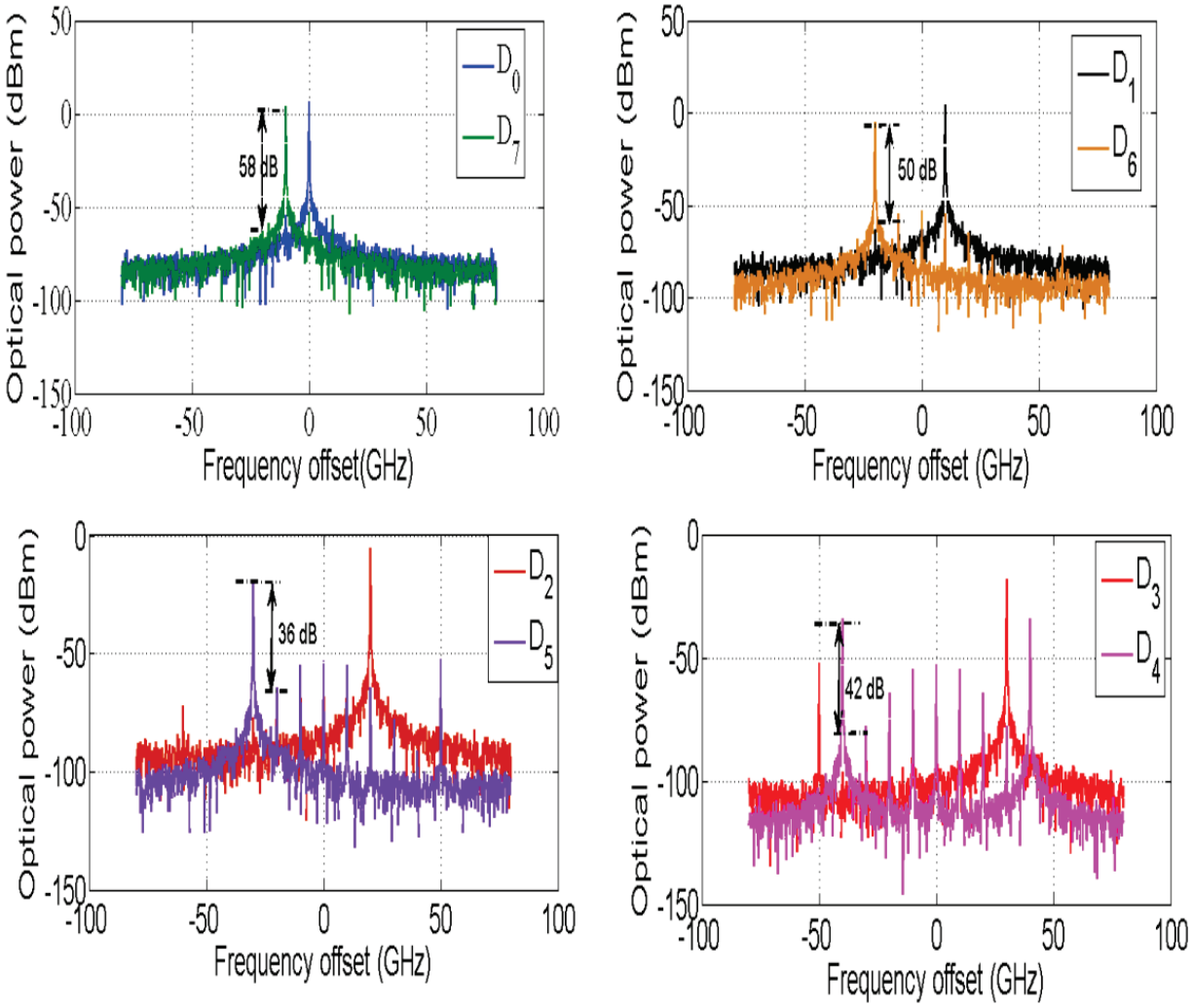

Figure 2.9: Optical spectrum of 8×8 DFT considering MMI design errors.

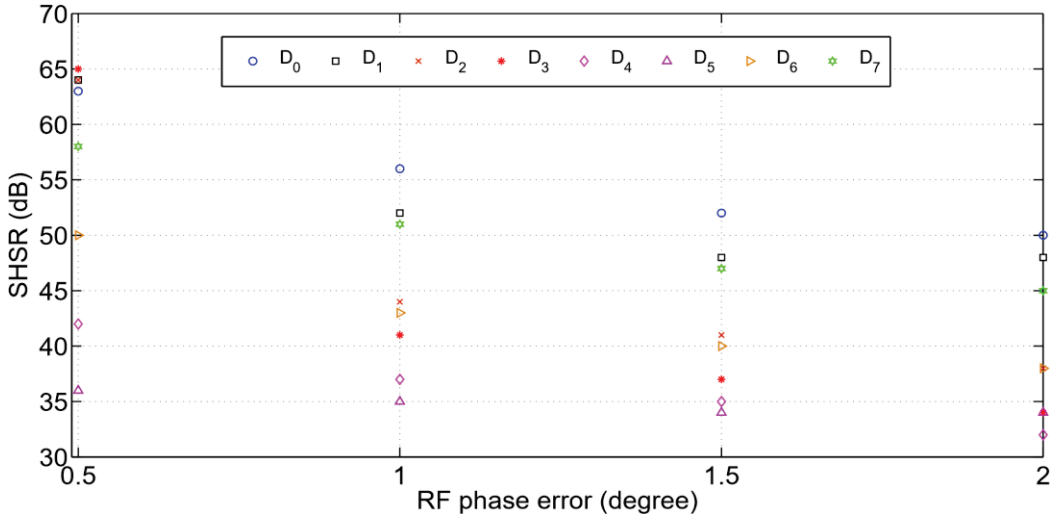

Figure 2.10: Optical SHSR vs RF drive's phase errors for 8×8 MMI.

Fig. 2.10 represents the optical spectra with the design errors i.e., 1^o phase error. Carrier break through is apparent from the figure which limits the expected system performance. Results shows that 36 dB or more of side harmonic suppression ratio (SHSR) can be attained for 1^o phase error. Fig. 2.11 and demonstrates optical SHSR variation as a function of RF drive phase error. A clear distinction of SHSR distribution is observed from the four different phase mismatches. SHSR performance is considerably reduced for the higher value of design errors as evident from the figure. Nonetheless a minimum 32 dB SHSR can be achieved for 1^o phase error. However, the optical phase errors can be considerably reduced using the sub-wavelength engineered MMI over a large bandwidth in compared with conventional MMI [41], [42]. Moreover, the joint use of RF phase shifters with the optical circuitry inherently eliminates phase shift errors and expedites electrical trimming [43].

To the end, the proposed circuit operation is not restricted to only DFT functions rather any linear optical transformation although the prime objective is focused on phase correlated subcarrier generation. The suggested circuit framework can be used for optical wireless information processing systems in discrete space form [44]. Simulations validate the assumptions of a transfer matrix model of the considered circuit model operations.

2.6 Summary

In this chapter, we investigated a coherent electro-optic circuit design approach that generates a frequency comb of *N* separated harmonically subcarriers. The proposed design comprises of 1×N splitter that feeds light into a parallel array of *N* electro-optic phase modulators electrically driven by RF signal with a progressive phase shift $\frac{2\pi}{N}$ with their phase modulated optical outputs processed by an *N*×*N* optical DFT. All though phase-correlated but spatially separated subcarrier generation is the principal aim; the circuit can subsume majority of the RF photonic applications in the prior art. The analytical formulation with necessary circuit diagram for even and odd dimensions of MMI based DFT is presented. In a nutshell, a pragmatic design approach for implementing optical DFT in photonic networks composed of waveguide splitters, combiners, and phase-shift elements have been presented. A system impairment such as fabrication errors has been taken into account during simulation under a realistic scenario. There is no tuning element in the circuit to compensate the MMI output power imbalances and phase errors due to the fabrication and bias errors. An industry standard software tool is used to verify the assumption of transfer matrix model for the circuit operation. The proposed architecture is not limited to an optical DFT but applicable in any optical linear transformation. However, the proposed circuit design subsumes many prior RF photonic circuit architectures with a suitable choice of output ports based on dimension *N*. The circuit implementation is found to be practical which depends on the availability of an appropriate photonic integration platform. Future extension of this work will focus on developing the validation of both even and odd configurations of DFT using CAD tools like FIMMWAVE in order to make realistic scenario and the verification of the circuit performance with the analytical model.

CHAPTER 3

Advances in Integrated Heterogeneous Electro-Optic Modulator

3.1 Introduction

Electro-optic modulators (EOMs) are fundamental component for high-speed optical communication, sensing technologies, signal processing, microwave photonics (MWP), and quantum computing. Next-generation EOMs demand low cost, high-density integration, and excellent system performance simultaneously, which are difficult to obtain with existing integrated photonics platforms. Thin-film lithium niobate (TFLN) has emerged as a strong contender due to its lower power consumption, high intrinsic electro-optic efficiency, smaller footprint, robustness, wider bandwidths, industry-proven performance, and most importantly, the rapid development of scalable fabrication techniques. However, conventional bulk LN EOMs privided large optical mode size with poor confinement and suffer from wide bending radii due to low index contrast (< 0.02). On the other hand, the importance of silicon nitride (Si3N4) thin films have been enormously increased because of small thermo-optic coefficient, ultralow propagation loss, very low second order nonlinearity, high-power handling capability, and particularly, ease of photonic integrated circuit (PIC) compatibility. The hybrid approach of utilizing silicon nitride on lithium niobate waveguide integrated on a single chip has anticipated best optical modulation performance that opens a broad range of opportunities such as chip-scale MWP systems, universal linear optical networks, ultra-speed optical switching, etc. This chapter begins with a brief overview of hybrid EOMs and a discussion of the current state of LN on insulator (LNOI) photonics. The subsequent sections describe the recent expansion of hybrid EO modulators categorized into photonic-integrated circuits and electro-optic tunable devices. This chapter also discussed the implementation challenges, potential solutions, and future research opportunities that may benefit the pursuit of this vision.

3.2 Theory

The ability to integrate lithium niobate (LN) and AlN directly with photonic platforms utilizing silicon nitride waveguides with oxide cladding opens up numerous opportunities for chip-scale microwave photonics (MWP) systems, universal linear optical networks, switch networks of optical communications, and nonlinear photonics. An optical modulator is a key building block for photonic integrated circuits (PICs), as its applications are widespread in both analog and digital systems such as on-chip RF photonics, passive millimeter wave imaging systems, modern telecommunication networks, data communication, frequency comb generation, highspeed signal processing, and quantum information processing. In order to realize a quantum internet in which superconducting quantum processors are connected via optical links; a quantum efficient electro-optic modulator is required to convert signals between the microwave and optical domains while preserving quantum correlations. The heterogeneous approach of utilizing LN, AlN on SN

waveguide is focused on developing a platform where the ultra-fast, ultra low-loss, ultra power-efficient optical phase shifters are integrated on a single chip. With the introduction of a Silicon Nitride integrated optics platform enable to empower important new applications such as modulators, frequency conversions that require picosecond class wavelength tuning speeds on sub 100 GHz dense wavelength division multiplexing grids, picosecond class photonic space switching, faster optical modulators (above 100 gigabauds) and all-photonic processing for artificial intelligence and quantum computing.

The biggest hooked up vicinity of applications in demand of advanced electro-optic modulators these days is at the end of millions of optical fibers connectivity in telecommunication and optical networks in data center. The fundamental lead in information delivery capability via optical fibers upon their invention have been eclipsed by means of the continuous development of bandwidth according to Moore's law [45]. A data center of application-specific integrated circuit switch transferred 25.6 Tb/s of data in 2020, requiring speeds of over 400 Gb/s for each lane of optical wavelengths [46]. However, the data rate is anticipated to double in the upcoming years and will continue to uplift with the augmentation of technology progression [47]. The up-trending demand for integrated EOMs in optical communication is to minimize power consumption while operating at ultra-high speed and maintaining an expected signal-to-noise ratio (SNR) [48]. Emerging applications including as satellite data networks [49], optical sensors [50], and quantum information processing [51] are driving demand for higher performance and integrated modulators. Beyond traditional telecommunication applications, these technologies frequently require electro-optic (EO) functionalities, such as linearized modulators for analog communications [52], low latency switching for quantum communications [53], and ultra-fast integrated modulator arrays for optical neural networks [54].

Integrated photonics has a lot of potential for realizing cost efficient scaled optical systems for high-speed communication, computation, and sensing. Furthermore, downsizing and integration of photonic structures into new design knobs and functionalities are not available in their bulk equivalents. For integrated photonics, a variety of material systems have been researched and adopted. Silicon (Si) [55], indium phosphide (InP) [56], silicon nitride (Si3N4) [57], aluminum nitride (AlN) [58], and silicon carbide (SiC) [59] are all good examples. Despite their advances, these material platforms are unable to support low propagation loss, faster and low-loss optical modulation, and efficient all-optical nonlinearities simultaneously. With the advancement of fabrication techniques, nanophotonic thin film LN waveguides have been widely realized in the area of integrated circuits due to emerging properties such as ultra-low-loss, high index contrast. On the thin-film LN platform, a comprehensive set of integrated ultrahigh-performance optical components with remarkable performance has been produced in the last few years [59]–[62].

Silicon photonics have advanced quickly due to largescale integration and low-cost demands [55], [63]. In addition to III-V [56] and conventional lithium niobate (LN) systems [59], silicon has become a major commercial photonics platform by using the mature complementary metal–oxide–semiconductor (CMOS) production infrastructure. While silicon photonics promises tremendous

scalability and low cost, the lack of inherent second-order non-linearity [63] poses increasing issues in terms of obtaining the requisite bandwidth and power consumption for future high-baud rate devices. Electronic doping confronts strict trade-offs between voltage, bandwidth, and optical losses, is frequently used in silicon for high-speed EO effects. As a result, numerous heterogeneous techniques to introducing superior EO solutions for silicon devices have been investigated.

For the recent development of integrated electro-optic circuits, silicon photonics has provided a diverse platform. Silicon waveguides are limited to operating wavelengths above 1100 nm due to the comparatively modest indirect bandgap of silicon (1.1eV), which prevents device operation in the visible spectrum range where low-noise lasers are readily available [64]–[66]. Due to silicon's narrow bandgap, silicon electro-optic devices are prone to severe two-photon absorption and free carrier absorption, which can result in significant thermal effects that restrict the devices' stability and cooling capability. In addition, silicon lacks the lowest order optical nonlinearity required for connecting with other active electrical components on a chip. The plasma dispersion effect is most typically used to modify the refractive index of silicon waveguides through mechanisms such as carrier accumulation, carrier injection, and depletion to accomplish modulation in silicon devices [67], [68]. Due to the long lifetime of free carriers, a careful balance must be maintained between modulation speed, efficiency, doping configuration, and carrier-induced absorption. The Pockels effect, on the other hand, is a broad-band, intrinsic characteristic of non-centrosymmetric crystals. The Pockels effect is frequently used in commercial highspeed electro-optic modulators, such as devices built of LiNbO3 and electro-optic organics, because it does not rely on free carriers. Common electro-optic materials with a high Pockels coefficient, on the other hand, are rarely compatible with CMOS technology. The quest for a suitable electro-optic material with large-scale integration capability on silicon substrates remains an outstanding topic in this concept [69].

Because of non-centrosymmetric crystal structures, lithium niobate is commonly used in PIC to overcome the aforementioned difficulties. TFLN (thin film lithium niobate) is a ferroelectric crystal with a number of desirable properties for integrated photonics platforms, including low loss, large electro-optic coefficient, linear modulation response, and broad modulation bandwidth. Strong second-order nonlinearity, pure phase modulation without optical absorption, zero to negative chirping, insignificant third-order nonlinearity, superior temperature stability, and a wide transmission spectrum have made lithium niobate (LiNbO3) the material of choice [70]. As a result, it is a popular material for guided wave optical devices and high-performance photonic integrated features, including switches, frequency doublers, surface acoustic wave devices, Pockels cells, optical parameter oscillators, and Q switching devices for lasers and among others.

TFLN platform could be an expedient option for next-generation EO photonic integrated circuits (PICs). This technology combines industry proven classical LN modulators' strong EO characteristics with scalable fabrication processes. In its bulk form, LN is a well-known and well-established substance that has been widely used in optical communications and radio signal processing. Thin-film LN permits modulator performance in previously inaccessible realms, demonstrating substantial integration potential, thanks to recent technological improvements in

thin-film material manufacturing and device design. The significant performance boost and reasonably well-understood nature of LN may be able to meet immediate optical communication needs while also enabling future sensors and quantum devices, for example, LN based electro-optic modulators are commonly used in fiber-optic communications, whereas periodically poled lithium niobate (PPLN) is employed for wavelength conversion and photon pair creation. Despite its enormous potential, LN has consistently lagged behind rival integrated photonic technologies, owing to major material integration and processing challenges. Low index-contrast waveguides, typically created by titanium (Ti) indiffusion or proton exchange in bulk LN, are the foundation of conventional integrated LN devices. Weak mode confinement, huge device footprints, and low nonlinear efficiency characterize these devices. As a consequence, LN devices remained bulky and discrete components. Other important integrated photonic systems, which are often built on thin films supported by low index cladding and benefit from high-index-contrast and sub-wavelength optical confinement, are in sharp contrast.

Silicon nitride (SN) is the ideal material among all of these due to its intrinsic material properties: ultralow propagation loss, very high-power handling capability, similar refractive index to LiNbO3, a small thermo-optic coefficient, low second-order nonlinearity, and PIC compatibility [70]. Due to highly desirable physical, chemical, and electrical features and the potential to enable new device technologies, interest in silicon nitride thin film material system continues to grow in both academic and industrial circles. SN is gaining popularity in the field of quantum optics as a result of its incredible potential for on-chip single-photon generators, compressed light, superconductive single-photon detectors, quantum walks, and time-bin encoding for quantum communication. Silicon nitride also allows interfacing with all typical quantum light sources, such as spontaneous parametric down-conversion, spontaneous four-wave mixing sources, and quantum dots, due to its wide spectrum transparency range (from 440 nm to 2.5 mm).

Thin film lithium niobate electro-optic modulators have grown in popularity over the last decade, promising lower voltage requirements and greater modulation bandwidths on a theoretically integrated platform. The current state of thin film modulator technology is discussed in this chapter, as well as a simplified modelling technique for fast optimizing a hybrid silicon niobate modulator. This chapter proposed on the best integration of advanced materials such as Lithium Niobate (LiNbO3) into an integrated optics platforms based on low-loss Silicon Nitride (Si3N4) waveguides with a goal of enabling high performance power-efficient optical phase shifters based on the Pockels effect under electrostatic and piezoelectric voltages.

3.3 Literature Review

A phase shifter is a photonic circuit component that allows you to electronically tune the effective refractive index of a waveguide. The thermo-optic (TO) effect is often used for deposited photonics such as Si3N4 by placing an external metal heater above the waveguide. Due to exceptional optical properties and diverse functionality, the Si3N4-LiNbO3 hybrid platform has lately been explored with considerable potential [71]. In comparison to alternative methods, this hybrid material system

combines LN's strong linear electro-optic effect with SN ultra-low propagation loss, low second order nonlinearity, small thermo-optic coefficient, high power handling capability, and wide optical transparency window to achieve low optical insertion loss, low nonlinearity due to plasma dispersion, ultra-fast modulation, and low voltage operation. Furthermore, a strip loaded Si3N4 waveguide on thin-film LiNbO3 enables for the creation of an etch-free LiNbO3 modulator [72]. Finally, the highly limited optical mode, together with closely spaced RF electrodes, greatly reduces the electrooptic tuning driving voltage. The first thin-film LiNbO3 Mach–Zehnder optical modulator that uses silicon nitride surface ridge optical waveguides was presented by Jin et al. [73]. A 1.2-cm-long push–pull phase modulation section and a pair of multimode interferometric 3-dB couplers make up the modulator. It displayed a $V\pi \times L\pi$ of 3 V.cm and an 8 GHz 3-dB bandwidth. A silicon nitride surface ridge is constructed on top of the LiNbO3 thin film to create lateral optical confinement. The simulated fundamental optical mode shows that the majority of the optical field is confined within the LiNbO3 thin film, with an 80 percent confinement factor. For a wavelength of 1.55 μm, the predicted $V\pi$ is 2.53 volts. Waveguide loss was measured to be around 7 dB/cm. The MMI coupler has a measured output imbalance of 0.35 dB. The modulator has a $V\pi$ and $L\pi$ of 3 V.cm. For this frequency response measurement, no DC bias voltage is used.

In [74], the authors demonstrated Mach-Zehnder modulators with V_L products of 0.5 Vcm and extinctions of 20 dB at = 674 nm, as well as ring resonators with Qs of up to 340,000 at = 1590 nm. The field's tight confinement in TFLN, with a simulated confinement factor of 82 percent, enables for efficient exploitation of LiNbO3's EO response, and the limited overlap with etched sidewalls may help minimize sidewall scattering. Ahmed et al. [75] showed a modified hybrid racetrack resonator made of PECVD Si3N4 X-cut LiNbO3 with modulating electrodes on both sides of the long arm of the racetrack. When the modulated optical sidebands are connected to the adjacent free spectral range (FSR) modes, the modulation effectiveness increases by around 10 dB. With an interaction zone length of 2.4 cm, the given amplitude modulator achieves a DC half-wave voltage of just 0.875 V, corresponding to a modulation efficiency per unit length of 2.11 V cm. The constructed device's power extinction ratio is around 30 dB, while the on-chip optical loss is around 5.4 dB. The present device's subvolt value is attained by simply lengthening the device and narrowing the electrode gap while retaining a high electrical and optical field overlap in the LiNbO3 area. The total optical insertion loss from the input fiber to the output fibers is estimated to be 19 dB, with coupling losses at the end facets accounting for the majority of this. The cutback method is used to measure the on-chip optical loss of 5.4 dB and coupling loss of 6.8 dB for this sort of device. The metal-induced absorption loss for the 5.8 mm electrode is less than 0.2 dB/cm. When compared to the bulk LiNbO3 equivalent, this modulation efficiency is improved by a factor of five, and it is comparable to the lowest possible non-hybrid TFLNOI modulator [76].

In order to achieve a low transition loss from the Si3N4 waveguide to the hybrid Si3N4-LiNbO3 structure, the authors presented a minimal but efficient mode converter system. A hybrid waveguide with a 1.7 mm wide, 200 nm thick Si3N4 strip loaded to a 300 nm thick LiNbO3 is chosen because it can support a more compact bending radius of 250 nm, higher mode confinement

in LiNbO3 of 0.63, and reduced mode transition loss. For non-etched LiNbO3, the simulated mode transition loss per interface is 2.67 dB. CMOS-compatible thin-film lithium niobate (TFLN) modulators with electro-optic 3 dB bandwidths of 30.6 GHz and half-wave voltages of 6.7 Vcm were demonstrated in reference [77]. Although etching LiNO3 is challenging [78] researchers have recently succeeded in etching TFLN, resulting in high-quality optical waveguides. It is possible to create high index contrast optical waveguides by dry etching this TFLN layer and significantly increase device performance by enhancing optical waveguide quality and providing better control over the group index of the optical mode [79]. The heterogeneous LiNbO3-Si3N4 based technology simplifies TFLN device and system fabrication while also addressing silicon's material limitations in terms of modulation and power handling capability. Table I demonstrated the comparison of material properties among LN, AlN and SN.

Table 3.1: Material property of AlN for photonics integrated circuit [80]

Properties	**AlN**	**Si_3N_4**	**$LiNbO_3$**
Refractive index	2.12	2.016	2.21
Bandgap energy (eV)	6.2	5.09	4.01
Waveguide loss (dB/cm)	0.42	1.9	0.37
Nonlinear index(cm^2/W)	2.3×10^{-15}	18×10^{-15}	1.8×10^{-19}
EO coefficient (pm/V)	0.67	8.31	32
Nonlinear susceptibility (pm/V)	4.7	2.38	-4.3
Piezoelectric coefficient (pm/V)	5.53	0.27	16
Thermal conductivity ($Wm^{-1}K^{-1}$)	285	26	4.19
CMOS-compatibility	Yes	Yes	Yes

3.4 Electro Optic (EO) Modulation

Light is coupled to the chip under test through a tunable laser, a polarization controller, and a lensed fiber, and transmission data is gathered using a power meter and normalized to reduce coupling losses. The coupling state of each device is obtained by tracking the extinction ratio of the resonances as a function of the ring-waveguide gap (for a fixed wavelength). As a result, the mean and standard deviation of the loss created by each bonding type may be calculated from the transmission spectra collection of resonances. The device under test achieves its half-wave voltage value by simply expanding the device length and decreasing the electrode gap while preserving the high electrical and optical field overlap at the LiNbO3 region. The confinement factors in these two cores are sensitive to Si3N4 ridge width because the Si3N4 waveguide and the LN layer have almost the same index. The ridge width and Si3N4 input waveguide width are designed to provide a confinement factor of 1.0 in the LN core. The width of the Si3N4 ridge reduces linearly once input light enters the bonded area with an LN film top, allowing the bulk of the mode to adiabatically migrate upward into the LN layer. Through the Si3N4 waveguides, TE polarized light is coupled in and out. The performance of the electro-optic system can also be increased by reducing the distance between the two electrodes. This can be done with a dicing machine, which

allows for more precise cutting. We propose a two-material core cross-section for creating hybrid waveguides in LN/SN, consisting of a few hundred nanometer single-crystal thin film of LN and SN bonded face-to-face.

3.4.1 Evolution of LN EO Modulators

LN is often described to as the "silicon of photonics," implying that it is as important in photonics as silicon is in microelectronics. This is due to the fact that LN has a wide optical transparency window, a strong EO (Pockels) effect, and a high glass transition (Curie) temperature, all of which are important for process compatibility and stable operations. Commercial off-the-shelf LN solutions have been widely adopted as a "workhorse of optoelectronics" for decades and are still commonly utilized at the ends of millions of optical fibers today due to their exceptional physical and chemical qualities. Several decades of research and optimization have resulted in designs that are still employed in practically all commercial LN systems. The legacy LN platform has three significant drawbacks: (1) Because of the low index contrast, the optical mode sizes are enormous, restricting the location of the electrodes and hence the EO modulation efficiency. (2) The LN substrate's high dielectric constant necessitates voltage–bandwidth trade-offs in order to accomplish the required velocity matching between microwave and optical signals for high-speed operations. (3) Because of the modest optical index contrast, bending radii above 1 mm prohibit dense integration. As a result, such a historical system is incompatible with modern PIC performance and integration requirements.

The lack of a single crystalline thin layer and the lack of smooth and scalable etching procedures were the key roadblocks in producing high-confinement channel type optical waveguides in LN, such as silicon. TFLN, in particular, may be transferred to silicon substrates with great yield using room-temperature bonding techniques. The mechanical properties of LNOI on Si wafers are similar to those of SOIs, making them far more resistant to thermal and mechanical shock than bulk LN substrates. In the late 2000s and early 2010s, the development and commercialization of LNOI wafers (e.g., NanoLN, Partow Technologies, NGK Insulators, TDK Corporation) provided the groundwork for the rapid rise of research in high confinement LN photonics [81].

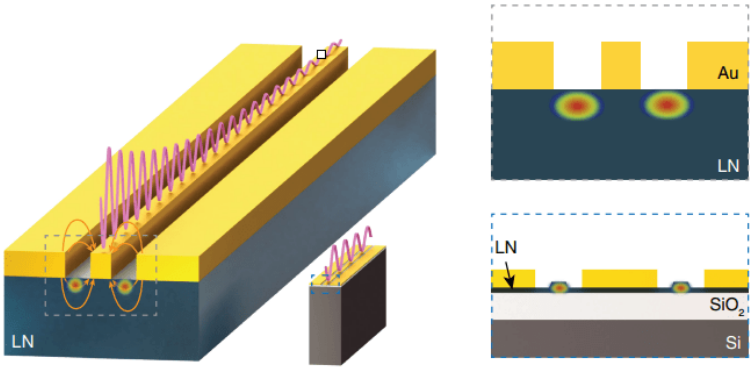

Figure 3.1: TFLN devices and cross-sectional views [81].

The study on LN dry etching has been accelerated by the growing interest in the fabrication of micro photonic and nanophotonic structures in LN thin films. Because the nonvolatile lithium fluoride byproducts created by typical fluorine based etching hinder further etching and cause rough edges, high-quality dry etching of LN at the micrometer scale has been a difficulty for years. LN nanofabrication techniques have been rapidly developed and iterated since the availability of LNOI wafers [82]. Smooth and repeatable etching has been demonstrated utilizing purely physical methods such as argon ion milling or reactive-ion-etching procedures. Optimization of such techniques resulted in a reduction in optical waveguide loss from >10dB/cm to 0.3 dB/cm [82]. Furthermore, heterogeneous and hybrid techniques based on rib-loading or chip/wafer bonding have progressed dramatically, achieving similar levels of loss. These platforms either employ hybrid waveguides, in which the optical modes are partially restricted within the LN thin films, or evanescently link light between the LN thin film and other material layers.

3.4.2 Phase Shifter in Integrated LN Modulators

A thin-film LN modulator's design goal is to increase the applied electric field strength in the optical mode area while retaining or improving other desirable properties. Because LN is an anisotropic EO material, the crystalline cut and device geometry must be chosen carefully to maximize the EO effect. There are two broad kinds of modulator design, similar to traditional LN modulators: one with the crystal axis (z axis) in plane with the wafer, x-cut or y-cut, and the other with the crystal axis out of plane, z-cut. The guided optical mode, which suffers a refractive index change as a result of the applied electric field, is sandwiched between two electrodes with opposite polarity in this configuration. A rib/ridge type of structure is widely used to arrange metal electrodes next to each other on a thin-film LN to introduce strong optical mode confinement. The optical field aligns with the strongest external applied field when light is propelled in transverse electric modes [83].

Because of the significant permittivity contrast, a thin slab in the monolithic technique dramatically reduces the effective electric field in the LN rib area. As a result of the boundary condition of the electric displacement fields, there is a substantial voltage drop in the passive dielectric outside the LN core region. A thick slab results in poor optical confinement, a greater bending radius, and bigger electrode gaps. To enable EO modulation in the hybrid technique, an LN slab is required. For hybrid structures, a well-engineered ratio between slab and rib thicknesses is critical for increasing modulation efficiency while maintaining appropriate optical confinement and a small bending radius. While adjustments for various performance goals can be performed, the index contrast between the LN and cladding ultimately determines the level of optical confinement that can be achieved, resulting in typical DC $V\pi$ ×L values of 1.53 V cm [95]. The strongest component of the applied electric field required in a z-cut LN modulator design is out-of-plane. The guided optical mode is positioned beneath the signal electrode to facilitate effective modulation, and light is launched in transverse magnetic modes to align with the strongest component of the external applied field. To prevent severe metal absorption losses, a low-index buffer layer (e.g., SiO2) is often required between the optical waveguide and the electrode. To ease

electric field penetration through the high permittivity LN regions, a thin-slab layer is still commonly used in this z-cut design. To produce a high vertical electric field, a signal electrode can be patterned on top of the LN film. To achieve a high vertical electric field, the buffer layer between the LN film and the top electrode can be made considerably thinner or even deleted, depending on the accepted range of slab material index and optical loss.

3.4.3 MZI Design in Integrated LN Modulators

A travelling wave MZI is typically used to convert a phase shifter into a high-speed intensity modulator. The input light beam is split into two routes in a MZI modulator (MZM), and an optical phase difference is created between the two arms using EO phase shifters, resulting in a change in the output intensity when the two paths are merged. A push–pull electrode arrangement, in which one arm's phase is advanced while the other's is delayed, is a common way to reduce the single arm $V\pi \times L$ value. The wave matching criterion must be satisfied in a travelling wave MZM: the optical wave must travel at the same speed as the electrical signal. The modulation effect can continue to accumulate when the optical group and electrical phase velocities are matched, as long as (1) the velocity matching condition is maintained, (2) the microwave signal is not heavily attenuated, and (3) the impedance of the RF transmission line matches well with the external electronics, allowing efficient microwave transmission [84]. Matching RF and optical velocities in x-cut devices has traditionally been difficult. To speed up the RF mode, a buffer layer and thick electrodes (>10 μm) are frequently utilized to draw it out of the high-permittivity LN crystal, at the penalty of diminished EO modulation efficiency. With a thin metal layer (1μm) and no dielectric buffer layers, velocity matching and low RF loss can be obtained in thin-film x-cut designs employing a low-permittivity substrate such as SiO2. The x-cut thin-film LN's design flexibility makes it a common crystal cut choice and leaves room for further optimization. The cross-section of the heterogeneous TFLN EO modulator optical waveguide is shown in Fig. 3.2.

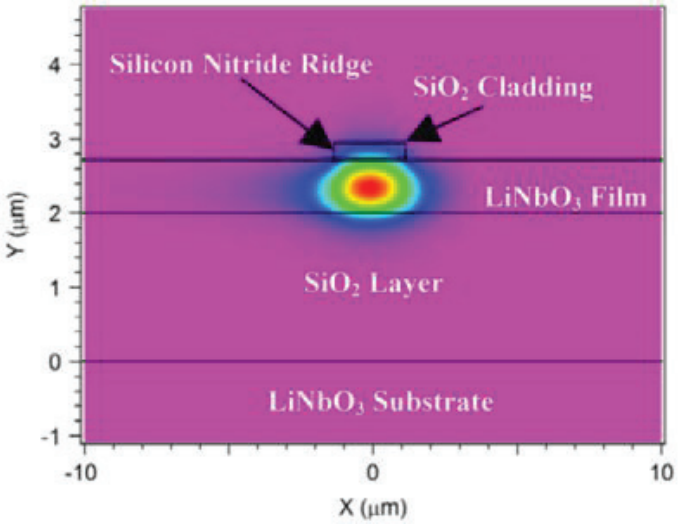

Figure 3.2 Hybrid TFLN optical modulator [73].

Unlike x-cut/y-cut EOMs, z-cut electrodes do not readily enable a symmetric push–pull configuration for a single electrical drive. The electric field strength experienced by the optical waveguide beneath the ground electrode is typically 3–10 times weaker than that experienced by the waveguide beneath the signal electrode in this configuration resulting in significant chirp. To ensure chirp-free operation, varying electrode arrangement relative to waveguides and crystal domain inversion may be required. However, shorter electrodes both x- and z-cut designs can attain a substantially greater EO bandwidth than typical LN EOMs.

3.5 Simulation Results

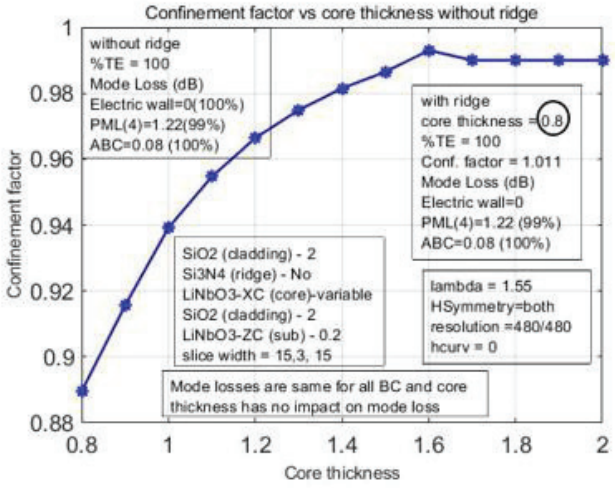

Figure 3.3 Variation of core thickness without ridge for different boundary conditions (BC)

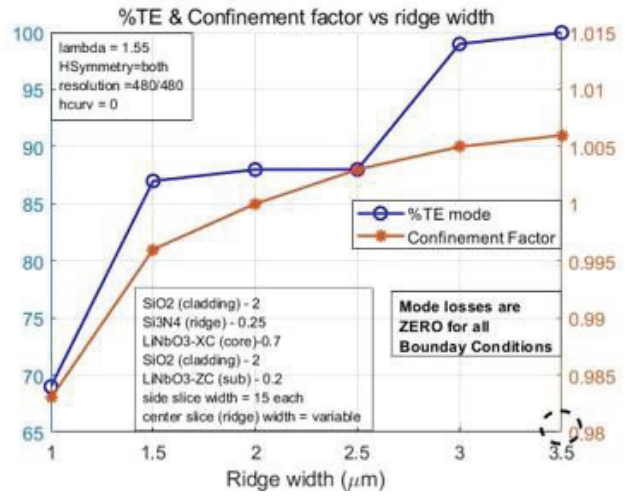

Figure 3.4 Impact of ridge width on TE mode, confinement factor and mode loss for different BC

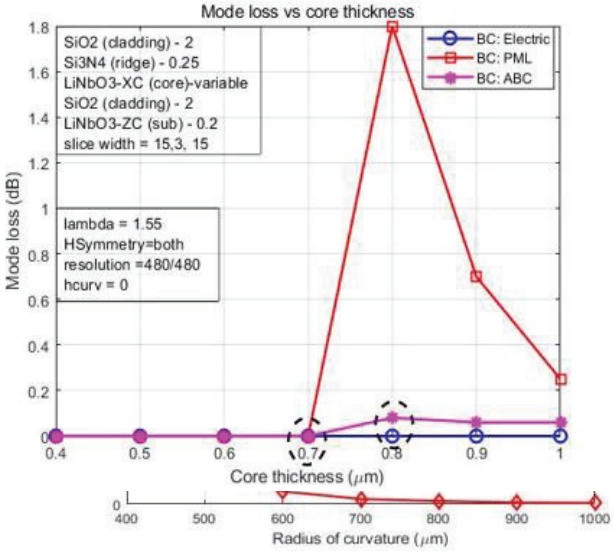

Figure 3.5 Mode loss vs core thickness.

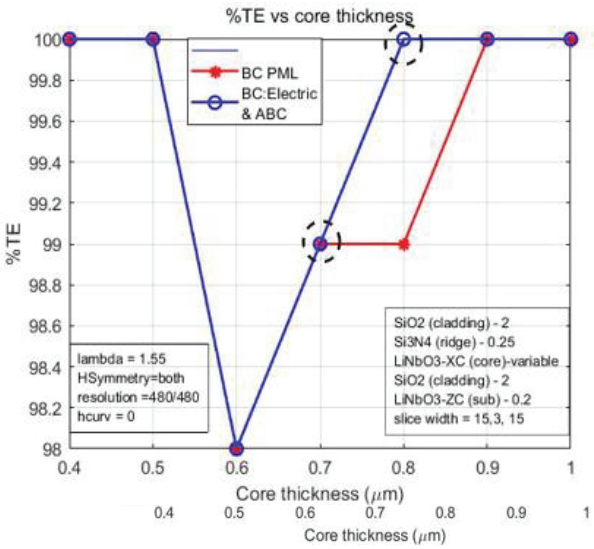

Figure 3.6 Percentage of TE mode vs core thickness.

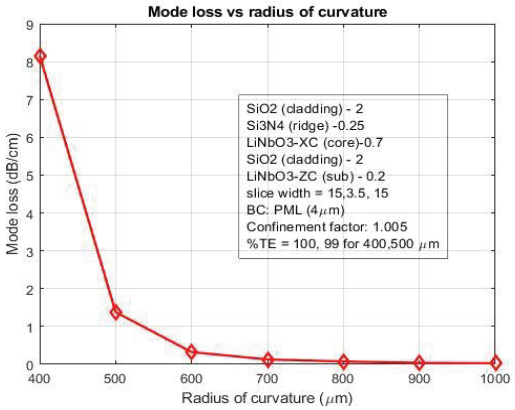

Figure 3.7 Effect of bending loss with curvature.

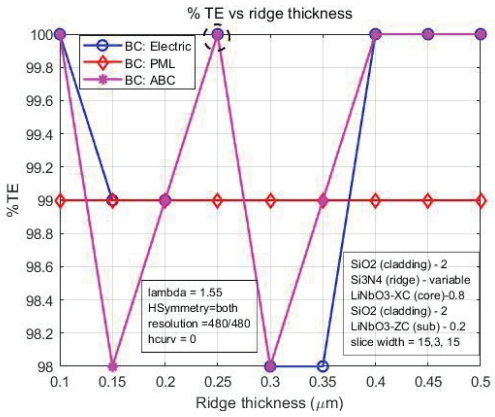

Figure 3.8 TE mode vs ridge thickness.

Confinement factor (CF) increases with core thickness (Tcore) whereas mode remains unchanged. Tcore = 1.6 μm for slab waveguide as seen in Figs. 3.3, 3.4 and 3.5. The optimum value of core width is Optimum value of ridge width = 3.5μm. According to the Figs. 3.6, 3.7 and 3.8, optimum value of core thickness is 0.7μm.

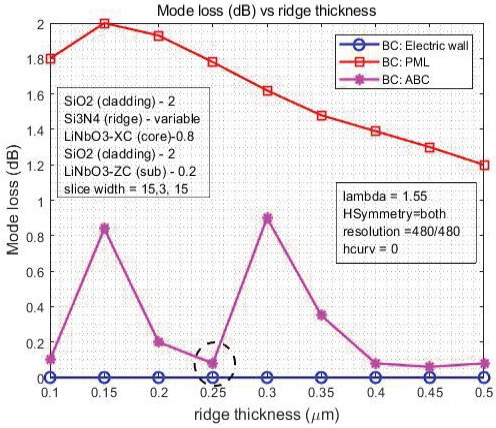

Figure 3.9 Mode loss vs ridge thickness.

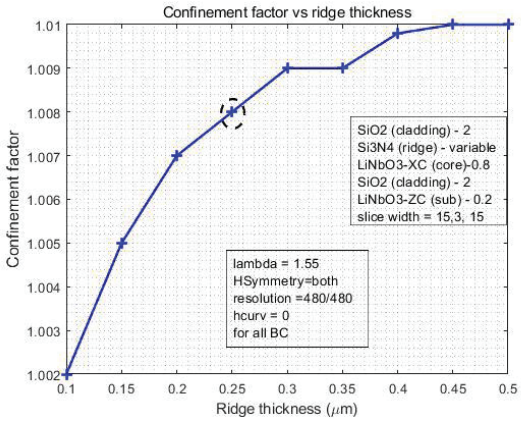

Figure 3.10 Confinement factor vs ridge thickness.

Changing of ridge width do not make any impact on percentage of TE, confinement factor and mode losses under all boundary conditions without bending. Reducing the ridge thickness and core thickness makes lower the confinement factor whereas %TE and mode losses under all BC remain unaffected [Fig.13]. However, the best condition is achieved varying core material ridge width=3.5μm, ridge thickness= 0.25μm, core thickness=0.7μm. In addition, performance of mode loss is better for X-cut LiNbO3 as a core material using bending. Note that the fundamental guided TE-like mode is strongly confined to LN core than TM-like mode. As a consequence, fundamental TM-like mode is ignored in this study.

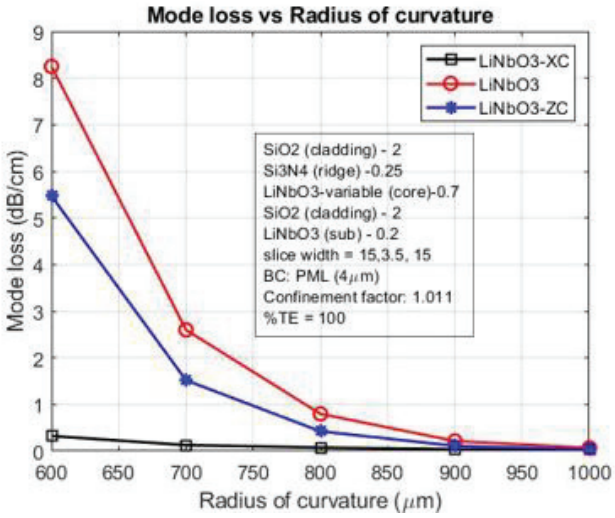

Figure 3.11 Mode loss vs radius of curvature.

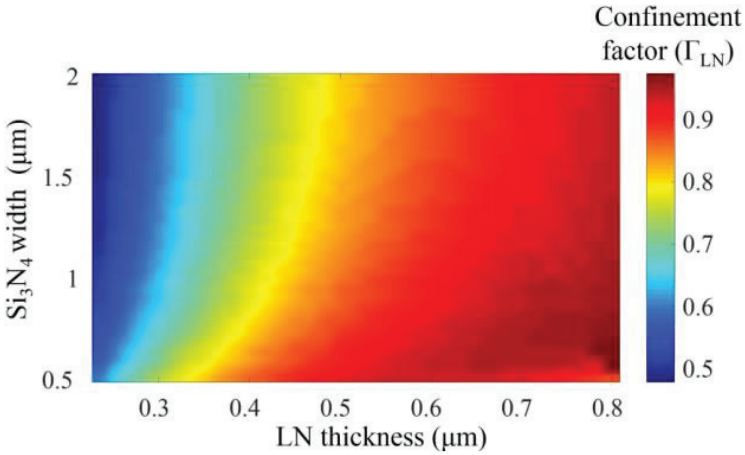

Figure 3.12 Simulated mode confinement factor in LiNbO3 as a function of Si3N4 strip width and LN film thickness for the fundamental TE mode.

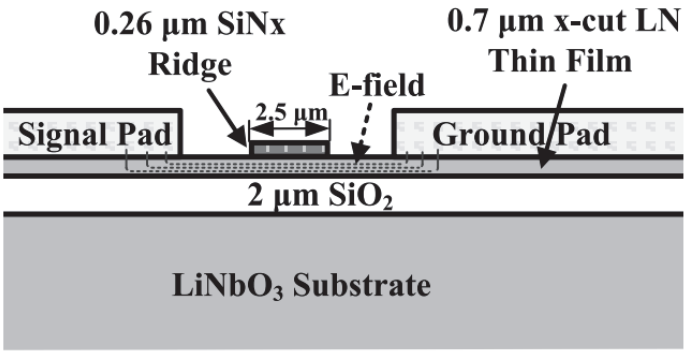

Figure 3.13 TFLN hybrid modulator optical waveguide.

Figure 3.14 TFLN layout in FIMMWAVE.

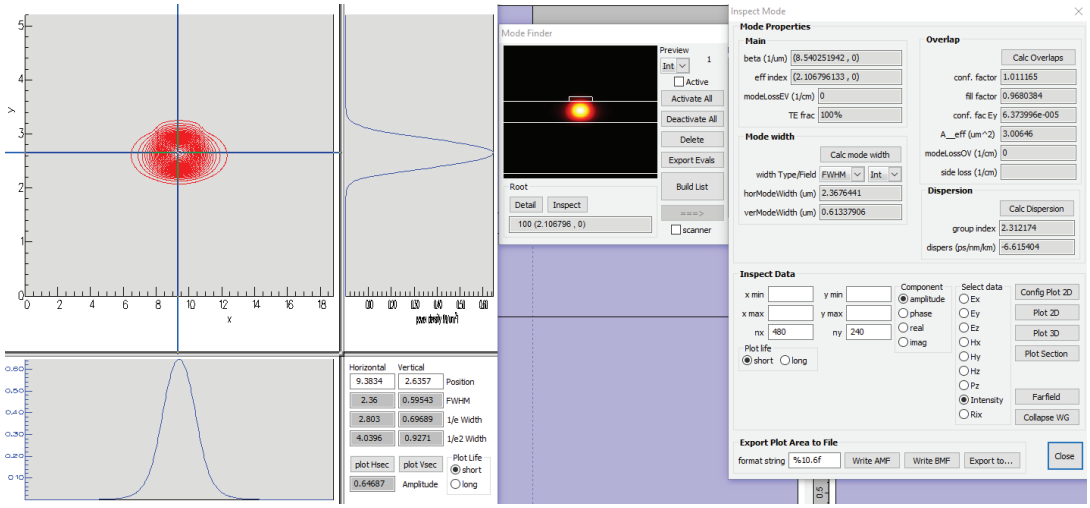

Figure 3.15 Intensity mode profile of given TFNL hybrid modulator.

3.6 Research Opportunities and Roadmap

With the exponential traffic growth in telecommunications, the Internet, data center, and Internet of Things, an optical switching matrix with a fast switching speed, non-blocking throughput, wide bandwidth, low loss, and low crosstalk is highly demanded. To realize these required specifications, the switch topology and the fabrication platform are two key factors in the development of optical switch matrix. The conventional planar lightwave circuits (PLCs) based switch technology is well known for its high extinction ratio and low loss, but usually has a large footprint and high power consumption due to the low index contrast and the low thermo-optic coefficient. On the other hand, the SOI-based optical switch has been viewed as a promising candidate by virtue of its compact size, fast switching time, and compatibility with the complementary metal-oxide semiconductor fabrication process. However, the array of the SOI-based optical switch is limited to less than 32 I/O ports due to both high insertion loss and high crosstalk; meanwhile, the operating wavelength is restricted in the near infrared.

In general, more advancements in fiber-to-chip interface coupling, careful consideration of electrical, RF, and optical packaging, and thermal/temporal reliability and stability studies are planned to be made soon in order to commercialize fully-packaged TFLN devices. Another area that is expected to attract a lot of research is heterogeneous integration of active elements like lasers, amplifiers, and photodetectors, as well as various TFLN components on a single photonic chip for a variety of applications like optical communication transceivers, high-performance computation, analogue, digital, and quantum communication and LiDAR systems. Backend of line heterogeneous integration with SOI and SN photonic circuits appears to be the most expected method to be explored for low cost, large-scale, and foundry compatible TFLN device deployment.

In the case of EOMs, one of the next stages required for sophisticated communication systems is to achieve modulation BWs over 100 GHz. EOMs have been demonstrated to have promising sub terahertz applications in studies. It should be highlighted, however, that fully realizing integrated EOMs with such high BWs will necessitate the development of ultrahigh-speed electrical and photonic drivers, as well as detecting components. The achievement of higher modulation formats for coherent optical communication, which has yet to be shown in the TFLN platform, is another critical milestone. In the near future, it is expected to demonstrate nonlinear devices on TFLN with improved performance by lowering insertion and propagation losses, optimizing poling conditions for PPLN waveguides, or improving the efficiency of other phase-matched waveguides. The integration of standalone nonlinear devices into more system-like applications, such as optical isolators, is also an interesting path to pursue. Heterogeneous integration of third order nonlinearity materials onto TFLN and cascaded nonlinearity using this heterogeneous platform is also a promising direction that paves the way for a variety of interesting applications such as highly efficient high-harmonic generation, frequency-stabilized optical frequency combs, and mid-infrared wavelength generation.

3.7 Summary

Over the last few decades, LN's diverse material characteristics and exceptional optical qualities have been widely explored. This adaptable material has proven to be one of the most appealing photonic platforms, particularly in the markets for electrooptic modulators and wavelength converters. The challenges and drawbacks of bulk LN have recently been overcome with the introduction of thin-film LN technology, and standalone TFLN devices are outperforming their bulk counterparts in terms of key performance parameters such as waveguide propagation loss, modulation BW for EOMs, and conversion efficiency in the case of wavelength converters. In order to meet the ever-increasing demands of largescale integration in current electronic-photonic systems, the TFLN technology also provides remarkable reductions in power consumption and overall device footprint. Thanks to the new availability of high-quality thin films of lithium niobate, the electro-optic modulator area is undergoing a revolution. Lower driving voltages, higher bandwidths, and more compact modulators have been developed using an integrated thin film platform. Thin films can also be attached to a variety of substrates for heterogeneous integration without causing damage to the films, allowing for construction flexibility not present in bulk LN modulator systems and potentially leading to the development of wafer-scale hybrid modulators. This chapter study discussed recent advancements in the field as well as design and manufacturing considerations for the hybrid SN-LN modulator platform. A sampling of future hybrid technologies at visible and mid-infrared wavelengths is also considered, as well as layer thicknesses for a single platform designed for best performance across the entire telecommunication wavelength range (1260–1675 nm). The recent developments in EO modulators point to a bright future of unique device designs and applications.

CHAPTER 4

High Resolution Panoramic C-band Spectrometer

4.1 Introduction

In this chapter, the design architecture of compact on-chip high-resolution broadband spectrometer contemplating Mach-Zehnder delay interferometers (MZDI), 3dB multimode interference (MMI) couplers and 2×2 directional couplers are presented and verified by software simulation. The ability to configure network functions, protocols, and make optimal use of spectrum is made possible by monitoring the state of the optical network. This chapter discusses the architecture for compact on-chip spectrometry targeting high resolution across the full C-band to assess the spectral profile of WDM signals precisely in fixed-grid and flex-grid topologies. The proposed architecture circuit is composed of a scanning ring resonator followed by a parallel arrangement of arrayed waveguide grating (AWGs) with interlaced channel spectra. The comb of ring resonances provides the high resolution, and the algorithm creates a virtual tunable AWG that isolates individual resonances of the comb within the flat passband of its synthesized channels. The parallel arrangement of AWGs may be replaced by a time multiplexed multi-input port AWG. The MZDI stage enables alignment of the RR resonances with the MZDI-AWG channels as the comb is scanned over a free-spectral range (FSR). A merit of this architecture is that it requires a minimum number of thermo-optic phase-shift elements for setting bias points and for tuning which minimizes power consumption of a demonstrator. The fabrication expected access to multi-project wafer MPW runs for test structures, followed by a custom wafer run for fabrication of prototypes for demonstration, in order to make efficient use of resources. LioniX International foundry offer MPW runs for designs using the low-cost photolithography with a feature size of $1\ \mu m$ and asymmetric double strip (ADS) waveguide. The components simulations that supported the assessment of the feasibility of a spectrometer compliant with the specification made use of the LioniX single strip (SS) waveguide with a $450\ nm$ minimum feature size. A merit of the change of waveguide structure is that a proven spot size convertor that efficiently couples light from standard single mode fibre to the ADS waveguide is available as a library component in the LioniX process development kit (PDK). Access to the PDK, has enables the update of the materials database used in simulations with the precise optical properties of the materials used in the LioniX process including the dispersion of the refractive index across the C-band. The SS waveguide and especially the smaller minimum feature size offered more scope for performance optimisation and minimisation of footprint. Nevertheless, while the design details change with the use of the ADS waveguide and MPW, the performance parameters of most components are substantially unaffected.

4.2 Theory

Optical performance monitoring (OPM) is the key enabling technology for reliable spectrum management. Up-to-date network telemetry is required for capacity scaling, network or component fault recovery, and network reconfiguration through performance prediction and planning. The monitoring includes information on optical signal-to-noise ratio (OSNR), electrical signal-to-noise ratio (ESNR), loss, bit-error-rate (BER), and power. In practice, optical performance monitoring may be based on the measurement of one or several parameters. However, OPM is used herein to refer to "power" monitoring since power is one of the key indicators of performance in optical systems.

In transport optics (e.g., WDM networks), spectral sensing is not straightforward. Traditionally WDM channels are distributed over the 40 nm wide fiber-optic C-band (1530 nm to 1565 nm) with fixed center frequencies arranged on the International Telecommunication Union (ITU) grid at intervals of 50 GHz or 100 GHz and an OPM card is used to measure the power [85]. The working principle of the OPM card involves sweeping a tunable filter with 50 GHz resolution over the spectrum to make available ITU grid channel power readings. Due to their excessive power consumption, size, and cost, OPM cards are deployed only at a few points in the network; typically co-located with reconfigurable add-drop multiplexers (ROADMs) [86]. However, current optical networks are elastic in nature, i.e., the channels are not located on a fixed regular grid, rather the channel center wavelength can be placed at an arbitrary location within the spectrum. The flexible grid can support a variety of channel power profiles (i.e., power spectral density and bandwidth) with a resolution of channel center frequency placement as fine as 6.25 GHz. Flex-ready spectrum measurements are required to facilitate the deployment of the flex-grid system. As a result, flex-grid ready ROADM architectures are equipped with new modules that can measure power at desired frequency location and resolution. However, due to cost issues, spectrum measurement is only performed at add-drop nodes and not at amplifier nodes. Moreover, a single OPM module is shared by the multi degree-ROADM, so the OPM measurement speed reduces as the number of lines it supports increases. The absence of OPM makes it difficult to have live and accurate network measurement; and hence it is hard to implement performance optimization.

A variety of different approaches to the problem of spectral sensing with high resolution across a wide band have been disclosed in the literature [87-89] but when scaled to combine acceptable resolution with wideband operation their practical implementation is most often not feasible due to excessive cost, loss and footprint. An integrated solution for a high resolution (sub-GHz) spectrometer to monitor the power across the entire conventional band remains challenging. The first stage is a tunable ring resonator (RR) that defines the resolution. The final stage is an arrayed waveguide grating (AWG) that isolates one RR resonance within each of its channels. The principal innovation is ganged tuning of the RR and AWG to retain the RR resonance at the center of the AWG channel passband. This is achieved by a second stage that uses an MZI to form a coherent superposition of two interleaved AWG channel spectra corresponding to a pair of input

ports. The coherent superposition of a pair of AWG input channels is replaced by the incoherent superposition of pairs of AWG outputs, which may be performed by processing the measured AWG channel powers. The MZI stage is eliminated, releasing the spectrometer from any requirement to control inter-stage optical path lengths, and thereby significantly easing manufacture.

The proposed architecture combines a RR and a number M of AWGs with interleaved channel spectra. For the purpose of exposition, the $M = 2$ case is first considered but subsequently generalized. Hardware economies may be made by replacing the multiple AWGs by a single time multiplexed M-input AWG. A number of ample reports is carried out in the literature of the technological verification of spot size convertors (SSC), multimode interference couplers, tunable RR, and sub-circuits such as Mach-Zehnder interferometers [90], [91] and high port count AWG [92] fabricated using the Si3N4 integration platform. LioniX have reported extremely low loss typically $0.1 - 0.2\ dB\ cm^{-1}$ in the 1580-1610 nm wavelength region. A merit of the change of waveguide structure is that a proven spot size convertor that efficiently couples light from standard single mode fibre to the ADS waveguide is available as a library component in the LioniX process development kit (PDK). The SS waveguide and especially the smaller minimum feature size offered more scope for performance optimisation and minimisation of footprint. Nevertheless, while the design details change with the use of the ADS waveguide and MPW, the performance parameters of most components are substantially unaffected. The exception is the footprint of the AWG which must be scaled-up to accommodate the larger minimum feature size. A simple but novel signal processing approach enables the spectrometer to scan the entire C-band with high resolution ($\sim$1GHz) using only one dynamic control. The original signal processing method renders the proposed architecture robust to fabrication tolerances.

4.3 Spectrometer Circuit Architecture

The suggested circuit architecture of the spectrometer is shown schematically in Fig. 4.1. A ring resonator is the initial stage, and its purpose is to define the spectrometer resolution. It generates a periodic train of resonances, each with a bandwidth of 1GHz and spaced by the free-spectral range of the system. It can be tuned in frequency over a single FSR. An arrayed waveguide grating is used in the final stage to isolate one RR resonance in each output channel. The -3dB passband width of each channel is half the channel spacing. The frequency spacing of the output channel is equal to the RR's FSR. The central stage's job is to ensure that the center frequency of each AWG output channel passband tracks the center frequency of their respective RR resonance as closely as possible. It is made up of a mirrored pair of ostensibly identical Mach-Zehnder delay interferometers with an FSR equal to the AWG channel spacing and thus the RR's FSR. The MZDI can be built with either 2x2 directional couplers or MMI couplers. The frequency spacing of the AWG input channels is half that of the AWG output channels. The MZI that comes before the MZDI pair is utilized as a switch to select the active MZDI and hence the active pair of AWG input channels of the four AWG input channels that are equipped.

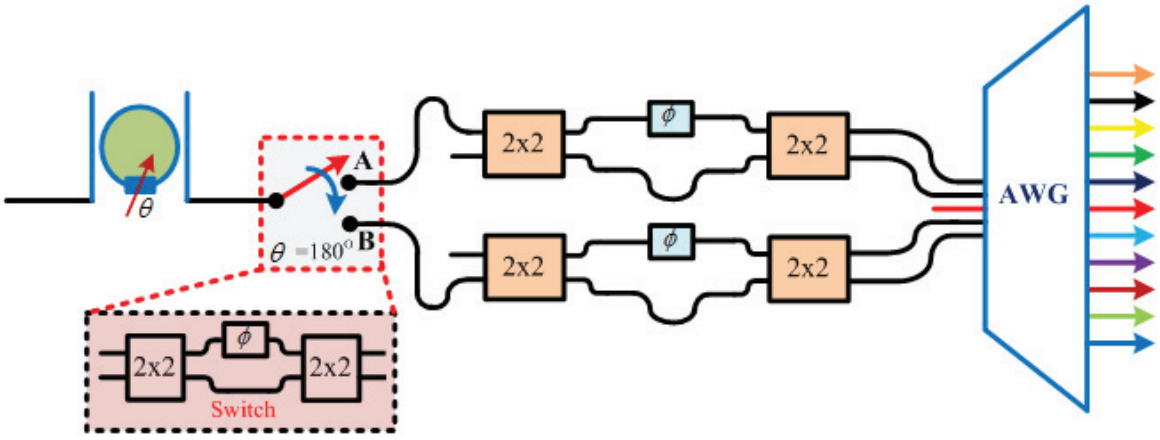

Figure 4.1 Schematic of the proposed spectrometer.

There are two controls on the spectrometer: one to tune the RR and another to flip the MZI switch. A phase shift element provides a $\Delta\theta \in [0,2\pi]$ phase change within the RR, which is used to scan the RR resonant frequency comb cyclically over one FSR. This operating cycle has two phases that correspond to the state of the switch. The switch toggles between the scan's midpoint and endpoint, as indicated by the first control. The only dynamic controls required are these two. However, to compensate for phase bias errors caused by manufacturing process fluctuations, the MZDI stages should be equipped with quasi-static (pre-set) phase trimmers.

The FSR and the total number of AWG output channels necessary to function over the full C-band can be chosen with some flexibility. The practicality of the spectrometer demonstration is supported by reported experimental demonstrations of the components and circuit simulations which combines a 50 GHz Micro RR (MRR) and an 88×50 GHz AWG. Table 1 shows the specifications of the proposed circuit design. For a RR FSR of 50 GHz, the required number of AWG output ports is 88 to cover the entire C-band.

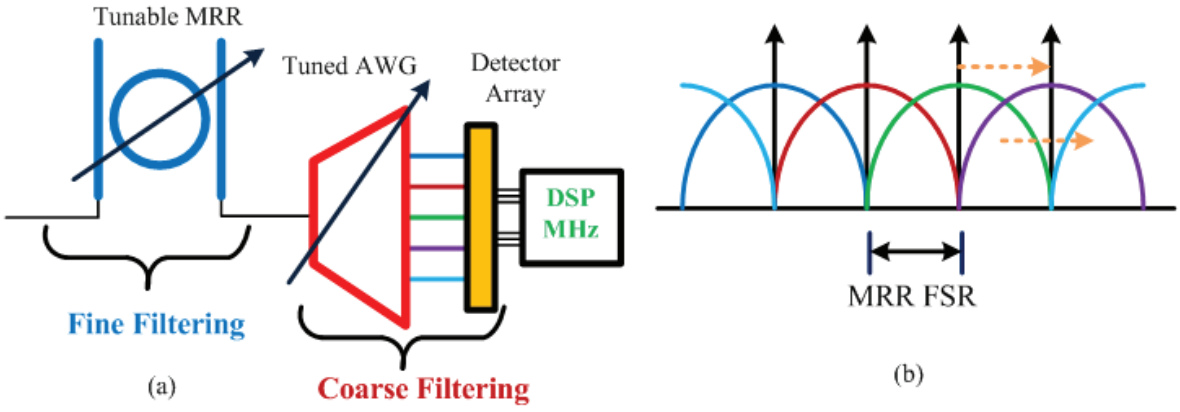

Figure 4.2: (a) Tunable ring resonator & AWG; (b) Tracking of RR comb.

As the spectrometer is scanned, the comb of AWG passband center frequencies should ideally track the comb of RR resonant frequencies to isolate an individual RR resonance within an AWG channel, as shown schematically in Fig. 4.2. (a, b). The following are some of the advantages of

ganged tuning: reduced excess loss, tuning invariant channel transmission, and AWG neighboring channel crosstalk that is the best (passband center) rather than the worst (passband edges).

Table 4.1. Detail design specifications of the circuit architecture.

Design specifications	Values	Remarks
Free spectral range (GHz)	50	
AWG output channel spacing (GHz)	50	equal to the FSR of RR
AWG output channel bandwidth (GHz)	20	~ ≤ 1⁄2 AWG output channel spacing
AWG input channel spacing (GHz)	25	half of AWG output channel spacing
Number of AWG output channels	88	
Total spectrum covered (THz)	4.4	88 × 50 = 4400 GHz (C band)

4.4 Integration Platform

The proposed spectrum monitoring device can be fabricated in any mature photonic integration platform. If the excess loss of the ring per turn is negligible in comparison to the power coupled out per turn, the resolution bandwidth is determined by the power cross-coupling ratio of the couplers. The minimum detectable power of the spectrometer is determined by the total excess loss of its components of which the insertion loss of the RR is most likely the primary contributor and the MZDI-AWG the secondary contributor. As a result, an integration platform that supports loss-loss waveguides and careful consideration to the design of RR couplers to reduce excess loss are essential. Consequently, the CMOS compatible Si3N4 photonic integration platform is chosen to match the specifications of the proposed spectrometer because it provides low loss, low dispersion waveguides, tight confinement, and a mature thermo-optic phase shifter technology. The platform also offers good prospects for further loss-reduction and to lower power consumption, temperature insensitive, alternatives to thermo-optic phase-shift elements [90].

Software simulations of all passive spectrometer components: fibre to planar waveguide couplers (‘spot size converters’ SSC); multimode interference couplers (MMI); directional couplers (DC); tunable RR; and sub-circuits: MZDI and AWG; have been performed. Waveguides with different structures were evaluated but a single strip (SS) waveguide (300 nm thick core, 500 nm -1200 nm width, 450 nm minimum feature size) of the LioniX Triplex Si_3N_4 integration platform, was selected for component and sub-circuit simulations with width transition tapers as necessary. The simulation results were found to be compliant with the specification.

4.5 Technological Validation & Integration Feasibility

The feasibility of the whole system is demonstrated using industry standard simulation tool and verified experimentally. A combination of industry approved software simulation tools is used to validate the concept. For example, VPIphotonics is used for the circuit simulation whereas, the Photon Design suite of tools and OptiBPM are used to validate the function of each component in the given architecture. If the excess loss of the ring per turn is negligible in comparison to the power coupled out per turn, the resolution bandwidth is determined by the power cross-coupling ratio of the couplers. The excess ring loss consequently limits the achievable resolution. An

integration platform supporting the design of low-loss waveguides and low-loss waveguide bends is therefore paramount concern.

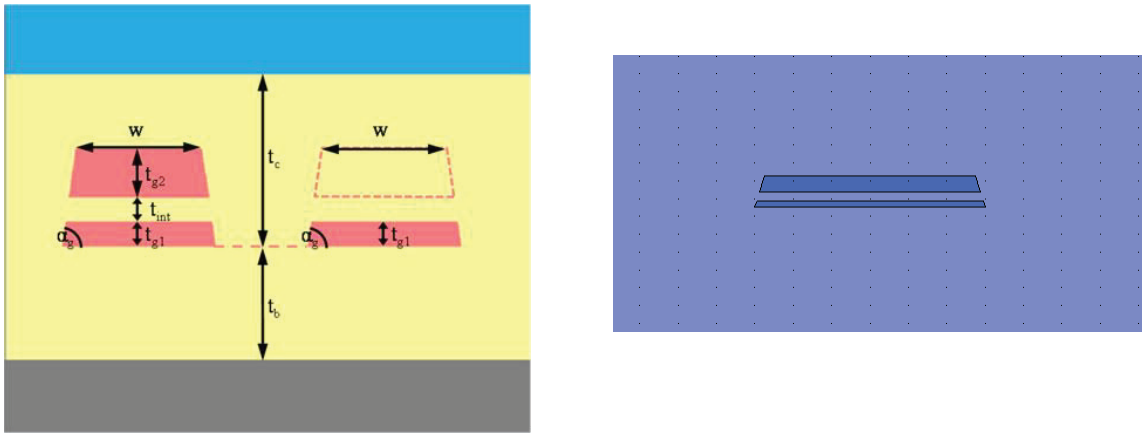

Figure 4.3 Definition of the cross-sectional parameters of the ADS waveguide (left). The thicknesses of lower strip, the gap and the upper strip are 75 nm, 100 nm and 175 nm, respectively. The black area is Si (silicon) substrate while the yellow area (cladding) is SiO_2 (silica) and red parts (cores) are Si_3N_4 (silicon nitride). The waveguides are placed a distance of $t_b = t_c = 8\ \mu m$ distance from the lower and upper limits of the cladding. The ADS waveguide simulated in the FIMMPROP is shown right window [89]

The reference ADS (asymmetric double strip) used in the LioniX MPW waveguides is shown in Fig. 4.3 where the width of the top side of the upper strip is 1100 nm and the etching results in sidewalls inclined at 82° relative to the horizontal axis. The simulations of the components and subcircuits are designed using ADS as reference waveguide. The waveguide characteristic over full C-band is obtained by using the Photon design software tool FIMMWAVE. TE-like mode is used in all the simulation due to its tight confinement, hence it exhibits lower bend loss in comparison to the TM-like mode. The effective refractive index of the mode at the at the smaller wavelength edge (1530 nm), center wavelength (1545 nm), and the longer wavelength edge (1565 nm) of the C-band is found to be 1.7725, 1.76841 and 1.7629 respectively.

Figure 4.4(a) shows the schematic diagram of a RR. As shown, it requires two directional couplers (DC). The resolution of the spectrometer is largely set by DC power cross coupling and is determined by the spatial gap between the interacting waveguides. A variety of numerical and quasi analytical methods involving different approximations are used to bracket a range of gaps targeting 2-6% power coupling. 2.5D FDTD uses effective index mode (EIM) solvers which cannot correctly model couplers. The eigenmode expansion (EME) method has problems modelling curved structures – it can be used in conjunction with a circuit simulator (PICWAVE, VPI) for very small FSR large racetrack rings, but it displayed an excessive computational power loss in the curved waveguide coupler of the 50 GHz ring.

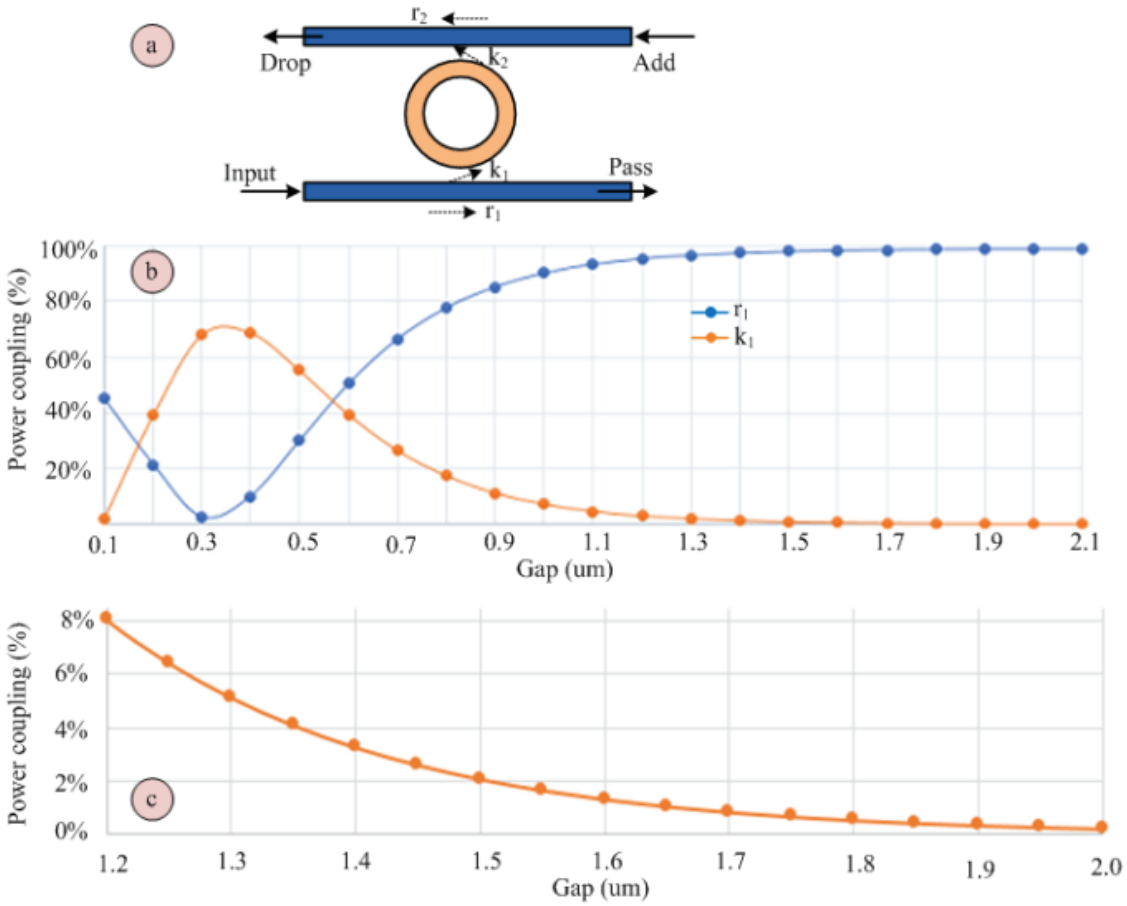

Figure 4.4 (a) Schematic diagram of a RR; (b) power coupling between the ports of a directional coupler as a function of spatial separation; (c) power coupling at the cross port as a function of spatial separation.

In this work, a semi-analytic method informed by a mode solver was applied to the problem. The mode solver tool (Photon Design MOLAB) is applied to find the fundamental symmetric and antisymmetric local eigenmodes to provide their effective index difference which is integrated over the interaction region using an adiabatic symmetry-based model that predicts the overall power transfer matrix of the proximate curved waveguides. An OptiBPM scanning of the power coupling as shown in Fig. 4.4(b) is also performed to validate the numerical calculation. Although the beam propagation method falls outside its domain of validity for this problem, it nevertheless predicted gaps in a similar range as the quasi-analytic method. The range of gaps is then sampled by test structures to enable the gap to be refined experimentally. The zoom in view of the power coupling at the cross port of the DC is shown in Fig. 4.4(c). Simulation result show that, for a gap of 1.3 um the power coupling at the cross port is 5% and it reduces to <∼1% for a gap of 1.7 um. For the MPW run, several ring resonators are laid out on the mask having gaps from 1.2 um to 1.8 um with 0.2 um increment with the objective that at least one RR works well. Two identical DC are used in the ring design. The ring circumference is calculated to be 3.3928 mm at 1545 nm for an FSR of 50 GHz using the following formula.

$$FSR(\omega) = c/n_g(\omega)l \tag{4.1}$$

where, n_g is the group index, l is the length of the delay line to obtain the specified FSR. The corresponding ring radius is 540 μm. Over the C-band, the bend loss of an ADS waveguide bend of this radius of curvature is insignificant; the mode is totally confined by the waveguide bend, and absorption and scattering loss are the only factors contributing loss. The waveguide loss is considered as 0.4 dB/cm in the simulation as a conservative assumption.

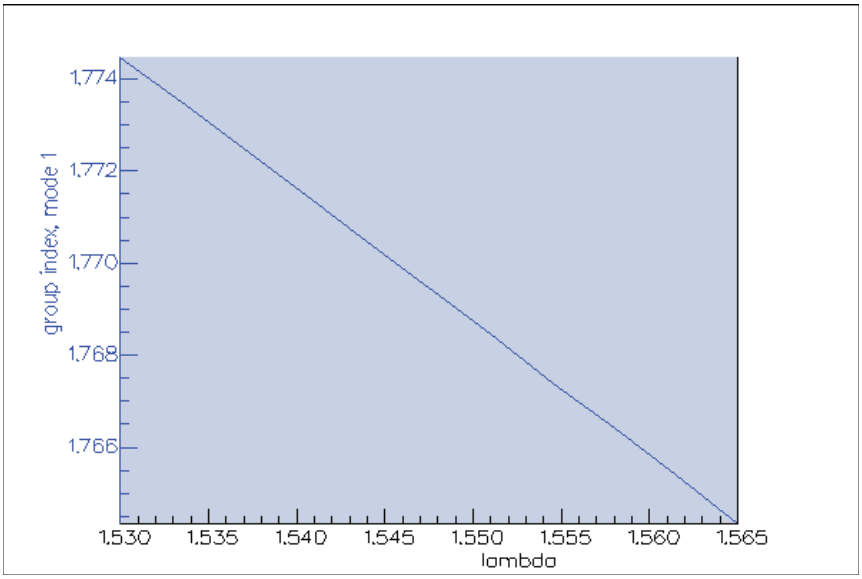

Figure 4.5 TE-like mode group index versus wavelength over the C-band.

Fig. 4.5 demonstrates the variation of group index in accordance with operating wavelength in C-band obtained by scanning in FIMMWAVE software. The dispersion of the mode group index is small and substantially linear with wavelength. For many purposes it may be neglected. However, it is responsible for the departure of RR resonant frequencies and AWG channel center wavelengths from a perfectly regular grid that is significant compared to the channel frequency spacing when accumulated over the whole C-band.

It is likely that this loss is attributable to the mode mismatch at both ends of the straight waveguides between the single waveguide fundamental l mode at the port and the lowest order symmetric and anti-symmetric modes of the dual waveguide that constitutes the DC. Typically, adiabatic S-bend access waveguides are appended to a straight waveguide coupling section. The separation between the access waveguides is thereby increased until the waveguides no longer couple significantly and may be treated as isolated waveguides. The access waveguides extend the region of coupling beyond the straight section which must be reduced in length to compensate. The addition of S-bend access waveguides eliminates the mode mismatch at the ports but it introduces two curvature discontinuities in each access guide which are now the main contributor to excess loss. However, it is not necessary to introduce any discontinuities within the ring. A circular ring may be coupled to an input-bypass waveguide that is a straight or a circular arc segment. Access waveguides may then be added to this section outside the interaction region, introducing no excess loss within the ring. The length over which the ring and input-bypass is extended and of the order of the ring radius. It will therefore be necessary to increase the minimum gap between the ring and input waveguide to retain the desired weak coupling. The increased slowly varying gap will also

eliminate loss due to conversion of the mode of an isolated curved ring waveguide (ring) and curved or straight input waveguide to the symmetric-like and antisymmetric-like modes of the ring-input waveguide pair in the interaction region.

4.6 Directional Coupler and MMI Coupler

A directional coupler is a device that joins two modes traveling in the same direction. This can be used as a beam splitter in its most basic form, but more complex devices can be employed as two-way switches or modulators; other variations can be used as filters or polarizers. These areas of the field must overlap spatially if two parallel guides are put near enough together. The inter waveguide space necessary for considerable overlap is usually on the order of the guide width. Figure 4.6 depicts the situation in two identical, neighboring symmetric slab waveguides for the lowest-order modes.

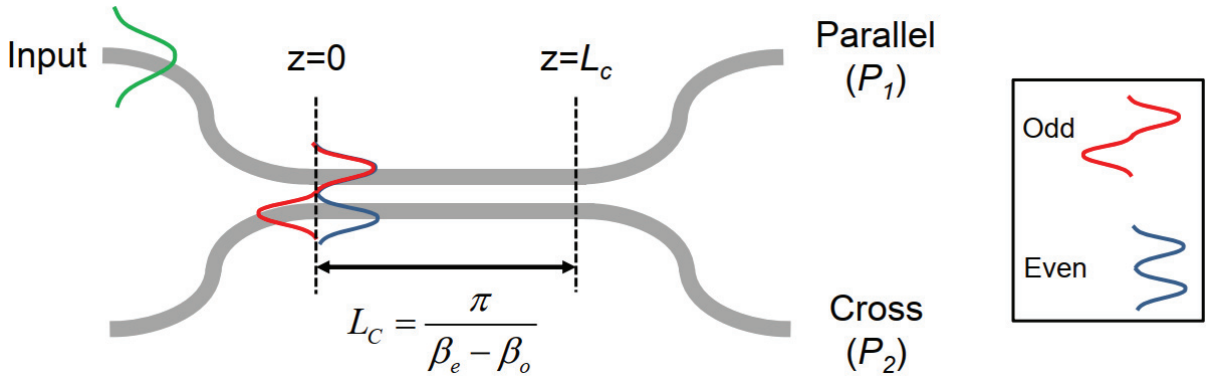

Figure 4.6 Schematic of basic directional coupler.

S-shape waveguides are used in the input and output ports of the directional coupler. The lower refractive index contrast between core and cladding allows higher bending radius. However, energy exchange in two parallel waveguides where interference occur in symmetric (even) and anti-symmetric (odd) shape.

The spectrometer circuit shown in Fig. 4.1 contains a total of three MZI sub-circuits formed by a total of six 2×2 3dB couplers. Three of these couplers have one nominally unused input port and might be replaced by 1 × 2 y-branch or MMI couplers with a centred input port. This strict mirror symmetry about the input port constrains the splitting ratio to 50:50. However, there is merit in the symmetry of an MZI formed by two nominally identical on-chip couplers. Moreover, the unused ports are available as test ports to aid set-up.

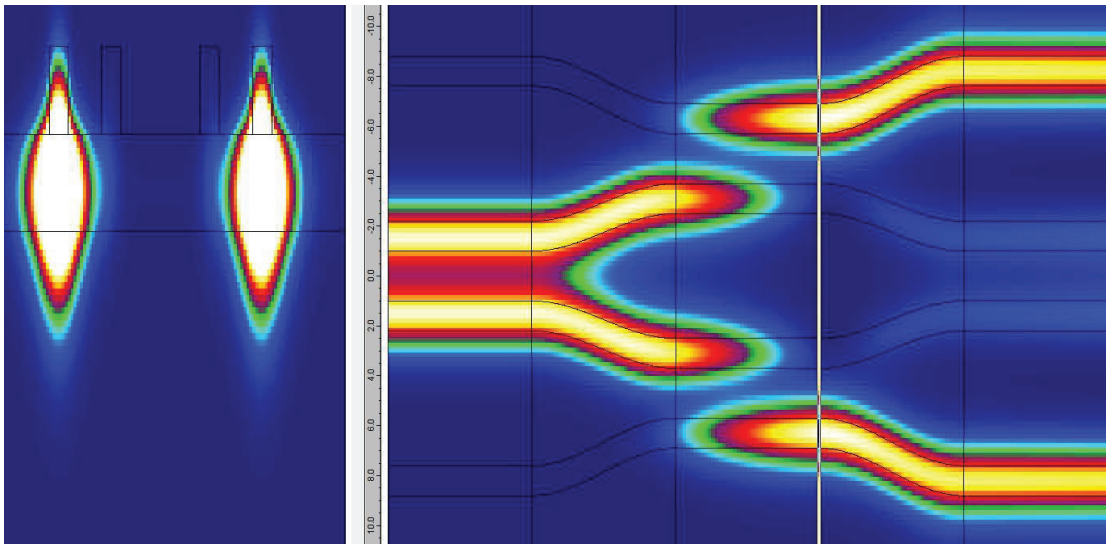

Figure 4.7 A schematic of 3dB directional coupler for ADS waveguides.

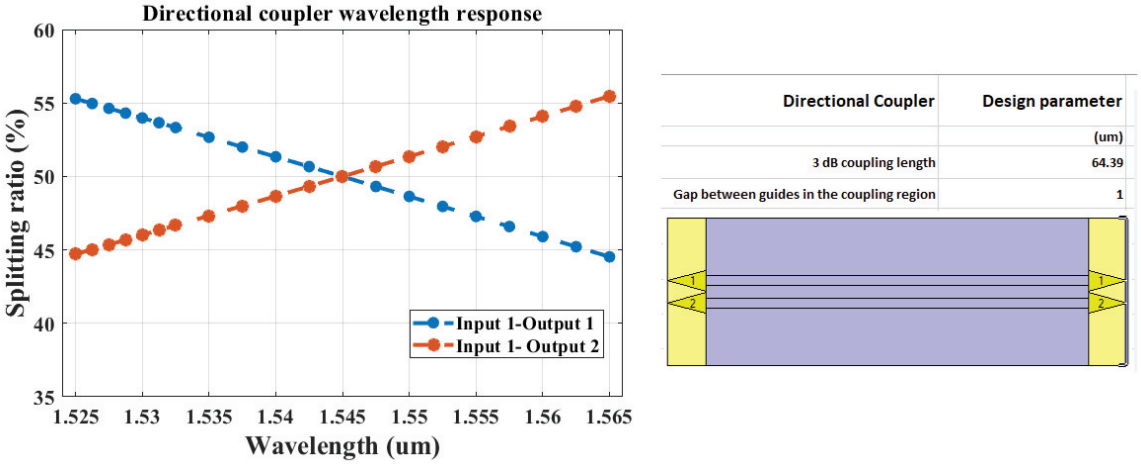

Figure 4.8 Splitting ratio of a 3dB directional coupler versus vacuum wavelength.

There are two parallel optical paths from the input to any output of the spectrometer each of which passes through four of these couplers. In addition to the insertion loss of the RR and AWG, the contribution to the total insertion loss of the excess loss of four couplers in series is a consideration. However, the use of MMI may cause additional insertion loss which is typically higher than 3dB DC. Simulations reveal that the excess loss of a directional coupler is negligible ($< 0.1\ dB$) in compared to 50:50 MMI (<1dB).

Fig. 4.8 and Fig. 4.9 provide the predicted wavelength dependence splitting ratio for a 3dB DC and a MMI coupler respectively. The relative phase of the lowest order symmetric and antisymmetric mode of the dual waveguide is linear in frequency for a constant effective index difference between the two modes. However, waveguide and, to a lesser extent, material dispersion add to this linear term. The slope of the DC splitting ratio variation, although modest, is significantly greater than if there was no waveguide dispersion. Note that adjusting the lengths of the DC arm and the path imbalance between them, the wavelength dependency of the splitting

ratio of a MZI sub-circuit created by a pair of DC interconnected with a pair of waveguide arms [93]. This expedient would double the complexity of the couplers, inviting risk, but the inclusion of maximally flat coupler test-structures would enable evaluation of their potential to provide loss-loss and broadband operation. Figure 4.10 illustrates the optical intensity profile for 3dB MMI couplers based on the optimum parameters presented in Table 4.1.

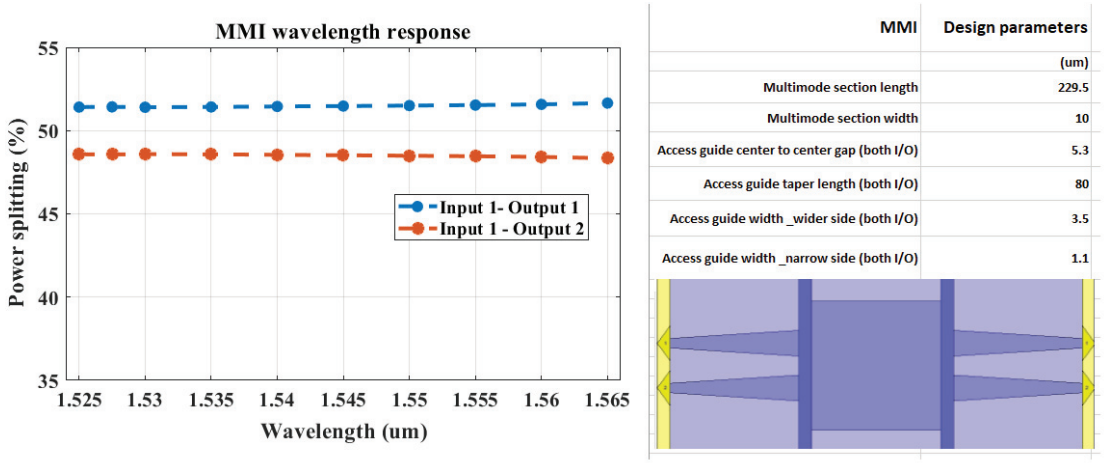

Figure 4.9 Splitting ratio of the straight section of a 3dB MMI versus wavelength.

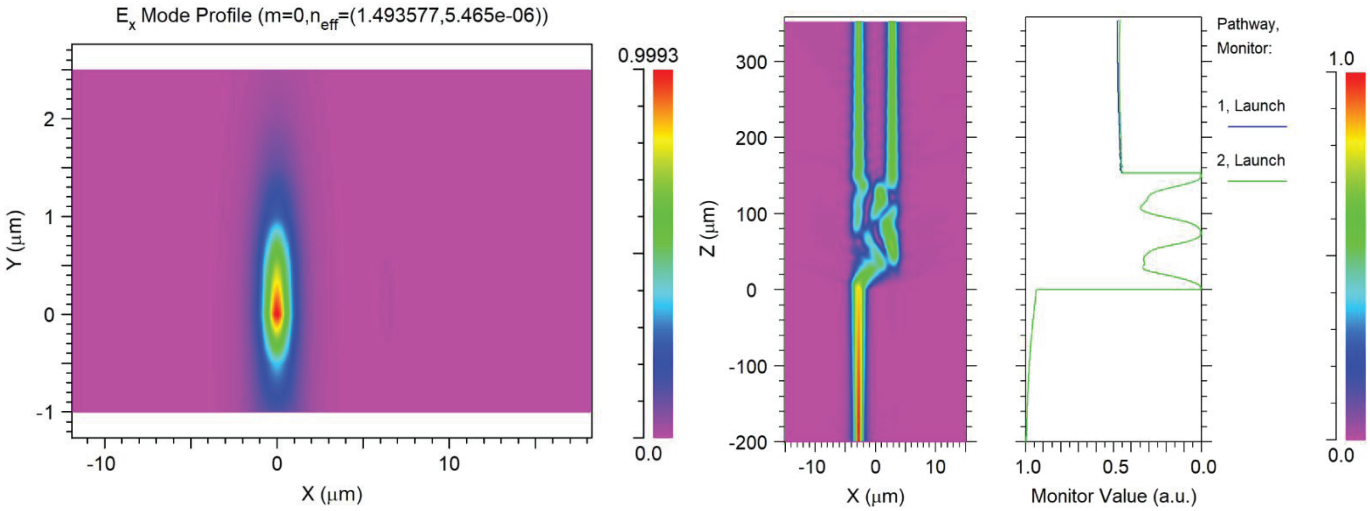

Figure 4.10 Optical intensity profile for MMI couplers.

Table 4.2: Optimum design specifications for 3dB MMI couplers

Parameters	Value
Wavelength (µm)	1.5475
MMI length (µm)	230.50
MMI width (µm)	10.05
I/O port separation (µm)	3
I/O arm length (µm)	200
Taper width (µm)	3.5
Effective refractive index	1.49356

The main effect of vacuum wavelength offset from the design wavelength over the operating band for an MMI is defocus of the field at its output ports. This impacts directly on the excess loss but has little impact on the splitting ratio. The results of the simulation shown in Fig. 4.9 confirm that the splitting ratio of an MMI is substantially constant over the entire C-band and the splitting ratio error is substantially smaller than the band-edge error of a DC. Given that simulations suggest that a spectrometer using either type of coupler is viable as a demonstrator it is prudent to use experimental trials of test structure to better inform a decision on which to use further or to fabricate spectrometer prototypes making use of one, the other, or a mixture of both.

4.7 Simulation Results

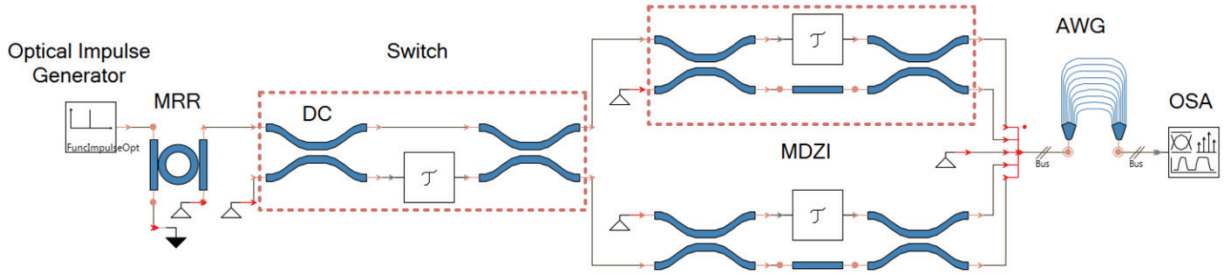

Figure 4.11 VPI schematic of a circuit architecture.

Fig. 4.11 shows a VPI schematic of the spectrometer architecture illustrated in Fig. 4.1 stripped of the RR and with waveguide delay-lines and frequency independent static phase shift elements denoted by the symbol τ. The phase shifts are manually modified to bias and switch between the higher and lower MZI stages. Power splitting ratio for a nominally 3dB directional coupler with 0dBm input power supply. Figure 4.13 represents the complete simulation of the spectrometer circuit including the scanning results of upper MZDI and lower MZDI.

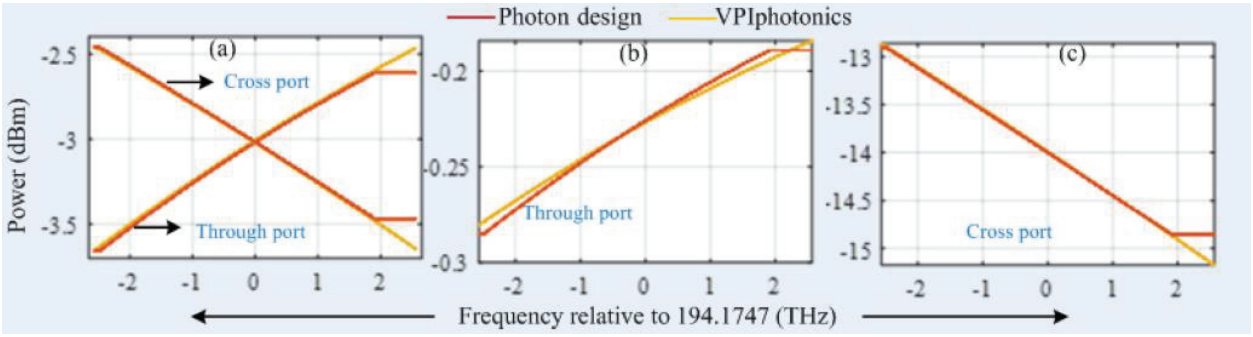

Figure 4:12 Power splitting of a 3 dB directional coupler with 0 dBm input power [93].

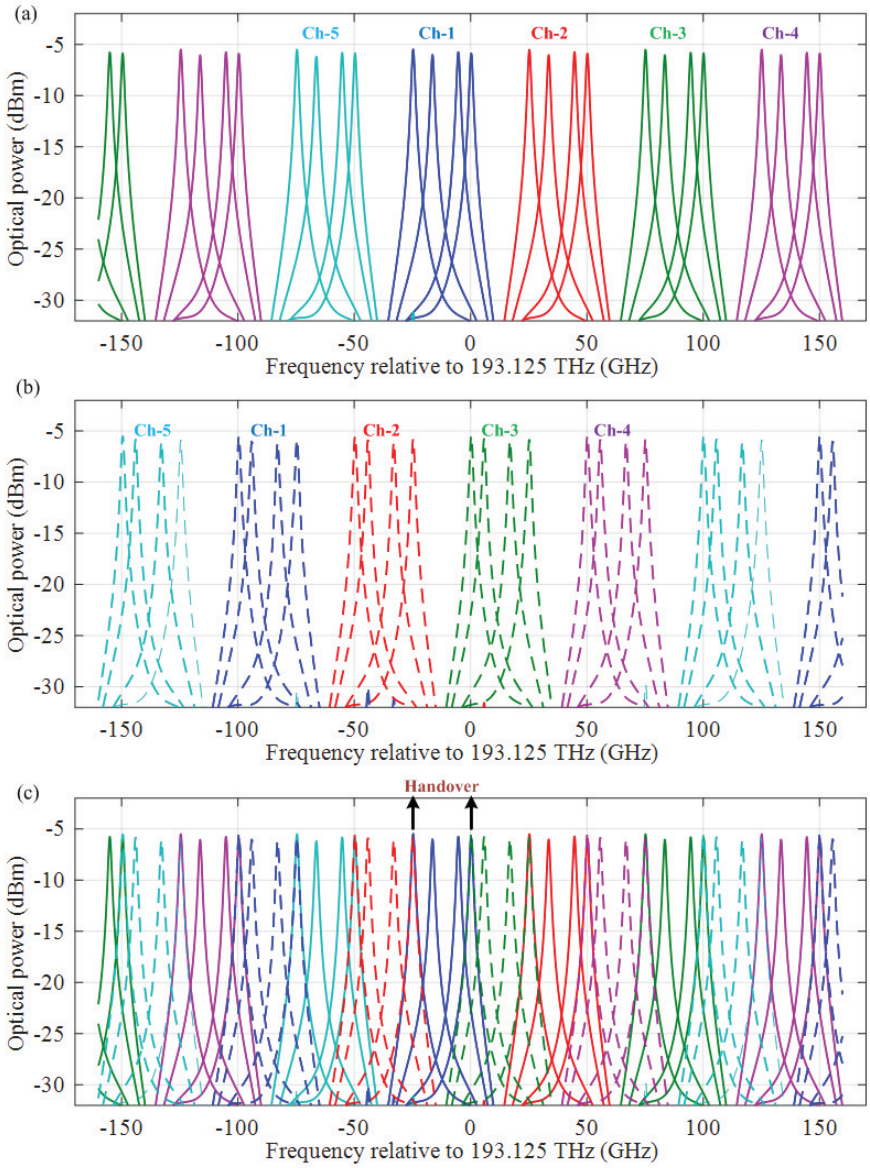

Figure 4.12 A complete simulation of the spectrometer circuit. (a) Upper MZDI selected phase of scanning cycle; (b) lower MZDI selected phase of scanning cycle; (c) full scanning cycle.

4.8 Layout

Layout is developed based on LioniX International foundry provided Process Design Kit that contains building blocks and information about their process, material platform technologies, special design rules. LioniX PDK supports Synopsys PhoeniX OptoDesigner, which means the final designs need to be layout with OptoDesigner and simulated before generating GDSII files.

OptoDesigner is the industry standard photonic integrated circuit design tool providing native all-angle and all-shape layout design using complete parametrized photonic libraries. It allows designers to automatically translate design intent into manufacturable layout thanks to the photonic

verification and design rule checking functionalities implemented both on the technology and functional level. Together with OptSim Circuit, Synopsys OptoDesigner offers full end-to-end photonic design tools allowing designers for first-time right tapeout. OptoDesigner uses a script language. This language gives maximum flexibility to the designer to create full parametric design. Scripts are used to define the structure, to start simulations, or to perform mask layout generation; this powerful feature is therefore built-in all modules allowing unlimited combinations.

OptSim Circuit is a photonic circuit simulation tool that enables PIC time and frequency domain analysis. The implementation of a PDK in OptSim Circuit consists in composite components called compound components, which are made of library blocks with parameters and data files already preset to model a given photonic device or component. In addition, the interface with the layout tool OptoDesigner enables the user to design a circuit intent in OptSim Circuit and then open it in OptoDesigner to finalize the physical realization in terms of component placement and waveguide routing. The circuit can then be saved and opened back in OptSim Circuit to simulate the PIC, including the effect of routing and crosstalk.

4.8.1 Die Templates

All individual function parts, including test structures, as MZI, direction couplers, micro-rings, AWG, and final whole structure are placed carefully put into either $16 \times 16\, mm^2$, or $32 \times 8\, mm^2$. For ease of simplicity, we used 16 ×16 die size in order to accommodate all the photonics components. The 100 mm diameter silicon wafer is divided into a matrix of 4 x 4 blocks of 16 mm x 16 mm, as indicated in Figure 4.14. In each block, a Process Control Feature is added to control the dimensions of the waveguides.

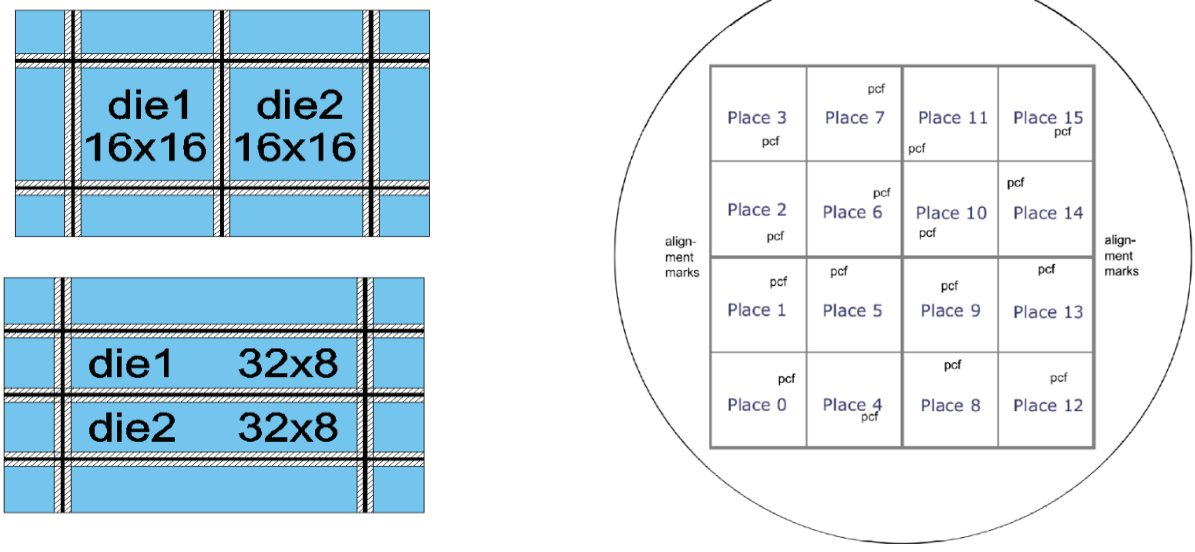

Figure 4.14 Wafer map showing the place of the blocks on the wafer; outside the blocks alignment marks is added. Inside each block, a process control features set (pcf) is placed on a suitable place.

Die template for a die of 16 mm × 16 mm, suitable for standard packaging on a PCB or for manual placement of probe pens as shown in figure 4.15. This die template is also suitable for integration with the laser building block. The fiber array is on the left, and the connection to the laser is on the bottom right. If the laser building block is not used, there can be two fiber arrays (left, right). There can be two DC pad arrays (top, bottom). Here, adapter type “pC” has been selected for both bondpad arrays, which has 20 bondpads.

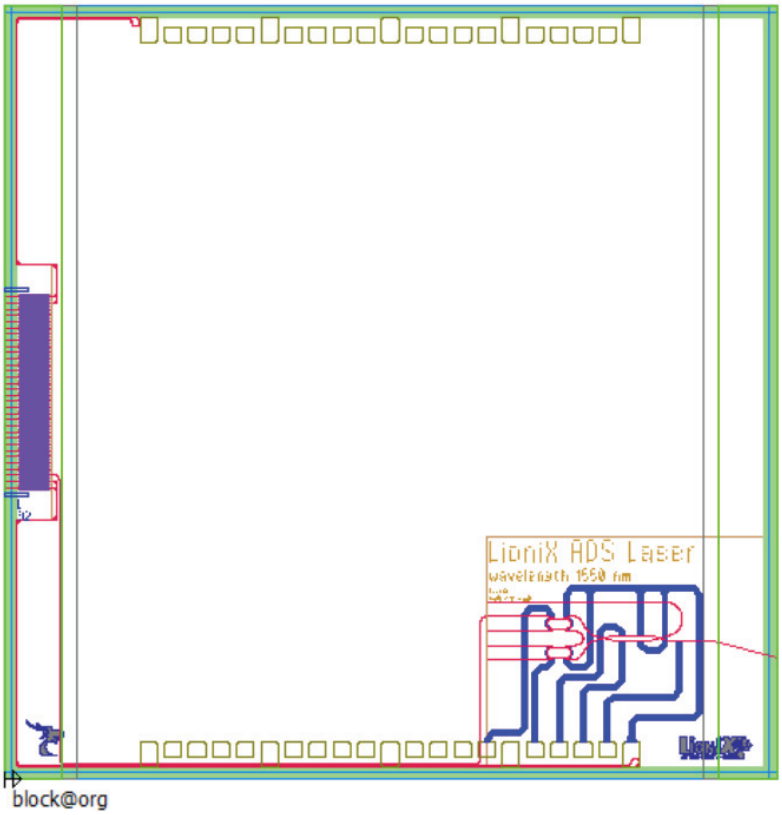

Figure: 4.15 16 mm × 16 mm die template.

4.8.2 Mask cross-sections

A cross-section is a slice of a waveguide or other device on our circuit - it shows the materials and the geometric shape of the device, in our situations it is called “double-stripe”, TriPleX BB presented in figure 4.16. OptoDesigner uses the concept of mask cross-sections to relate the cross-section of a device to information about the fabrication process. The waveguide with desired cross-section generated from PDK also would be checked by plotting mode profiles and effective index for straight and cured waveguides. The mask cross-section can be considered as the logical layer under which several representations of physical cross-section (mask layers) can reside.

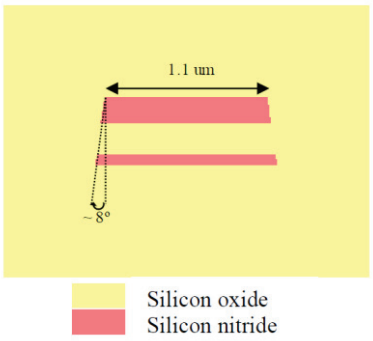

Figure 4.16 Cross-Section of the LioniX TriPleX ADS waveguide with a Si3N4 core and SiO2 cladding.

4.8.3 Design Rule Checks (DRC)

OptoDesigner has two sets of Design Rule Checking on a mask layout before GDSII filing. A photonic DRC checks for issues in functionality. For example, a check if the radius of curvature is high enough to guide the light is a photonic DRC. A fabrication DRC checks if the design can be fabricated without problems. LioniX PDK provides two sets of DRC in addition to "Design rules for packaging" if fabrication is followed by dicing, polishing, alignment and packing.

1. Minimum waveguide width: 1.0 µm;
2. Minimum radius of curvature: 80 µm (negligible bend loss for TE only);
3. Minimum gap between optical waveguides: 1.0 µm.
4. Heater width: 20 µm; Lead width: 100 µm.
5. Minimum gap between electrical parts: 30.0 µm;
6. Multiple heaters may be connected to the same ground pad.
7. Minimum pitch between a heater and adjacent waveguide: 250 µm (thermal crosstalk:-17 dB).

However, the script for the complete circuit design layout fitting with the given template is listed in Appendix II.

4.9 LioniX ADS PDK Modeling

4.9.1 Waveguides

The waveguides are modeled with full effective index calculated for TE mode and 1.1 um width from 1.53 to 1.565 um with the following transfer function:

$$H(\lambda) = I_L e^{jn_{eff}(\lambda)\frac{2\pi}{\lambda_0}L}$$

where I_L insertion loss, $n_{eff}(\lambda)$ effective index as function of wavelength, λ_0 wavelength in vacuum, L waveguide length.

Loss and phase effects are accounted for, so the model can be used to simulate, for instance, an interference in Mach-Zehnder interferometer configurations, resulting in filtering behavior. Only one waveguide width value of 1.1 um is modeled for TE mode, and the effect of curvature on the effective index is neglected.

4.9.2 Phase Modulators

The phase modulators propagation properties are the same as the waveguide blocks. The phase modulation is modeled based on the following transfer function.

$$H = 10^{\frac{simLoss\ L}{10}} e^{j\pi \frac{simDeltaTemp}{simPiTemp}}$$

where $simLoss$ loss [dB/cm], L length, $simDeltaTemp$ device modulating temperature $simPiTemp$ temperature needed for π rad phase shift.

4.9.3 Heater Lead

The heater lead propagation properties are the same as the waveguide blocks. The phase modulation is modeled with the following transfer function.

$$H = 10^{\frac{simLoss\ L}{10}} e^{j\pi \frac{(P_{in}+power\_bias\_mW)}{Ppi\_mW}}$$

where $simLoss$ loss [dB/cm], L length, P_{in} input power [mW], Ppi_mW power needed for π rad phase shift [mW], $power\_bias\_mW$ power bias added to input power [mW].

4.9.4 Splitters and Couplers

The splitter and directional couplers are ideal components that distribute the input signals into output ports with a given insertion loss in dB. The splitter doesn't introduce any phase rotation, while the coupler introduces a $\pi/2$ shift for the cross terms, and no phase shift for the bar terms.

We placed the asymmetric MZI building block in the die template and add the optical and electrical connectors in OptoDesigner to finish the design as presented in figure 4.17. The final layout will then include the building block inside the LioniX ADS template is depicted in figure 4.18, whereas a complete layout containing of multiple components is illustrated in figure 4.19.

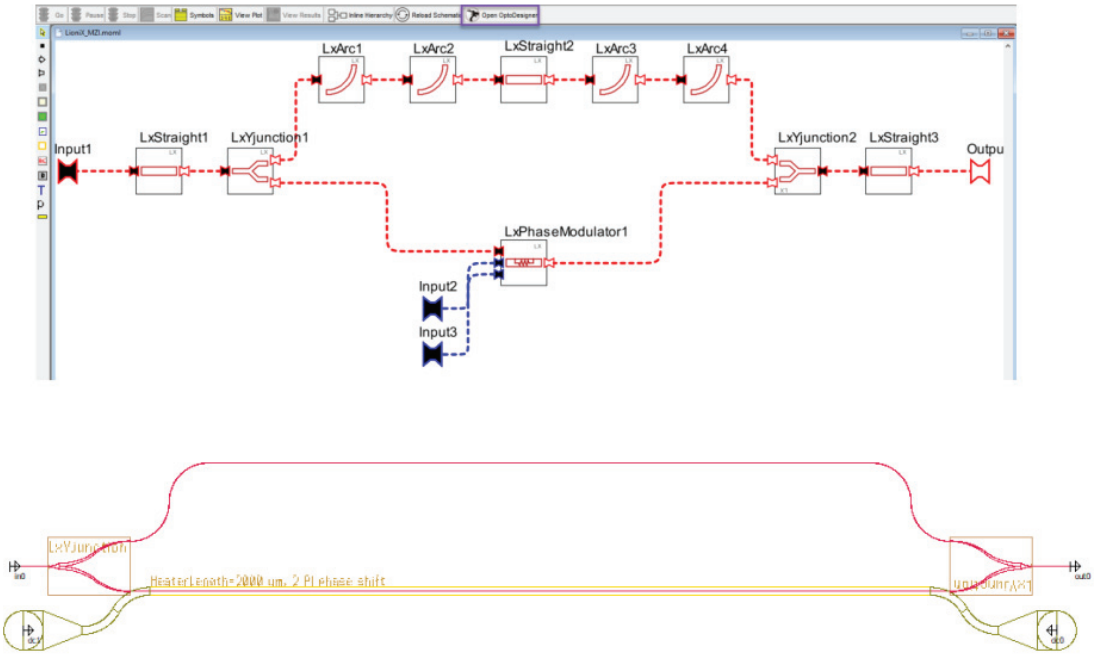

Figure 4.17 Fitting the PIC layout into die template.

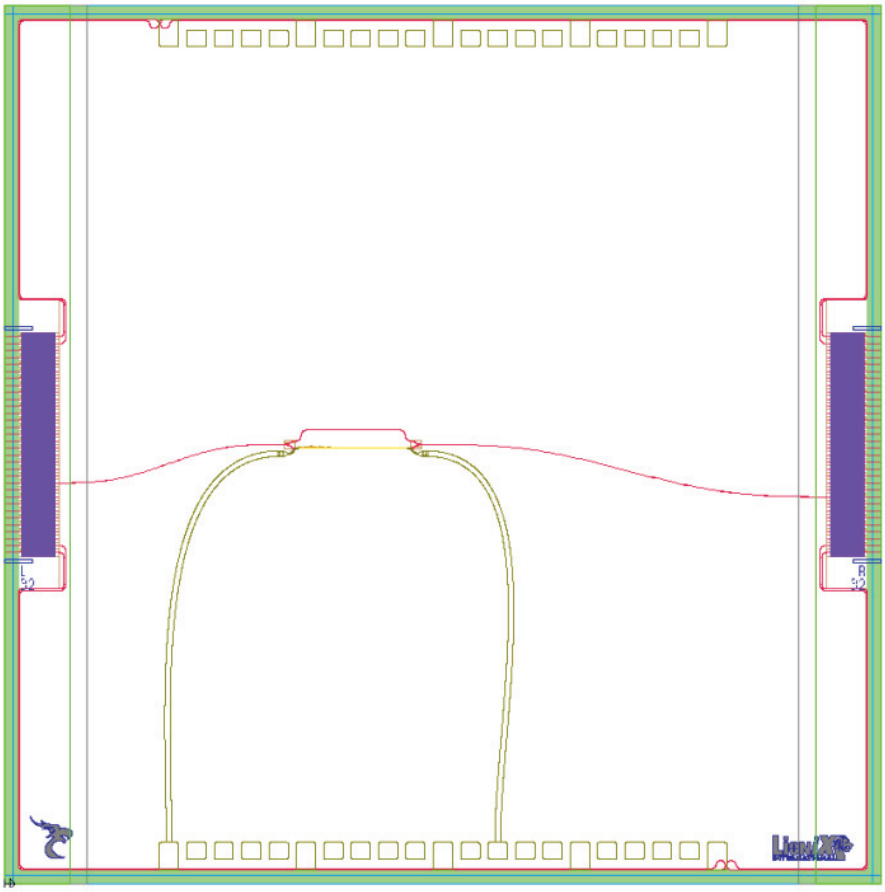

Figure 4.18 A complete layout for a single component.

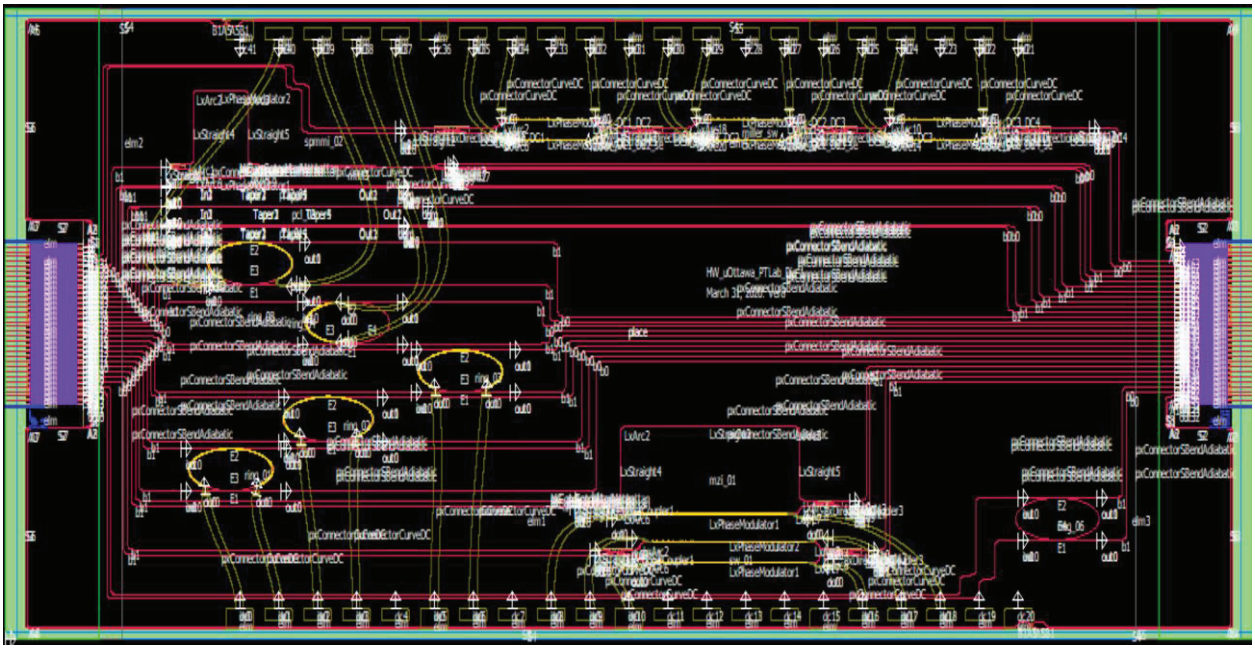

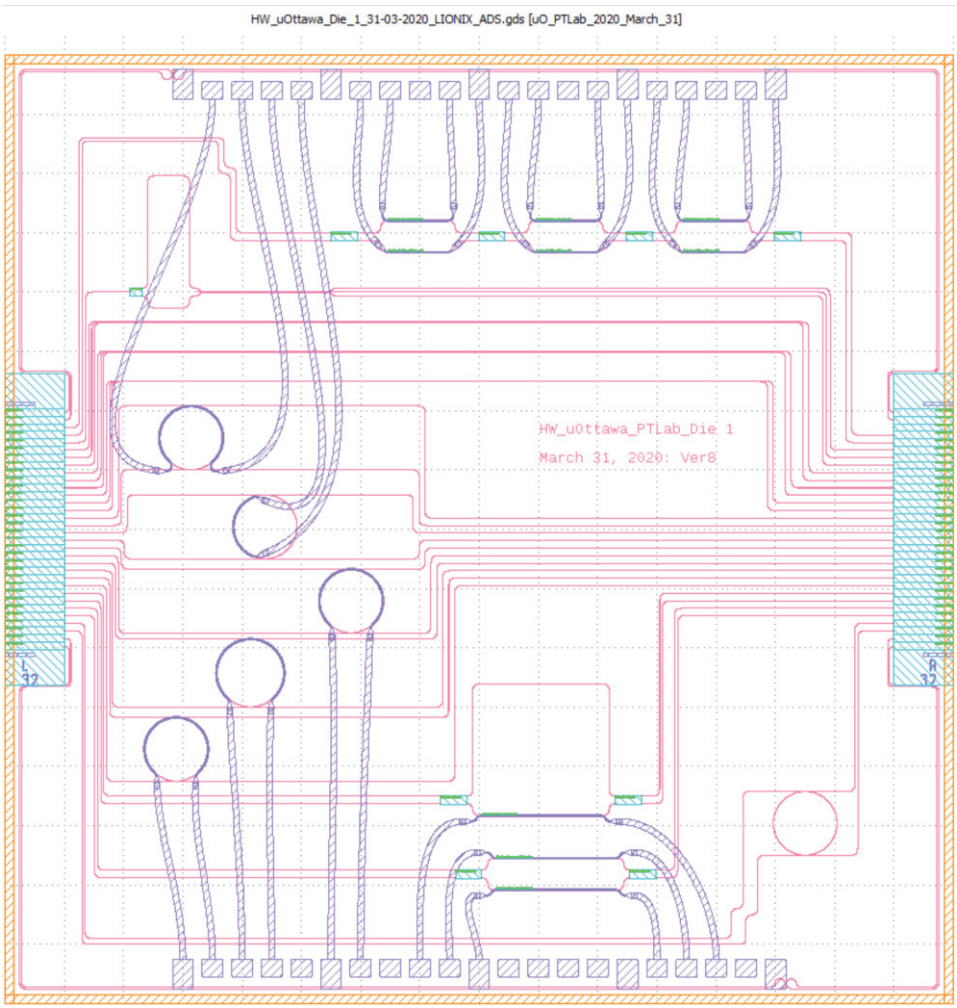

Figure 4.19 A complete GDSII layout.

4.10 Summary

The design architecture of a compact on-chip high-resolution C-band panoramic spectrometer is presented and verified by software simulation using an industry standard tool particularly focused on MMI coupler, MZDI, 3 dB directional couplers components. The components simulations that supported the assessment of the feasibility of a spectrometer compliant with the specification made use of the LioniX asymmetric double strip (ADS) waveguide and the low-cost photolithography has a minimum feature size of 1 μm. A spot size convertor that efficiently couples light from standard single mode fibre to the ADS waveguide is available as a library component in the LioniX process development kit (PDK). Access to the PDK, has enables the update of the materials database used in simulations with the precise optical properties of the materials used in the LioniX process including the dispersion of the refractive index across the C-band.

CHAPTER 5

Conclusions

5.1 Summary & Conclusions

Microwave photonic applications in the terahertz (THz) region of the spectrum are attracting increasing attention for next-generation (5G/6G) wireless communication systems that is capable of handling tremendous data rates. An electro-optic modulator (EOM) is a key enabling technology as it enables the transference of information from the electrical domain of wireless communications to the optical domain. The picosecond class wavelength tuning speeds on sub 100 GHz dense wavelength division multiplexing grids and ultra low loss of the fully integrated EOM system is the paramount importance in applications such as optical & wireless communications i.e. the generation of mm waves for 5G wireless and research into sources of THz radiation, high speed digital electronics, radar, lidar, and astronomy. The application of mm-wave is not limited to wireless access networks only. Antenna remoting, phased-array antennas, optical sensors, radars and tera-hertz applications can also benefit from efficient generation and transmission of mmwaves. The heterogeneous approach of utilizing SN on LN waveguide compact EO modulator has anticipated best optical modulation performance that allows multiple opportunities for universal linear optical networks, chip-scale microwave photonics systems, optical switching, etc. A coherent electro-optic photonic integrated circuit deploying generalized Mach-Zehnder interferometer is necessary to drive the phase modulators. On the other hand, the ability to configure network functions, protocols, and make optimal use of spectrum is made possible by monitoring the state of the optical network.

This thesis offers some insight in the context of coherent optical signal processor architecture through the design and verification by simulation which applicable ranging from RF photonics to optical communications. Chapter 2 presents a coherent electro-optic photonic integrated circuit deploying generalized Mach-Zehnder interferometer (GMZI) substituting $N\times1$ combiner by an optical $N\times N$ discrete Fourier transform (DFT) in order to generate a regularly spaced frequency comb to drive the phase modulators. A generalized transfer matrix approach is applied to model the envisioned framework which is examined by simulations performed using an industry standard software tool. Provisioning of N spatially separated phase correlated subcarriers for all OFDM technique offers terabit data demands through providing multi-carriers for augmented transmission in the context of microwave photonic applications. With the added benefits of circuit symmetries and tight optical path length control, the proposed architecture has the potential to eliminate the presence of optical de-multiplexing filter at the output of an optical comb generator and can be easily integrated in any material platform that exhibits linear EO phase modulation effect. The proposed architecture is demonstrated for both even and odd dimensions of MMI configurations which has no restriction on the number of inputs. The proposed circuit architecture can be used for frequency up-conversion/down-conversion, SSB modulation, and frequency multiplication based on the choice of output ports and dimension of the circuit.

The heterogeneous approach of utilizing lithium niobate (LN) and silicon nitride (SN) waveguide integrated on a single chip electro optic modulator that has anticipated best optical modulation performance is presented in chapter 3. Lithium niobate (LN) is widely used for guided-wave optical devices and high performance photonic integrated functionalities. However, bulk LN modulators suffer from large optical mode size with weak confinement, and large bending radii because of low refractive index contrast. In contrary, the importance of silicon nitride (Si3N4) thin-films have been rapidly increased due to a small thermo-optic coefficient, ultralow propagation loss high-power handling capability, low second-order nonlinearity, and photonic integrated circuit compatibility. The main issue of the current LN phase shifter is its poor modulation efficiency due to the relatively small Pockels coefficient. The greatest promise of a breakthrough lies with hybrid material systems that combine the excellent properties of active materials (e.g. thin films on Si3N4) for high speed functions and LN for drift free bias functions while leveraging the powerful, scalable fabrication processes associated with Si3N4. The hybrid SN-LN modulator platform was the subject of this chapter research, which included recent breakthroughs in the field as well as design and production considerations. Layer thicknesses for a single platform optimized for best performance across the whole telecommunication wavelength range are also addressed, as well as a sampling of future hybrid technologies at visible and mid-infrared wavelengths. Recent advancements in EO modulators lead to an exciting future of novel device designs and applications.

In chapter 4, the design architecture of compact on-chip high-resolution wideband spectrometer such as Mach-Zehnder delay interferometers (MZDI), 3dB multimode interference (MMI) couplers and 2×2 50:50 directional couplers and are presented and validated by software simulations. This chapter describes the architecture for compact on-chip spectrometry targeting high resolution across the entire C-band to measure the spectral profile of WDM signals reliably and accurately. The proposed architecture consists of three stages. The circuit is composed of a scanning ring resonator followed by a parallel arrangement of arrayed waveguide grating (AWGs) with interlaced channel spectra. The MZDI stage enables alignment of the RR resonances with the MZDI-AWG channels as the comb is scanned over a free-spectral range (FSR). A merit of this architecture is that it requires a minimum number of thermo-optic phase-shift elements for setting bias points and for tuning which minimizes power consumption of a demonstrator. The components simulations that supported the assessment of the feasibility of a spectrometer compliant with the specification made use of the LioniX asymmetric double strip (ADS) waveguide. A spot size convertor that efficiently couples light from standard single mode fibre to the ADS waveguide is available as a library component in the LioniX process development kit (PDK). Access to the PDK, has enables the update of the materials database used in simulations with the precise optical properties of the materials used in the LioniX process including the dispersion of the refractive index across the C-band.

In summary, the thesis contributes to the advancement of the field through the conception, theoretical modelling, verification by simulation, and experimental demonstration of original photonic processor circuit architectures amenable to photonic integration that include:

- A generalized coherent electro-optic circuit design approach that generates a frequency comb of *N* separated harmonically subcarriers for the applications inter alia to phase correlated sub-carrier generation for Tbit/s data transfer using optical orthogonal frequency division multiplexing.
- Advancement of the integrated electro optical modulators (>300 gigabauds), through innovative architectures targeting key requirements of picosecond (ps) class wavelength tuning speeds on sub 100 GHz dense wavelength division multiplexing grids, ultra-low loss (one tenth dB per cm), and ultra-power-efficient (femtojoules) all-photonic processing.
- A design architecture of a compact on-chip high-resolution commercially viable C-band panoramic spectrometer.

5.2 Future Scope

The thesis concentrates on electro-optic photonic integrated circuits which can offers a wide range of functionalities. Realization of these circuits in their integrated formats while considering practical issues with design and material platform is the next step. Some suggestions for future work are offered below.

- The universal RF photonic processor introduced up to initially the dimension N = 8 and then beyond.
- The robust design of taper in the waveguide geometry to develop high confinements and low propagation losses EO modulator.
- Developing a higher order optical switching matrix (e.g., 128x128) incorporating 2x2 MZI switch along with a high-voltage CMOS driving circuitry and necessary switching algorithms.
- On-chip sensors, controllers, and algorithms to monitor the state of the system.
- The operation of RF drive sources, the length of the waveguides connecting the drive signal to the phase modulators and the long-term stability issues particularly dc bias drift.
- Research on circuit symmetries and emerging trimming algorithms to approach perfect photonic systems using imperfect components.

Appendix I. MMI DFT Equivalence

Even Dimensions

For $p = 1$ and q *even*, the elements of the transmission matrix T_{MMI} of a standard uniform split ratio MMI coupler are:

$$\{T_{MMI}\}_{\nu\mu} = \frac{1}{\sqrt{q}} e^{-i\gamma} \begin{cases} \exp\left[i\left(\frac{\nu-\mu}{2}\right)^2 \frac{\pi}{q}\right] & (\nu-\mu)\ even \\ -\exp\left[i\left(\frac{(\nu+\mu+1)}{2}\right)^2 \frac{\pi}{q}\right] & (\nu-\mu)\ odd \end{cases} \quad ; \quad \nu, \mu = 0,1,..,(q-1)$$

Set:

$$\{\Gamma\}_{\nu\nu} = \begin{cases} \exp\left[-i\left(\frac{\nu}{2}\right)^2 \frac{\pi}{q}\right] & \nu\ even \\ -\exp\left[-i\left(\frac{(\nu+1)}{2}\right)^2 \frac{\pi}{q}\right] & \nu\ odd \end{cases} \quad ; \quad \{\Gamma\}_{\mu\mu} = \begin{cases} \exp\left[-i\left(\frac{\mu}{2}\right)^2 \frac{\pi}{q}\right] & \mu\ even \\ -\exp\left[-i\left(\frac{(\mu+1)}{2}\right)^2 \frac{\pi}{q}\right] & \mu\ odd \end{cases}$$

De-phase:

$$\{\Gamma T_{MMI}\Gamma\}_{\nu\mu}$$
$$= \frac{1}{\sqrt{q}} \begin{cases} \exp\left[-i\left(\frac{\nu}{2}\right)^2 \frac{\pi}{q}\right] \exp\left[i\left(\frac{\nu-\mu}{2}\right)^2 \frac{\pi}{q}\right] \exp\left[-i\left(\frac{\mu}{2}\right)^2 \frac{\pi}{q}\right] & \nu\ even \quad \mu\ even \\ \exp\left[-i\left(\frac{\nu}{2}\right)^2 \frac{\pi}{q}\right] \exp\left[i\left(\frac{(\nu+\mu+1)}{2}\right)^2 \frac{\pi}{q}\right] \exp\left[-i\left(\frac{(\mu+1)}{2}\right)^2 \frac{\pi}{q}\right] & \nu\ even \quad \mu\ odd \\ \exp\left[-i\left(\frac{(\nu+1)}{2}\right)^2 \frac{\pi}{q}\right] \exp\left[i\left(\frac{(\nu+\mu+1)}{2}\right)^2 \frac{\pi}{q}\right] \exp\left[-i\left(\frac{\mu}{2}\right)^2 \frac{\pi}{q}\right] & \nu\ odd \quad \mu\ even \\ \exp\left[-i\left(\frac{(\nu+1)}{2}\right)^2 \frac{\pi}{q}\right] \exp\left[i\left(\frac{\nu-\mu}{2}\right)^2 \frac{\pi}{q}\right] \exp\left[-i\left(\frac{(\mu+1)}{2}\right)^2 \frac{\pi}{q}\right] & \nu\ odd \quad \mu\ odd \end{cases}$$

Simplify:

$$\{\Gamma T_{MMI}\Gamma\}_{\nu\mu} = \frac{1}{\sqrt{q}} \begin{cases} \exp\left[-i\frac{\nu\mu}{4}\frac{2\pi}{q}\right] & \nu\ even \quad \mu\ even \\ \exp\left[i\frac{\nu(\mu+1)}{4}\frac{2\pi}{q}\right] & \nu\ even \quad \mu\ odd \\ \exp\left[i\frac{(\nu+1)\mu}{4}\frac{2\pi}{q}\right] & \nu\ odd \quad \mu\ even \\ \exp\left[-i\frac{(\nu+1)(\mu+1)}{4}\frac{2\pi}{q}\right] & \nu\ odd \quad \mu\ odd \end{cases}$$

Set:

$$z = \exp\left[-i\frac{2\pi}{q}\right]$$

Consequently, the matrix of powers of z that compose the de-phased transmission matrix is:

$$\begin{bmatrix}
0 & 0 & 0 & 0 & 0 & 0 & 0 & 0 & 0 & 0 & 0 & 0 & 0 & 0 & 0 & 0 \\
0 & -1 & 1 & -2 & 2 & -3 & 3 & -4 & 4 & -5 & 5 & -6 & 6 & -7 & 7 & -8 \\
0 & 1 & -1 & 2 & -2 & 3 & -3 & 4 & -4 & 5 & -5 & 6 & -6 & 7 & -7 & 8 \\
0 & -2 & 2 & -4 & 4 & -6 & 6 & -8 & 8 & -10 & 10 & -12 & 12 & -14 & 14 & -16 \\
0 & 2 & -2 & 4 & -4 & 6 & -6 & 8 & -8 & 10 & -10 & 12 & -12 & 14 & -14 & 16 \\
0 & -3 & 3 & -6 & 6 & -9 & 9 & -12 & 12 & -15 & 15 & -18 & 18 & -21 & 21 & -24 \\
0 & 3 & -3 & 6 & -6 & 9 & -9 & 12 & -12 & 15 & -15 & 18 & -18 & 21 & -21 & 24 \\
0 & -4 & 4 & -8 & 8 & -12 & 12 & -16 & 16 & -20 & 20 & -24 & 24 & -28 & 28 & -32 \\
0 & 4 & -4 & 8 & -8 & 12 & -12 & 16 & -16 & 20 & -20 & 24 & -24 & 28 & -28 & 32 \\
0 & -5 & 5 & -10 & 10 & -15 & 15 & -20 & 20 & -25 & 25 & -30 & 30 & -35 & 35 & -40 \\
0 & 5 & -5 & 10 & -10 & 15 & -15 & 20 & -20 & 25 & -25 & 30 & -30 & 35 & -35 & 40 \\
0 & -6 & 6 & -12 & 12 & -18 & 18 & -24 & 24 & -30 & 30 & -36 & 36 & -42 & 42 & -48 \\
0 & 6 & -6 & 12 & -12 & 18 & -18 & 24 & -24 & 30 & -30 & 36 & -36 & 42 & -42 & 48 \\
0 & -7 & 7 & -14 & 14 & -21 & 21 & -28 & 28 & -35 & 35 & -42 & 42 & -49 & 49 & -56 \\
0 & 7 & -7 & 14 & -14 & 21 & -21 & 28 & -28 & 35 & -35 & 42 & -42 & 49 & -49 & 56 \\
0 & -8 & 8 & -16 & 16 & -24 & 24 & -32 & 32 & -40 & 40 & -48 & 48 & -56 & 56 & -64
\end{bmatrix}$$

Special cases:

Equivalence $mod\ \boldsymbol{q = 8}$**:**

$$\begin{bmatrix}
0 & 0 & 0 & 0 & 0 & 0 & 0 & 0 \\
0 & -1 & 1 & -2 & 2 & -3 & 3 & -4 \\
0 & 1 & -1 & 2 & -2 & 3 & -3 & 4 \\
0 & -2 & 2 & -4 & 4 & -6 & 6 & -8 \\
0 & 2 & -2 & 4 & -4 & 6 & -6 & 8 \\
0 & -3 & 3 & -6 & 6 & -9 & 9 & -12 \\
0 & 3 & -3 & 6 & -6 & 9 & -9 & 12 \\
0 & -4 & 4 & -8 & 8 & -12 & 12 & -16
\end{bmatrix} \equiv \begin{bmatrix}
0 & 0 & 0 & 0 & 0 & 0 & 0 & 0 \\
0 & 7 & 1 & 6 & 2 & 5 & 3 & 4 \\
0 & 1 & 7 & 2 & 6 & 3 & 5 & 4 \\
0 & 6 & 2 & 4 & 4 & 2 & 6 & 0 \\
0 & 2 & 6 & 4 & 4 & 6 & 2 & 0 \\
0 & 5 & 3 & 2 & 6 & 7 & 1 & 4 \\
0 & 3 & 5 & 6 & 2 & 1 & 7 & 4 \\
0 & 4 & 4 & 0 & 0 & 4 & 4 & 0
\end{bmatrix} \Rightarrow \Gamma T_{MMI} \Gamma = \frac{1}{\sqrt{8}} \begin{bmatrix}
z^0 & z^0 & z^0 & z^0 & z^0 & z^0 & z^0 & z^0 \\
z^0 & z^7 & z^1 & z^6 & z^2 & z^5 & z^3 & z^4 \\
z^0 & z^1 & z^7 & z^2 & z^6 & z^3 & z^5 & z^4 \\
z^0 & z^6 & z^2 & z^4 & z^4 & z^2 & z^6 & z^0 \\
z^0 & z^2 & z^6 & z^4 & z^4 & z^6 & z^2 & z^0 \\
z^0 & z^5 & z^3 & z^2 & z^6 & z^7 & z^1 & z^4 \\
z^0 & z^3 & z^5 & z^6 & z^2 & z^1 & z^7 & z^4 \\
z^0 & z^4 & z^4 & z^0 & z^0 & z^4 & z^4 & z^0
\end{bmatrix}$$

Reorder columns then rows:

$$\begin{bmatrix}
z^0 & z^0 & z^0 & z^0 & z^0 & z^0 & z^0 & z^0 \\
z^0 & z^7 & z^1 & z^6 & z^2 & z^5 & z^3 & z^4 \\
z^0 & z^1 & z^7 & z^2 & z^6 & z^3 & z^5 & z^4 \\
z^0 & z^6 & z^2 & z^4 & z^4 & z^2 & z^6 & z^0 \\
z^0 & z^2 & z^6 & z^4 & z^4 & z^6 & z^2 & z^0 \\
z^0 & z^5 & z^3 & z^2 & z^6 & z^7 & z^1 & z^4 \\
z^0 & z^3 & z^5 & z^6 & z^2 & z^1 & z^7 & z^4 \\
z^0 & z^4 & z^4 & z^0 & z^0 & z^4 & z^4 & z^0
\end{bmatrix} \rightarrow \begin{bmatrix}
z^0 & z^0 & z^0 & z^0 & z^0 & z^0 & z^0 & z^0 \\
z^0 & z^1 & z^2 & z^3 & z^4 & z^5 & z^6 & z^7 \\
z^0 & z^7 & z^6 & z^5 & z^4 & z^3 & z^2 & z^1 \\
z^0 & z^2 & z^4 & z^6 & z^0 & z^2 & z^4 & z^6 \\
z^0 & z^6 & z^4 & z^2 & z^0 & z^6 & z^4 & z^2 \\
z^0 & z^3 & z^6 & z^1 & z^4 & z^7 & z^2 & z^5 \\
z^0 & z^5 & z^2 & z^7 & z^4 & z^1 & z^6 & z^3 \\
z^0 & z^4 & z^0 & z^4 & z^0 & z^4 & z^0 & z^4
\end{bmatrix}$$

$$\rightarrow \begin{bmatrix}
z^0 & z^0 & z^0 & z^0 & z^0 & z^0 & z^0 & z^0 \\
z^0 & z^1 & z^2 & z^3 & z^4 & z^5 & z^6 & z^7 \\
z^0 & z^2 & z^4 & z^6 & z^0 & z^2 & z^4 & z^6 \\
z^0 & z^3 & z^6 & z^1 & z^4 & z^7 & z^2 & z^5 \\
z^0 & z^4 & z^0 & z^4 & z^0 & z^4 & z^0 & z^4 \\
z^0 & z^5 & z^2 & z^7 & z^4 & z^1 & z^6 & z^3 \\
z^0 & z^6 & z^4 & z^2 & z^0 & z^6 & z^4 & z^2 \\
z^0 & z^7 & z^6 & z^5 & z^4 & z^3 & z^2 & z^1
\end{bmatrix}$$

Unwrap powers:

$$\begin{bmatrix} z^0 & z^0 & z^0 & z^0 & z^0 & z^0 & z^0 & z^0 \\ z^0 & z^1 & z^2 & z^3 & z^4 & z^5 & z^6 & z^7 \\ z^0 & z^2 & z^4 & z^6 & z^0 & z^2 & z^4 & z^6 \\ z^0 & z^3 & z^6 & z^1 & z^4 & z^7 & z^2 & z^5 \\ z^0 & z^4 & z^0 & z^4 & z^0 & z^4 & z^0 & z^4 \\ z^0 & z^5 & z^2 & z^7 & z^4 & z^1 & z^6 & z^3 \\ z^0 & z^6 & z^4 & z^2 & z^0 & z^6 & z^4 & z^2 \\ z^0 & z^7 & z^6 & z^5 & z^4 & z^3 & z^2 & z^1 \end{bmatrix} \equiv \begin{bmatrix} z^0 & z^0 & z^0 & z^0 & z^0 & z^0 & z^0 & z^0 \\ z^0 & z^1 & z^2 & z^3 & z^4 & z^5 & z^6 & z^7 \\ z^0 & z^2 & z^4 & z^6 & z^8 & z^{10} & z^{12} & z^{14} \\ z^0 & z^3 & z^6 & z^9 & z^{12} & z^{15} & z^{18} & z^{21} \\ z^0 & z^4 & z^8 & z^{12} & z^{16} & z^{20} & z^{24} & z^{28} \\ z^0 & z^5 & z^{10} & z^{15} & z^{20} & z^{25} & z^{30} & z^{35} \\ z^0 & z^6 & z^{12} & z^{18} & z^{24} & z^{30} & z^{36} & z^{42} \\ z^0 & z^7 & z^{14} & z^{21} & z^{28} & z^{35} & z^{42} & z^{49} \end{bmatrix} = F_8$$

8×8 DFT by 8×8 MMI

The transmission matrix of an 8×8 MMI is:

$$T = \begin{bmatrix} 1 & -z & z & -z^4 & z^4 & -z^9 & z^9 & -1 \\ -z & 1 & -z^4 & z & -z^9 & z^4 & -1 & z^9 \\ z & -z^4 & 1 & -z^9 & z & -1 & z^4 & -z^9 \\ -z^4 & z & -z^9 & 1 & -1 & z & -z^9 & z^4 \\ z^4 & -z^9 & z & -1 & 1 & -z^9 & z & -z^4 \\ -z^9 & z^4 & -1 & z & -z^9 & 1 & -z^4 & z \\ z^9 & -1 & z^4 & -z^9 & z & -z^4 & 1 & -z \\ -1 & z^9 & -z^9 & z^4 & -z^4 & z & -z & 1 \end{bmatrix} \quad ; \quad z = \exp(i\,\pi/8)$$

Re-phase

$$\Gamma = \text{diag}\begin{pmatrix} 1 \\ -z^{-1} \\ z^{-1} \\ -z^{-4} \\ z^{-4} \\ -z^{-9} \\ z^{-9} \\ -1 \end{pmatrix}$$

$$\Gamma T \Gamma = \text{diag}\begin{pmatrix} 1 \\ -z^{-1} \\ z^{-1} \\ -z^{-4} \\ z^{-4} \\ -z^{-9} \\ z^{-9} \\ -1 \end{pmatrix} \begin{bmatrix} 1 & -z & z & -z^4 & z^4 & -z^9 & z^9 & -1 \\ -z & 1 & -z^4 & z & -z^9 & z^4 & -1 & z^9 \\ z & -z^4 & 1 & -z^9 & z & -1 & z^4 & -z^9 \\ -z^4 & z & -z^9 & 1 & -1 & z & -z^9 & z^4 \\ z^4 & -z^9 & z & -1 & 1 & -z^9 & z & -z^4 \\ -z^9 & z^4 & -1 & z & -z^9 & 1 & -z^4 & z \\ z^9 & -1 & z^4 & -z^9 & z & -z^4 & 1 & -z \\ -1 & z^9 & -z^9 & z^4 & -z^4 & z & -z & 1 \end{bmatrix} \text{diag}\begin{pmatrix} 1 \\ -z^{-1} \\ z^{-1} \\ -z^{-4} \\ z^{-4} \\ -z^{-9} \\ z^{-9} \\ -1 \end{pmatrix}$$

$$\Gamma T \Gamma = \begin{bmatrix} 1 & -z & z & -z^4 & z^4 & -z^9 & z^9 & -1 \\ 1 & -z^{-1} & z^3 & -1 & z^8 & -z^3 & z^{-1} & -z^8 \\ 1 & -z^3 & z^{-1} & -z^8 & 1 & -z^{-1} & z^3 & -z^8 \\ 1 & -z^{-3} & z^5 & -z^{-4} & z^{-4} & -z^{-3} & z^5 & -1 \\ 1 & -z^5 & z^{-3} & -z^{-4} & z^{-4} & -z^5 & z^{-3} & -1 \\ 1 & -z^{-5} & z^{-9} & -z^{-8} & 1 & -z^{-9} & z^{-5} & -z^{-8} \\ 1 & -z^{-9} & z^{-5} & -1 & z^{-8} & -z^{-5} & z^{-9} & -z^{-8} \\ 1 & -z^9 & z^9 & -z^4 & z^4 & -z & z & -1 \end{bmatrix} \text{diag}\begin{pmatrix} 1 \\ -z^{-1} \\ z^{-1} \\ -z^{-4} \\ z^{-4} \\ -z^{-9} \\ z^{-9} \\ -1 \end{pmatrix}$$

$$\Gamma T\Gamma = \begin{bmatrix} 1 & 1 & 1 & 1 & 1 & 1 & 1 & 1 \\ 1 & z^{-2} & z^{2} & z^{-4} & z^{4} & z^{-6} & z^{-10} & z^{8} \\ 1 & z^{2} & z^{-2} & z^{4} & z^{-4} & z^{-10} & z^{-6} & z^{8} \\ 1 & z^{-4} & z^{4} & -1 & z^{-8} & z^{-12} & z^{-4} & 1 \\ 1 & z^{4} & z^{-4} & z^{-8} & z^{-8} & z^{-4} & z^{-12} & 1 \\ 1 & z^{-6} & z^{-10} & z^{-12} & z^{-4} & z^{-18} & z^{-14} & z^{-8} \\ 1 & z^{-10} & z^{-6} & z^{-4} & z^{-12} & z^{-14} & z^{-18} & z^{-8} \\ 1 & z^{8} & z^{8} & 1 & 1 & z^{-8} & z^{-8} & 1 \end{bmatrix}$$

But:

$$z^{16} = 1$$

Hence:

$$\Gamma T\Gamma = \begin{bmatrix} 1 & 1 & 1 & 1 & 1 & 1 & 1 & 1 \\ 1 & z^{14} & z^{2} & z^{12} & z^{4} & z^{10} & z^{6} & z^{8} \\ 1 & z^{2} & z^{14} & z^{4} & z^{12} & z^{6} & z^{10} & z^{8} \\ 1 & z^{12} & z^{4} & -1 & z^{8} & z^{4} & z^{12} & 1 \\ 1 & z^{4} & z^{12} & z^{8} & z^{8} & z^{12} & z^{4} & 1 \\ 1 & z^{10} & z^{6} & z^{4} & z^{12} & z^{14} & z^{2} & z^{8} \\ 1 & z^{6} & z^{10} & z^{12} & z^{4} & z^{2} & z^{14} & z^{8} \\ 1 & z^{8} & z^{8} & 1 & 1 & z^{8} & z^{8} & 1 \end{bmatrix} \quad ; \quad \Gamma = \text{diag} \begin{pmatrix} z^{0} \\ z^{7} \\ z^{15} \\ z^{4} \\ z^{12} \\ z^{15} \\ z^{7} \\ z^{8} \end{pmatrix}$$

Now:

$$F_8 = \begin{bmatrix} w^0 & w^0 & w^0 & w^0 & w^0 & w^0 & w^0 & w^0 \\ w^0 & w^1 & w^2 & w^3 & w^4 & w^5 & w^6 & w^7 \\ w^0 & w^2 & w^4 & w^6 & w^8 & w^{10} & w^{12} & w^{14} \\ w^0 & w^3 & w^6 & w^9 & w^{12} & w^{15} & w^{18} & w^{21} \\ w^0 & w^4 & w^8 & w^{12} & w^{16} & w^{20} & w^{24} & w^{28} \\ w^0 & w^5 & w^{10} & w^{15} & w^{20} & w^{25} & w^{30} & w^{35} \\ w^0 & w^6 & w^{12} & w^{18} & w^{24} & w^{30} & w^{36} & w^{42} \\ w^0 & w^7 & w^{14} & w^{21} & w^{28} & w^{35} & w^{42} & w^{49} \end{bmatrix} \quad ; \quad w = \exp(i\,2\pi/8)$$

Equivalently:

$$F_8 = \begin{bmatrix} w^0 & w^0 & w^0 & w^0 & w^0 & w^0 & w^0 & w^0 \\ w^0 & w^1 & w^2 & w^3 & w^4 & w^5 & w^6 & w^7 \\ w^0 & w^2 & w^4 & w^6 & w^0 & w^2 & w^4 & w^6 \\ w^0 & w^3 & w^6 & w^1 & w^4 & w^7 & w^2 & w^5 \\ w^0 & w^4 & w^0 & w^4 & w^0 & w^4 & w^0 & w^4 \\ w^0 & w^5 & w^2 & w^7 & w^4 & w^1 & w^6 & w^3 \\ w^0 & w^6 & w^4 & w^2 & w^0 & w^6 & w^4 & w^2 \\ w^0 & w^7 & w^6 & w^5 & w^4 & w^3 & w^2 & w^1 \end{bmatrix}$$

$$\Gamma T\Gamma = \begin{bmatrix} w^0 & w^0 & w^0 & w^0 & w^0 & w^0 & w^0 & w^0 \\ w^0 & w^7 & w^1 & w^6 & w^2 & w^5 & w^3 & w^4 \\ w^0 & w^1 & w^7 & w^2 & w^6 & w^3 & w^5 & w^4 \\ w^0 & w^6 & w^2 & w^4 & w^4 & w^2 & w^6 & w^0 \\ w^0 & w^2 & w^6 & w^4 & w^4 & w^6 & w^2 & w^0 \\ w^0 & w^5 & w^3 & w^2 & w^6 & w^7 & w^1 & w^4 \\ w^0 & w^3 & w^5 & w^6 & w^2 & w^1 & w^7 & w^4 \\ w^0 & w^4 & w^4 & w^0 & w^0 & w^4 & w^4 & w^0 \end{bmatrix} \quad ; \quad \Gamma = \text{diag} \begin{pmatrix} w^0 \\ w^{3.5} \\ w^{7.5} \\ w^2 \\ w^6 \\ w^{7.5} \\ w^{3.5} \\ w^4 \end{pmatrix}$$

Permutations:

Columns $(0,1,2,3,4,5,6,7) \longrightarrow (0,7,1,6,2,5,3,4)$

$$Q = \begin{bmatrix} 1 & 0 & 0 & 0 & 0 & 0 & 0 & 0 \\ 0 & 0 & 1 & 0 & 0 & 0 & 0 & 0 \\ 0 & 0 & 0 & 0 & 1 & 0 & 0 & 0 \\ 0 & 0 & 0 & 0 & 0 & 0 & 1 & 0 \\ 0 & 0 & 0 & 0 & 0 & 0 & 0 & 1 \\ 0 & 0 & 0 & 0 & 0 & 1 & 0 & 0 \\ 0 & 0 & 0 & 1 & 0 & 0 & 0 & 0 \\ 0 & 1 & 0 & 0 & 0 & 0 & 0 & 0 \end{bmatrix}$$

$$\Gamma T \Gamma Q = \begin{bmatrix} w^0 & w^0 & w^0 & w^0 & w^0 & w^0 & w^0 & w^0 \\ w^0 & w^1 & w^2 & w^3 & w^4 & w^5 & w^6 & w^7 \\ w^0 & w^7 & w^6 & w^5 & w^4 & w^3 & w^2 & w^1 \\ w^0 & w^2 & w^4 & w^6 & w^0 & w^2 & w^4 & w^6 \\ w^0 & w^6 & w^4 & w^2 & w^0 & w^6 & w^4 & w^2 \\ w^0 & w^3 & w^6 & w^1 & w^4 & w^7 & w^2 & w^5 \\ w^0 & w^5 & w^2 & w^7 & w^4 & w^1 & w^6 & w^3 \\ w^0 & w^4 & w^0 & w^4 & w^0 & w^4 & w^0 & w^4 \end{bmatrix}$$

Rows $(0,1,2,3,4,5,6,7) \longrightarrow (0,1,7,2,6,3,5,4)$

$$P = \begin{bmatrix} 1 & 0 & 0 & 0 & 0 & 0 & 0 & 0 \\ 0 & 1 & 0 & 0 & 0 & 0 & 0 & 0 \\ 0 & 0 & 0 & 1 & 0 & 0 & 0 & 0 \\ 0 & 0 & 0 & 0 & 0 & 1 & 0 & 0 \\ 0 & 0 & 0 & 0 & 0 & 0 & 0 & 1 \\ 0 & 0 & 0 & 0 & 0 & 0 & 1 & 0 \\ 0 & 0 & 0 & 0 & 1 & 0 & 0 & 0 \\ 0 & 0 & 1 & 0 & 0 & 0 & 0 & 0 \end{bmatrix}$$

$$P\Gamma T \Gamma Q = \begin{bmatrix} w^0 & w^0 & w^0 & w^0 & w^0 & w^0 & w^0 & w^0 \\ w^0 & w^1 & w^2 & w^3 & w^4 & w^5 & w^6 & w^7 \\ w^0 & w^2 & w^4 & w^6 & w^0 & w^2 & w^4 & w^6 \\ w^0 & w^3 & w^6 & w^1 & w^4 & w^7 & w^2 & w^5 \\ w^0 & w^4 & w^0 & w^4 & w^0 & w^4 & w^0 & w^4 \\ w^0 & w^5 & w^2 & w^7 & w^4 & w^1 & w^6 & w^3 \\ w^0 & w^6 & w^4 & w^2 & w^0 & w^6 & w^4 & w^2 \\ w^0 & w^7 & w^6 & w^5 & w^4 & w^3 & w^2 & w^1 \end{bmatrix} = F_8$$

Hence the transmission matrix of $8x8$ MMI is re-phasing permutation equivalent to an $8x8$ DFT.

8×8 DFT Coupler Network

A coupler network is desired with a transmission matrix given by:

$$F_8 = \frac{1}{\sqrt{8}} \begin{bmatrix} z^0 & z^0 & z^0 & z^0 & z^0 & z^0 & z^0 & z^0 \\ z^0 & z^1 & z^2 & z^3 & z^4 & z^5 & z^6 & z^7 \\ z^0 & z^2 & z^4 & z^6 & z^8 & z^{10} & z^{12} & z^{14} \\ z^0 & z^3 & z^6 & z^9 & z^{12} & z^{15} & z^{18} & z^{21} \\ z^0 & z^4 & z^8 & z^{12} & z^{16} & z^{20} & z^{24} & z^{28} \\ z^0 & z^5 & z^{10} & z^{15} & z^{20} & z^{25} & z^{30} & z^{35} \\ z^0 & z^6 & z^{12} & z^{18} & z^{24} & z^{30} & z^{36} & z^{42} \\ z^0 & z^7 & z^{14} & z^{21} & z^{28} & z^{35} & z^{42} & z^{49} \end{bmatrix} \quad ; \quad z = \exp(\pm i\, 2\pi/8)$$

This may be rewritten:

$$F_8 = \frac{1}{\sqrt{8}}\begin{bmatrix} (z^2)^0 & (z^2)^0 & (z^2)^0 & (z^2)^0 & (z^2)^0 & (z^2)^0 & (z^2)^0 & (z^2)^0 \\ (z^2)^0 z^0 & (z^2)^0 z^1 & (z^2)^0 z^2 & (z^2)^0 z^3 & (z^2)^0 z^4 & (z^2)^0 z^5 & (z^2)^0 z^6 & (z^2)^0 z^7 \\ (z^2)^0 & (z^2)^1 & (z^2)^2 & (z^2)^3 & (z^2)^0 & (z^2)^1 & (z^2)^2 & (z^2)^3 \\ (z^2)^0 z^0 & (z^2)^1 z^1 & (z^2)^2 z^2 & (z^2)^3 z^3 & (z^2)^0 z^4 & (z^2)^1 z^5 & (z^2)^2 z^6 & (z^2)^3 z^7 \\ (z^2)^0 & (z^2)^2 & (z^2)^4 & (z^2)^6 & (z^2)^0 & (z^2)^2 & (z^2)^4 & (z^2)^6 \\ (z^2)^0 z^0 & (z^2)^2 z^1 & (z^2)^4 z^2 & (z^2)^6 z^3 & (z^2)^0 z^4 & (z^2)^2 z^5 & (z^2)^4 z^6 & (z^2)^{14} z^7 \\ (z^2)^0 & (z^2)^3 & (z^2)^6 & (z^2)^9 & (z^2)^0 & (z^2)^3 & (z^2)^6 & (z^2)^9 \\ (z^2)^0 z^0 & (z^2)^3 z^1 & (z^2)^6 z^2 & (z^2)^9 z^3 & (z^2)^0 z^4 & (z^2)^3 z^5 & (z^2)^6 z^6 & (z^2)^9 z^7 \end{bmatrix}$$

Note:

$$\frac{1}{\sqrt{8}}\begin{bmatrix} (z^2)^0 & (z^2)^0 & (z^2)^0 & (z^2)^0 \\ (z^2)^0 & (z^2)^0 & (z^2)^2 & (z^2)^3 \\ (z^2)^0 & (z^2)^2 & (z^2)^4 & (z^2)^6 \\ (z^2)^0 & (z^2)^3 & (z^2)^6 & (z^2)^9 \end{bmatrix} \equiv \frac{1}{\sqrt{2}} F_4$$

$$\frac{1}{\sqrt{8}}\begin{bmatrix} (z^2)^0 z^0 & (z^2)^0 z^1 & (z^2)^0 z^2 & (z^2)^0 z^3 \\ (z^2)^0 z^0 & (z^2)^1 z^1 & (z^2)^2 z^2 & (z^2)^3 z^3 \\ (z^2)^0 z^0 & (z^2)^2 z^1 & (z^2)^4 z^2 & (z^2)^6 z^3 \\ (z^2)^0 z^0 & (z^2)^3 z^1 & (z^2)^6 z^2 & (z^2)^9 z^3 \end{bmatrix} = \frac{1}{\sqrt{8}}\begin{bmatrix} (z^2)^0 & (z^2)^0 & (z^2)^0 & (z^2)^0 \\ (z^2)^0 & (z^2)^0 & (z^2)^2 & (z^2)^3 \\ (z^2)^0 & (z^2)^2 & (z^2)^4 & (z^2)^6 \\ (z^2)^0 & (z^2)^3 & (z^2)^6 & (z^2)^9 \end{bmatrix}\begin{bmatrix} z^0 & 0 & 0 & 0 \\ 0 & z^1 & 0 & 0 \\ 0 & 0 & z^2 & 0 \\ 0 & 0 & 0 & z^3 \end{bmatrix}$$

$$\equiv \frac{1}{\sqrt{2}} F_4 \,\mathrm{diag}([z^0, z^1, z^2, z^3])$$

$$\frac{1}{\sqrt{2}}\begin{bmatrix} 1 & 1 \\ 1 & -1 \end{bmatrix} \equiv F_2$$

$$\frac{1}{\sqrt{8}}\begin{bmatrix} (z^2)^0 z^4 & (z^2)^0 z^5 & (z^2)^0 z^6 & (z^2)^0 z^7 \\ (z^2)^0 z^4 & (z^2)^1 z^5 & (z^2)^2 z^6 & (z^2)^3 z^7 \\ (z^2)^0 z^4 & (z^2)^2 z^5 & (z^2)^4 z^6 & (z^2)^{14} z^7 \\ (z^2)^0 z^4 & (z^2)^3 z^5 & (z^2)^6 z^6 & (z^2)^9 z^7 \end{bmatrix} = -\frac{1}{\sqrt{8}}\begin{bmatrix} (z^2)^0 z^0 & (z^2)^0 z^1 & (z^2)^0 z^2 & (z^2)^0 z^3 \\ (z^2)^0 z^0 & (z^2)^1 z^1 & (z^2)^2 z^2 & (z^2)^3 z^3 \\ (z^2)^0 z^0 & (z^2)^2 z^1 & (z^2)^4 z^2 & (z^2)^6 z^3 \\ (z^2)^0 z^0 & (z^2)^3 z^1 & (z^2)^6 z^2 & (z^2)^9 z^3 \end{bmatrix}$$

$$\equiv -\frac{1}{\sqrt{2}} F_4 \,\mathrm{diag}([z^0, z^1, z^2, z^3])$$

A 2x2 MMI transmission matrix is re-phasing equivalent to F_2. A 4×4 MMI transmission matrix is re-phasing-permutation-equivalent to F_4. Account must be taken of the re-phasing and permutations. However, re-ordering and re-phasing of output ports most likely can be neglected and the re-phasing phase shifts consolidated with other phase shifts. The ordering of the inputs above suits differential drive MZI – the F_2 couplers are then the output couplers of the MZI. The transpose of the above network may be used as the input coupler (it may be partially equipped if only one input is used). The rephrasing phase shifts within the MZI arms then conveniently cancel.

Note the path length of all the links in the diagram above are taken as zero. In practice this means paths between stages must be matched. The cross-over interconnect above is in that respect in convenient. One can implement crossovers using MMIs and other coupler structures and the phase-shifts incurred are in principle predictable and can be compensated.

Equivalence $mod\ q$=16

$$\equiv \begin{bmatrix}
0 & 0 & 0 & 0 & 0 & 0 & 0 & 0 & 0 & 0 & 0 & 0 & 0 & 0 & 0 & 0 \\
0 & 15 & 1 & 14 & 2 & 13 & 3 & 12 & 4 & 11 & 5 & 10 & 6 & 9 & 7 & 8 \\
0 & 1 & 15 & 2 & 14 & 3 & 13 & 4 & 12 & 5 & 11 & 6 & 10 & 7 & 9 & 8 \\
0 & 14 & 2 & 12 & 4 & 10 & 6 & 8 & 8 & 6 & 10 & 4 & 12 & 2 & 14 & 0 \\
0 & 2 & 14 & 4 & 12 & 6 & 10 & 8 & 8 & 10 & 6 & 12 & 4 & 14 & 2 & 0 \\
0 & 13 & 3 & 10 & 6 & 7 & 9 & 4 & 12 & 1 & 15 & 14 & 2 & 11 & 5 & 8 \\
0 & 3 & 13 & 6 & 10 & 9 & 7 & 12 & 4 & 15 & 1 & 2 & 14 & 5 & 11 & 8 \\
0 & 12 & 4 & 8 & 8 & 4 & 12 & 0 & 0 & 12 & 4 & 8 & 8 & 4 & 12 & 0 \\
0 & 4 & 12 & 8 & 8 & 12 & 4 & 0 & 0 & 4 & 12 & 8 & 8 & 12 & 4 & 0 \\
0 & 11 & 5 & 6 & 10 & 1 & 15 & 12 & 4 & 7 & 9 & 2 & 14 & 13 & 3 & 8 \\
0 & 5 & 11 & 10 & 6 & 15 & 1 & 4 & 12 & 9 & 7 & 14 & 2 & 3 & 13 & 8 \\
0 & 10 & 6 & 4 & 12 & 14 & 2 & 8 & 8 & 2 & 14 & 12 & 4 & 6 & 10 & 0 \\
0 & 6 & 10 & 12 & 4 & 2 & 14 & 8 & 8 & 14 & 2 & 4 & 12 & 10 & 6 & 0 \\
0 & 9 & 7 & 2 & 14 & 11 & 5 & 4 & 12 & 13 & 3 & 6 & 10 & 15 & 1 & 8 \\
0 & 7 & 9 & 14 & 2 & 5 & 11 & 12 & 4 & 3 & 13 & 10 & 6 & 1 & 15 & 8 \\
0 & 8 & 8 & 0 & 0 & 8 & 8 & 0 & 0 & 8 & 8 & 0 & 0 & 8 & 8 & 0
\end{bmatrix}$$

Reorder columns:

$$\rightarrow \begin{bmatrix}
0 & 0 & 0 & 0 & 0 & 0 & 0 & 0 & 0 & 0 & 0 & 0 & 0 & 0 & 0 & 0 \\
0 & 1 & 2 & 3 & 4 & 5 & 6 & 7 & 8 & 9 & 10 & 11 & 12 & 13 & 14 & 15 \\
0 & 15 & 14 & 13 & 12 & 11 & 10 & 9 & 8 & 7 & 6 & 5 & 4 & 3 & 2 & 1 \\
0 & 2 & 4 & 6 & 8 & 10 & 12 & 14 & 0 & 2 & 4 & 6 & 8 & 10 & 12 & 14 \\
0 & 14 & 12 & 10 & 8 & 6 & 4 & 2 & 0 & 14 & 12 & 10 & 8 & 6 & 4 & 2 \\
0 & 3 & 6 & 9 & 12 & 15 & 2 & 5 & 8 & 11 & 14 & 1 & 4 & 7 & 10 & 13 \\
0 & 13 & 10 & 7 & 4 & 1 & 14 & 11 & 8 & 5 & 2 & 15 & 12 & 9 & 6 & 3 \\
0 & 4 & 8 & 12 & 0 & 4 & 8 & 12 & 0 & 4 & 8 & 12 & 0 & 4 & 8 & 12 \\
0 & 12 & 8 & 4 & 0 & 12 & 8 & 4 & 0 & 12 & 8 & 4 & 0 & 12 & 8 & 4 \\
0 & 5 & 10 & 15 & 4 & 9 & 14 & 3 & 8 & 13 & 2 & 7 & 12 & 1 & 6 & 11 \\
0 & 11 & 6 & 1 & 12 & 7 & 2 & 13 & 8 & 3 & 14 & 9 & 4 & 15 & 10 & 5 \\
0 & 6 & 12 & 2 & 8 & 14 & 4 & 10 & 0 & 6 & 12 & 2 & 8 & 14 & 4 & 10 \\
0 & 10 & 4 & 14 & 8 & 2 & 12 & 6 & 0 & 10 & 4 & 14 & 8 & 2 & 12 & 6 \\
0 & 7 & 14 & 5 & 12 & 3 & 10 & 1 & 8 & 15 & 6 & 13 & 4 & 11 & 2 & 9 \\
0 & 9 & 2 & 11 & 4 & 13 & 6 & 15 & 8 & 1 & 10 & 3 & 12 & 5 & 14 & 7 \\
0 & 8 & 0 & 8 & 0 & 8 & 0 & 8 & 0 & 8 & 0 & 8 & 0 & 8 & 0 & 8
\end{bmatrix}$$

Reorder rows:

$$\rightarrow \begin{bmatrix}
0 & 0 & 0 & 0 & 0 & 0 & 0 & 0 & 0 & 0 & 0 & 0 & 0 & 0 & 0 & 0 \\
0 & 1 & 2 & 3 & 4 & 5 & 6 & 7 & 8 & 9 & 10 & 11 & 12 & 13 & 14 & 15 \\
0 & 2 & 4 & 6 & 8 & 10 & 12 & 14 & 0 & 2 & 4 & 6 & 8 & 10 & 12 & 14 \\
0 & 3 & 6 & 9 & 12 & 15 & 2 & 5 & 8 & 11 & 14 & 1 & 4 & 7 & 10 & 13 \\
0 & 4 & 8 & 12 & 0 & 4 & 8 & 12 & 0 & 4 & 8 & 12 & 0 & 4 & 8 & 12 \\
0 & 5 & 10 & 15 & 4 & 9 & 14 & 3 & 8 & 13 & 2 & 7 & 12 & 1 & 6 & 11 \\
0 & 6 & 12 & 2 & 8 & 14 & 4 & 10 & 0 & 6 & 12 & 2 & 8 & 14 & 4 & 10 \\
0 & 7 & 14 & 5 & 12 & 3 & 10 & 1 & 8 & 15 & 6 & 13 & 4 & 11 & 2 & 9 \\
0 & 8 & 0 & 8 & 0 & 8 & 0 & 8 & 0 & 8 & 0 & 8 & 0 & 8 & 0 & 8 \\
0 & 9 & 2 & 11 & 4 & 13 & 6 & 15 & 8 & 1 & 10 & 3 & 12 & 5 & 14 & 7 \\
0 & 10 & 4 & 14 & 8 & 2 & 12 & 6 & 0 & 10 & 4 & 14 & 8 & 2 & 12 & 6 \\
0 & 11 & 6 & 1 & 12 & 7 & 2 & 13 & 8 & 3 & 14 & 9 & 4 & 15 & 10 & 5 \\
0 & 12 & 8 & 4 & 0 & 12 & 8 & 4 & 0 & 12 & 8 & 4 & 0 & 12 & 8 & 4 \\
0 & 13 & 10 & 7 & 4 & 1 & 14 & 11 & 8 & 5 & 2 & 15 & 4 & 9 & 6 & 3 \\
0 & 14 & 12 & 10 & 8 & 6 & 4 & 2 & 0 & 14 & 12 & 10 & 8 & 6 & 4 & 2 \\
0 & 15 & 14 & 13 & 12 & 11 & 10 & 9 & 8 & 7 & 6 & 5 & 4 & 3 & 2 & 1
\end{bmatrix}$$

Unwrap powers

$$\equiv \begin{bmatrix} 0 & 0 & 0 & 0 & 0 & 0 & 0 & 0 & 0 & 0 & 0 & 0 & 0 & 0 & 0 & 0 \\ 0 & 1 & 2 & 3 & 4 & 5 & 6 & 7 & 8 & 9 & 10 & 11 & 12 & 13 & 14 & 15 \\ 0 & 2 & 4 & 6 & 8 & 10 & 12 & 14 & 16 & 18 & 20 & 22 & 24 & 26 & 28 & 30 \\ 0 & 3 & 6 & 9 & 12 & 15 & 18 & 21 & 24 & 27 & 30 & 33 & 36 & 39 & 42 & 45 \\ 0 & 4 & 8 & 12 & 16 & 20 & 24 & 28 & 32 & 36 & 40 & 44 & 48 & 52 & 56 & 60 \\ 0 & 5 & 10 & 15 & 20 & 25 & 30 & 35 & 40 & 45 & 50 & 55 & 60 & 65 & 70 & 75 \\ 0 & 6 & 12 & 18 & 24 & 30 & 36 & 42 & 48 & 54 & 60 & 66 & 72 & 78 & 84 & 90 \\ 0 & 7 & 14 & 21 & 28 & 35 & 42 & 49 & 56 & 63 & 70 & 77 & 84 & 91 & 98 & 105 \\ 0 & 8 & 16 & 24 & 32 & 40 & 48 & 56 & 64 & 72 & 80 & 88 & 96 & 104 & 112 & 120 \\ 0 & 9 & 18 & 27 & 36 & 45 & 54 & 63 & 72 & 81 & 90 & 99 & 108 & 117 & 126 & 135 \\ 0 & 10 & 20 & 30 & 40 & 50 & 60 & 70 & 80 & 90 & 100 & 110 & 120 & 130 & 140 & 150 \\ 0 & 11 & 22 & 33 & 44 & 55 & 66 & 77 & 88 & 99 & 110 & 121 & 132 & 143 & 154 & 165 \\ 0 & 12 & 24 & 36 & 48 & 60 & 72 & 84 & 96 & 108 & 120 & 134 & 144 & 156 & 168 & 180 \\ 0 & 13 & 26 & 39 & 52 & 65 & 78 & 91 & 104 & 117 & 130 & 143 & 156 & 169 & 182 & 195 \\ 0 & 14 & 28 & 42 & 56 & 70 & 84 & 98 & 112 & 14 & 140 & 154 & 168 & 182 & 196 & 210 \\ 0 & 15 & 30 & 45 & 60 & 75 & 90 & 105 & 120 & 135 & 150 & 165 & 180 & 195 & 210 & 255 \end{bmatrix} = F_{16}$$

It has been established the transmission matrix of a $q \times q$ MMI is permutation-phase equivalent to a $q \times q$ DFT for $q = 2, 4, 6, 8, 16$. The special cases do not constitute a proof but there seems no impediment to the equivalence for all even q. It is conjectured that the equivalence holds for all odd q but different formulae then apply.

MMI DFT Equivalence Odd Dimensions

Equivalence $mod\ q = 7$

$$T_{MMI} = \frac{1}{\sqrt{7}} \begin{bmatrix} -z & z & -z^9 & z^9 & -z^{11} & z^{11} & -z^7 \\ z & -z^9 & z & -z^{11} & z^9 & -z^7 & z^{11} \\ -z^9 & z & -z^{11} & z & -z^7 & z^9 & -z^{11} \\ z^9 & -z^{11} & z & -z^7 & z & -z^{11} & z^9 \\ -z^{11} & z^9 & -z^7 & z & -z^{11} & z & -z^9 \\ z^{11} & -z^7 & z^9 & -z^{11} & z & -z^9 & z \\ -z^7 & z^{11} & -z^{11} & z^9 & -z^9 & z & -z \end{bmatrix} \quad ; \quad z = \exp(i\,\pi/7)$$

Rewrite:

$$T_{MMI} = -z \frac{1}{\sqrt{7}} \begin{bmatrix} 1 & -1 & z^8 & -z^8 & z^{10} & -z^{10} & z^6 \\ -1 & z^8 & -1 & z^{10} & -z^8 & z^6 & -z^{10} \\ z^8 & -1 & z^{10} & -1 & z^6 & -z^8 & z^{10} \\ -z^8 & z^{10} & -1 & z^6 & -1 & z^{10} & -z^8 \\ z^{10} & -z^8 & z^6 & -1 & z^{10} & -1 & z^8 \\ -z^{10} & z^6 & -z^8 & z^{10} & -1 & z^8 & -1 \\ z^6 & -z^{10} & z^{10} & -z^8 & z^8 & -1 & 1 \end{bmatrix} \quad ; \quad z = \exp(i\,\pi/7)$$

Set:

$$\Gamma = \mathrm{diag}([1, -1, z^{-8}, -z^{-8}, z^{-10}, -z^{-10}, z^{-6}])$$

De-phase:

$$\Gamma T_{MMI}\Gamma = -z\frac{1}{\sqrt{7}}\begin{bmatrix}1 & 1 & 1 & 1 & 1 & 1 & 1\\ 1 & z^{8} & z^{-8} & z^{2} & z^{-2} & z^{-4} & z^{4}\\ 1 & z^{-8} & z^{-6} & z^{-16} & z^{-12} & z^{-10} & z^{-4}\\ 1 & z^{2} & z^{-16} & z^{-10} & z^{-18} & z^{-8} & z^{-6}\\ 1 & z^{-2} & z^{-12} & z^{-18} & z^{-10} & z^{-20} & z^{-8}\\ 1 & z^{-4} & z^{-10} & z^{-8} & z^{-20} & z^{-12} & z^{-16}\\ 1 & z^{4} & z^{-4} & z^{-6} & z^{-8} & z^{-16} & z^{-12}\end{bmatrix}$$

$$\Gamma T_{MMI}\Gamma \equiv -z\frac{1}{\sqrt{7}}\begin{bmatrix}1 & 1 & 1 & 1 & 1 & 1 & 1\\ 1 & z^{8} & z^{6} & z^{2} & z^{12} & z^{10} & z^{4}\\ 1 & z^{6} & z^{8} & z^{12} & z^{2} & z^{4} & z^{10}\\ 1 & z^{2} & z^{12} & z^{4} & z^{10} & z^{6} & z^{8}\\ 1 & z^{12} & z^{2} & z^{10} & z^{4} & z^{8} & z^{6}\\ 1 & z^{10} & z^{4} & z^{6} & z^{8} & z^{2} & z^{12}\\ 1 & z^{4} & z^{10} & z^{8} & z^{6} & z^{12} & z^{2}\end{bmatrix}$$

$$\begin{bmatrix}1 & 1 & 1 & 1 & 1 & 1 & 1\\ 1 & z^{8} & z^{6} & z^{2} & z^{12} & z^{10} & z^{4}\\ 1 & z^{6} & z^{8} & z^{12} & z^{2} & z^{4} & z^{10}\\ 1 & z^{2} & z^{12} & z^{4} & z^{10} & z^{6} & z^{8}\\ 1 & z^{12} & z^{2} & z^{10} & z^{4} & z^{8} & z^{6}\\ 1 & z^{10} & z^{4} & z^{6} & z^{8} & z^{2} & z^{12}\\ 1 & z^{4} & z^{10} & z^{8} & z^{6} & z^{12} & z^{2}\end{bmatrix} = \begin{bmatrix}w^{0} & w^{0} & w^{0} & w^{0} & w^{0} & w^{0} & w^{0}\\ w^{0} & w^{4} & w^{3} & w^{1} & w^{6} & w^{5} & w^{2}\\ w^{0} & w^{3} & w^{4} & w^{6} & w^{1} & w^{2} & w^{5}\\ w^{0} & w^{1} & w^{6} & w^{2} & w^{5} & w^{3} & w^{4}\\ w^{0} & w^{6} & w^{1} & w^{5} & w^{2} & w^{4} & w^{3}\\ w^{0} & w^{5} & w^{2} & w^{3} & w^{4} & w^{1} & w^{6}\\ w^{0} & w^{2} & w^{5} & w^{4} & w^{3} & w^{6} & w^{1}\end{bmatrix} \quad ; \quad w = \exp(i\,2\pi/7)$$

Re-order columns:

$$\begin{bmatrix}w^{0} & w^{0} & w^{0} & w^{0} & w^{0} & w^{0} & w^{0}\\ w^{0} & w^{4} & w^{3} & w^{1} & w^{6} & w^{5} & w^{2}\\ w^{0} & w^{3} & w^{4} & w^{6} & w^{1} & w^{2} & w^{5}\\ w^{0} & w^{1} & w^{6} & w^{2} & w^{5} & w^{3} & w^{4}\\ w^{0} & w^{6} & w^{1} & w^{5} & w^{2} & w^{4} & w^{3}\\ w^{0} & w^{5} & w^{2} & w^{3} & w^{4} & w^{1} & w^{6}\\ w^{0} & w^{2} & w^{5} & w^{4} & w^{3} & w^{6} & w^{1}\end{bmatrix} \longrightarrow \begin{bmatrix}w^{0} & w^{0} & w^{0} & w^{0} & w^{0} & w^{0} & w^{0}\\ w^{0} & w^{1} & w^{2} & w^{3} & w^{4} & w^{5} & w^{6}\\ w^{0} & w^{6} & w^{5} & w^{4} & w^{3} & w^{2} & w^{1}\\ w^{0} & w^{2} & w^{4} & w^{6} & w^{1} & w^{3} & w^{5}\\ w^{0} & w^{5} & w^{3} & w^{1} & w^{6} & w^{4} & w^{2}\\ w^{0} & w^{3} & w^{6} & w^{2} & w^{5} & w^{1} & w^{4}\\ w^{0} & w^{4} & w^{1} & w^{5} & w^{2} & w^{6} & w^{3}\end{bmatrix}$$

Re-order rows:

$$\begin{bmatrix}w^{0} & w^{0} & w^{0} & w^{0} & w^{0} & w^{0} & w^{0}\\ w^{0} & w^{1} & w^{2} & w^{3} & w^{4} & w^{5} & w^{6}\\ w^{0} & w^{6} & w^{5} & w^{4} & w^{3} & w^{2} & w^{1}\\ w^{0} & w^{2} & w^{4} & w^{6} & w^{1} & w^{3} & w^{5}\\ w^{0} & w^{5} & w^{3} & w^{1} & w^{6} & w^{4} & w^{2}\\ w^{0} & w^{3} & w^{6} & w^{2} & w^{5} & w^{1} & w^{4}\\ w^{0} & w^{4} & w^{1} & w^{5} & w^{2} & w^{6} & w^{3}\end{bmatrix} \longrightarrow \begin{bmatrix}w^{0} & w^{0} & w^{0} & w^{0} & w^{0} & w^{0} & w^{0}\\ w^{0} & w^{1} & w^{2} & w^{3} & w^{4} & w^{5} & w^{6}\\ w^{0} & w^{2} & w^{4} & w^{6} & w^{1} & w^{3} & w^{5}\\ w^{0} & w^{3} & w^{6} & w^{2} & w^{5} & w^{1} & w^{4}\\ w^{0} & w^{4} & w^{1} & w^{5} & w^{2} & w^{6} & w^{3}\\ w^{0} & w^{5} & w^{3} & w^{1} & w^{6} & w^{4} & w^{2}\\ w^{0} & w^{6} & w^{5} & w^{4} & w^{3} & w^{2} & w^{1}\end{bmatrix}$$

Unwrap powers:

$$\begin{bmatrix}w^{0} & w^{0} & w^{0} & w^{0} & w^{0} & w^{0} & w^{0}\\ w^{0} & w^{1} & w^{2} & w^{3} & w^{4} & w^{5} & w^{6}\\ w^{0} & w^{2} & w^{4} & w^{6} & w^{1} & w^{3} & w^{5}\\ w^{0} & w^{3} & w^{6} & w^{2} & w^{5} & w^{5} & w^{4}\\ w^{0} & w^{4} & w^{1} & w^{5} & w^{2} & w^{6} & w^{3}\\ w^{0} & w^{5} & w^{3} & w^{1} & w^{6} & w^{4} & w^{2}\\ w^{0} & w^{6} & w^{5} & w^{4} & w^{3} & w^{2} & w^{1}\end{bmatrix} \equiv \begin{bmatrix}w^{0} & w^{0} & w^{0} & w^{0} & w^{0} & w^{0} & w^{0}\\ w^{0} & w^{1} & w^{2} & w^{3} & w^{4} & w^{5} & w^{6}\\ w^{0} & w^{2} & w^{4} & w^{6} & w^{8} & w^{10} & w^{12}\\ w^{0} & w^{3} & w^{6} & w^{9} & w^{12} & w^{15} & w^{18}\\ w^{0} & w^{4} & w^{8} & w^{12} & w^{16} & w^{20} & w^{24}\\ w^{0} & w^{5} & w^{10} & w^{15} & w^{20} & w^{25} & w^{30}\\ w^{0} & w^{6} & w^{12} & w^{18} & w^{24} & w^{30} & w^{36}\end{bmatrix} = F_{7}$$

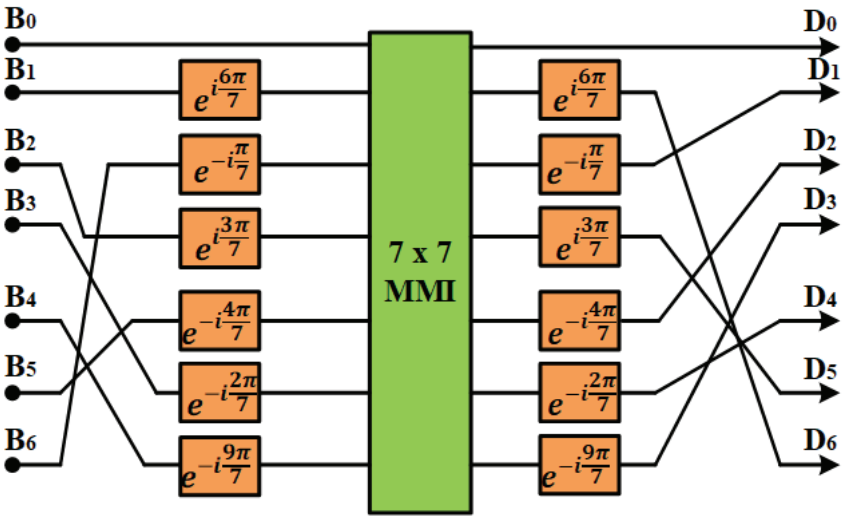

Figure A1.1: Realization of 7×7 DFT using 7×7 MMI.

The realization 7×7 DFT using 7×7 MMI is depicted in Fig. A1.1. It has been established that the transmission matrix of standard uniform split $q \times q$ MMI coupler is permutation-phase equivalent to a $q \times q$ DFT for $odd\ q$.

Appendix II. Script for the Complete Spectrometer Circuit Design Layout

```
// ----------------------------------------
// REFRESH
dsp::clearInfoWin(); mask::clearFiles(); mask::clearTV(); res::Clear();

// ----------------------------------------
// LOAD AND SELECT FOUNDRY, PACKAGING AND DESIGN HOUSES
pda::loadFoundry   ("foundryLionix_ADS");
pda::enableFoundry ("LIONIX.ADS");
#include @topview;
#include @layout;

// ----------------------------------------
// Die parameter

string maskfilename = "c:/temp/PhoeniX/mask/ski_laserBB_" ;
maskfilename = "c:/temp/PhoeniX/mask/ski_" ;
string projectname = "oU_PTLab_00" ;

//Place Laser only for Die Block 16x16 mm.
//If using Laser, FiberOptic unit on the right will be removed.
int placeLaser = 0 ; //1=yes, 0=no.

//Fiber Array Unit (FAU). Allowed values: 0, 8, 12, 16, 24, 28, or 32.
int amount_FiberOptic_Left  = 32 ;
int amount_FiberOptic_Right = 32 ;

//AlignmentWG = 0 : no Alignment waveguides, AlignmentWG = 4 : four Alignment Loop
waveguides.
int AlignmentWG = 4;

//DC pad: "ProbePad" or "BondPad".
string type_DC_pad = "BondPad" ;

//Amount of BondPad: 0, 20 (16 mm die size), 50 (32 mm die size with "pD" adapter).
//If you use the Laser, then you cannot set the amount_BondPad_bottom to zero
//because the laser is using the bond pads at the bottom.
int amount_BondPad_top = 20 ;
int amount_BondPad_bottom = 20 ;
```

```
//Only for Die Size 32 mm: BondPad type and placement.
//"pC" sets 20 BondPads, "pD" sets 50 BondPads.
string adapterTypeTop        = "pC" ; //"pC", "pD".
string adapterTypeBottom     = "pC" ; //"pC", "pD".
string adapterPlacementTop   = "Center" ; //"Center", "Left", "Right".
string adapterPlacementBottom= "Center" ; //"Center", "Left", "Right".

string showTemplateLogo = "no" ; //yes or no.

//!!! set SBoffset=0.
//Comment this script to use automatic SBoffset from PDK.
//techLionixADS.setSBoffset(0);

// ----------------------------------------
//FOUNDRY ENVIRONMENT.
//===== do NOT change this section!! =====
AlignmentWG=placeLaser?3:AlignmentWG;//placeLaser=1:AlignmentWG=3.
amount_BondPad_bottom=placeLaser?20:amount_BondPad_bottom;
techLionixADS.setWavelength(1.55);

Lionix_ADS_DieBB16x16(type_DC_pad) die;
//Lionix_ADS_DieBB32x8(type_DC_pad) die; //set placeLaser=0.
//Lionix_ADS_DieBB16x8(type_DC_pad) die; //set placeLaser=0.

die.showTemplateLogo(showTemplateLogo);

die.setFauLeft(amount_FiberOptic_Left);
if(placeLaser) die.setFauRight(0);
else die.setFauRight(amount_FiberOptic_Right);

die.setDCArrayTop(amount_BondPad_top);
die.setDCArrayBottom(amount_BondPad_bottom);

die.useSymmetricalDCPadTop();
die.useSymmetricalDCPadBot();

die.setBondPadTypeTop(adapterTypeTop);
die.setBondPadTypeBot(adapterTypeBottom);
```

```
die.setBondPadPositionTop(adapterPlacementTop);
die.setBondPadPositionBot(adapterPlacementBottom);

die.place(org->[0]:);

AlignmentWG_ADS(&die, AlignmentWG) align;
align.placeAlignmentWG();

LioniX_ADS_Laser(&die) LaserBB;
var laser; if(placeLaser) laser = LaserBB.place(:);

var block = die.getBox();

double blockW = block.Width, blockL = block.Length; printf("\nblockW=",blockW,", blockL=",
blockL, "\n");
ml::ShowPort(cin->block@org:"block@org", 10);

//mask::CScreate("mcsUserArea",virtual,RGB(0,0,0),true,false);
//var userArea=ml::Straight(bir->[250,250]:wfix(15.5E3),15.5E3);
//var user=ml::Offset(cin->userArea@bir:0,0,0);

// END : FOUNDRY ENVIRONMENT.
// ----------------------------------------

// ----------------------------------------
// YOUR MASK DESIGN.
// Select process layer.
mask::CSselect ("mcsWAVEGUIDE_ADS") ;

// Print technology info from the foundry's database.
printf ( mask::CSattr() , "\n" );

// Link your design to the technology specs in foundry's database.
double wwg = mcsGetWidth(); //mask::CSattr ( "wgWidth" );
double wR  = mcsGetRadius(); //mask::CSattr ( "wgRadius" );

double wavelength = techLionixADS.getWavelength();
double SBoffset=techLionixADS.GetSBoffset(wwg, wavelength, wR);

printf("\n--\n wavelength = "     , wavelength
```

```
    , "\n waveguide width = "    , wwg
    , "\n default bend Radius = ", wR
    , "\n SBoffset = "          , SBoffset
    ,"\n--\n");

//--------------My Design ----------------------
//Peng L, March 23, 2020 5:45pm:

//2)      Ring#2-2, (half heater,R=537um, gap=2.0um) + MZI 2 (delay=2x1695um,2x2
DC,50Ghz/0.4nm FSR, two heaters)
//3)      Ring#2-3, R=537um, full ring heater, gap=2.2um
//4)      Ring#2-4, R=537um, half ring heater, gap=2.2um

//5)      Coupling alignment layout 1, case 1
//6)      Coupling alignment layout 1, case 2
//7)      Coupling alignment layout 1, case 3

//9)      Bottom straight waveguide
//10) Coupling alignment layout 2, case 1
//11)    Coupling alignment layout 2, case 2
//12) Coupling alignment layout 2, case 3

//13)  MMI-MZI(delay=2x1695um,2x2 MMI,50Ghz/0.4nm FSR,two heaters)
//14)  1x2 splitter + delay line + 2x2 MMI(delay=2x1695um,2x2 MMI
//15)  1x2 splitter + delay line + 3x3 MMI(delay=2x1695um, 3x3MMI)

//16)    Top straight waveguide

//---------------------------------- ring 2-1, (full heater,R=537um, gap=2.0um)
mask::CSselect ("mcsWAVEGUIDE_ADS") ;
layout ring_BB_01 (width1=1.1, gap1=1.8, radius1=537)
{
ml::LxStraight( : 1280., width1, 0.5) E1;
ml::LxPhaseModulatorArc( in0 ->  E1@ccen +[0, width1+gap1, 0]:
            /* Heater_Angle = */ 275,
            /* Waveguide_Angle = */ 360,
            /* Waveguide_Width = */ width1,
            /* Radius = */ radius1,
            /* Lead1Angle = */ -90,
            /* Lead2Angle = */ -90,
```

```
            /* Lead1Up = */ 1,
            /* Lead2Up = */ 1,
            /* Wavelength = */ 1.55,
            /* simDeltaTemp = */ 0,
            /* simLoss = */ 0.5) E3;
ml::LxStraight( ccen -> E1@ccen + [0, +2*radius1+2*width1+2*gap1, 0] : 1280., width1, 0.5)
E2;

ml::setPort(E1 : in0 -> this@in0);
ml::setPort(E1 : out0 -> this@out0);
ml::setPort(E2 : in0 -> this@in1);
ml::setPort(E2 : out0 -> this@out1);
ml::setPort(E3 : dc0 -> this@dc1);
ml::setPort(E3 : dc1 -> this@dc0);
}

//---------------------------------- ring 2-2, (half heater,R=537um, gap=2.0um) + MZI 2
(delay=2x1695um,2x2 DC,50Ghz/0.4nm FSR,two heaters)
mask::CSselect ("mcsWAVEGUIDE_ADS") ;
layout ring_BB_02 (width1=1.1, gap1=1.8, radius1=537)
{
ml::LxStraight( : 1280., width1, 0.5) E1;
 ml::LxArc( in0 ->  E1@ccen +[0, width1+gap1, 0]:
            /* Waveguide_Angle = */ 180,
            /* Radius = */ radius1,
            /* Waveguide_Width = */ width1,
            /* Wavelength = */ 1.55,
            /* simLoss = */ 0.5) E4;
 ml::LxPhaseModulatorArc( in0 ->  E4@out0:
            /* Heater_Angle = */ 135,
            /* Waveguide_Angle = */ 180,
            /* Waveguide_Width = */ width1,
            /* Radius = */ radius1,
            /* Lead1Angle = */ 45,
            /* Lead2Angle = */ 45,
            /* Lead1Up = */ 1,
            /* Lead2Up = */ 1,
            /* Wavelength = */ 1.55,
            /* simDeltaTemp = */ 0,
            /* simLoss = */ 0.5) E3;
```

```
ml::LxStraight( ccen -> E1@ccen + [0, +2*radius1+2*width1+2*gap1, 0] : 1280., width1, 0.5)
E2;

ml::setPort(E1 : in0 -> this@in0);
ml::setPort(E1 : out0 -> this@out0);
ml::setPort(E2 : in0 -> this@in1);
ml::setPort(E2 : out0 -> this@out1);
ml::setPort(E3 : dc0 -> this@dc0);
ml::setPort(E3 : dc1 -> this@dc1);
}

var ring_02 = ml::ring_BB_02( in0->block@org +[3000, 5000, 0] : 1.1, 2.0, 537);

ml::pxConnectorSBendAdiabatic(from->block@out12 , to->ring_02@in0 : 700);
ml::pxConnectorSBendAdiabatic(from->block@out13 , to->ring_02@in1 : 750);

mask::CSselect ("mcsLEAD") ;
ml::pxConnectorCurveDC(from->block@dc2 , to->ring_02@dc1 :);
ml::pxConnectorCurveDC(from->block@dc3 , to->ring_02@dc0 :);
//---------------------------------

///---------------------------------- ,
layout LioniX_MZI_02(double T=20)

{
  mask::setLayoutPort(this, "in0", "out0");
  var RoutingGridElectrical = Tech.getDefaultOrNewAutoRouterGrid(this, "Electrical",
"LioniX_MZIElectrical", 40, 40);
  var RoutingGrid = Tech.getDefaultOrNewAutoRouterGrid(this, "Optical",
"LioniX_MZIOptical", 40, 40);

  mask::CSselect("mcsWAVEGUIDE_ADS");
  ml::LxArc(: 90,100.0,mcsGetWidth(),1.55,0.5) LxArc1;
  mask::CSselect("mcsWAVEGUIDE_ADS");
  ml::LxArc(: -90,100.0,mcsGetWidth(),1.55,0.5) LxArc2;
  mask::CSselect("mcsWAVEGUIDE_ADS");
  ml::LxArc(: -90,100.0,mcsGetWidth(),1.55,0.5) LxArc3;
  mask::CSselect("mcsWAVEGUIDE_ADS");
  ml::LxArc(: 90,100.0,mcsGetWidth(),1.55,0.5) LxArc4;
  mask::CSselect("mcsWAVEGUIDE_ADS");
```

```
  ml::LxArc(: -90,100.0,mcsGetWidth(),1.55,0.5) LxArc5;
  mask::CSselect("mcsWAVEGUIDE_ADS");
  ml::LxArc(in0->LxArc5@out0: 90,100.0,mcsGetWidth(),1.55,0.5) LxArc6;
  mask::CSselect("mcsWAVEGUIDE_ADS");
  ml::LxArc(: 90,100.0,mcsGetWidth(),1.55,0.5) LxArc7;
  mask::CSselect("mcsWAVEGUIDE_ADS");
  ml::LxArc(in0->LxArc7@out0: -90,100.0,mcsGetWidth(),1.55,0.5) LxArc8;
  mask::CSselect("mcsWAVEGUIDE_ADS");
  ml::LxDirectionalCoupler(out0->LxArc5@in0, out1->LxArc1@in0: 127,127,0.5)
LxDirectionalCoupler1;
  mask::CSselect("mcsWAVEGUIDE_ADS");
  ml::LxDirectionalCoupler(in0->LxArc8@out0, in1->LxArc4@out0: 127,127,0.5)
LxDirectionalCoupler3;
  mask::CSselect("mcsWAVEGUIDE_ADS");
  ml::LxPhaseModulator(in0->LxArc6@out0, out0->LxArc7@in0:
2000,2100,mcsGetWidth(),0,0,0,0,T,0.5,"yes") LxPhaseModulator1;
  mask::CSselect("mcsWAVEGUIDE_ADS");
  ml::LxPhaseModulator(in0->LxArc2@out0, out0->LxArc3@in0:
2000,2100,mcsGetWidth(),0,0,0,0,T,0.5,"yes") LxPhaseModulator2;
  mask::CSselect("mcsWAVEGUIDE_ADS");
  ml::LxStraight(out0->LxDirectionalCoupler1@in1: 100,mcsGetWidth(),0.5) LxStraight1;
  mask::CSselect("mcsWAVEGUIDE_ADS");
  ml::LxStraight(in0->LxDirectionalCoupler3@out1: 100,mcsGetWidth(),0.5) LxStraight3;
  mask::CSselect("mcsWAVEGUIDE_ADS");
  ml::LxStraight(in0->LxArc1@out0, out0->LxArc2@in0: 1695,mcsGetWidth(),0.5)
LxStraight4;
  mask::CSselect("mcsWAVEGUIDE_ADS");
  ml::LxStraight(in0->LxArc3@out0, out0->LxArc4@in0: 1695,mcsGetWidth(),0.5)
LxStraight5;
  mask::CSselect("mcsWAVEGUIDE_ADS");
  ml::LxStraight(out0->LxDirectionalCoupler1@in0: 100,mcsGetWidth(),0.5) LxStraight6;
  mask::CSselect("mcsWAVEGUIDE_ADS");
  ml::LxStraight(in0->LxDirectionalCoupler3@out0: 100,mcsGetWidth(),0.5) LxStraight7;


  // Stored element connections

  ml::setPort(LxStraight1 : in0->this@in0);
  ml::setPort(LxStraight6 : in0->this@in1);
```

```
  ml::setPort(LxStraight3 : out0->this@out0);
  ml::setPort(LxStraight7 : out0->this@out1);

  ml::setPort(LxPhaseModulator1 : dc1->this@dc0);
  ml::setPort(LxPhaseModulator1 : dc0->this@dc1);
  ml::setPort(LxPhaseModulator2 : dc1->this@dc2);
  ml::setPort(LxPhaseModulator2 : dc0->this@dc3);

  // Persist routing parameters into the MoML file
  this = Tech.populateAutoRouterInformation(this);

  // Set the promoted I/O ports domain
  mask::elementPortRegexSetDomain(this, "(in|out)([[:int:]])", OpticsDomain);

  mask::port2layout(&this);
}

ml::LioniX_MZI_02(in0->block@org+[8500, 4750] : ) mzi_02;

ml::pxConnectorSBendAdiabatic(from ->mzi_02@in0, to->ring_02@out1: 500);
ml::pxConnectorSBendAdiabatic(from ->mzi_02@in1, to->ring_02@out0: 550);
ml::pxConnectorSBendAdiabatic(from ->mzi_02@out1, to->block@out41: 550);
ml::pxConnectorSBendAdiabatic(from ->mzi_02@out0, to->block@out42: 500);

mask::CSselect("mcsLEAD");
ml::pxConnectorCurveDC(from ->block@dc10, to->mzi_02@dc1:);
ml::pxConnectorCurveDC(from ->block@dc19, to->mzi_02@dc0:);
ml::pxConnectorCurveDC(from ->block@dc8, to->mzi_02@dc3:);
ml::pxConnectorCurveDC(from ->block@dc20, to->mzi_02@dc2:);
//---------------------------------

//---------------------------------- ring 2-3, (full heater,R=537um, gap=2.2um)
//mask::CSselect ("mcsWAVEGUIDE_ADS") ;

//var ring_03 = ml::ring_BB_01( in0->block@org +[5200, 6250, 0] : 1.1, 2.2, 537);

//ml::pxConnectorSBendAdiabatic(from->block@out14 , to->ring_03@in0 : 800);
//ml::pxConnectorSBendAdiabatic(from->block@out15 , to->ring_03@in1 : 850);
//ml::pxConnectorSBendAdiabatic(from->block@out44 , to->ring_03@out0 :6700);
//ml::pxConnectorSBendAdiabatic(from->block@out45 , to->ring_03@out1 :6800);
```

```
//mask::CSselect ("mcsLEAD") ;
//ml::pxConnectorCurveDC(from->block@dc5 , to->ring_03@dc0 :);
//ml::pxConnectorCurveDC(from->block@dc6 , to->ring_03@dc1 :);
//---------------------------------

//--------------------------------- ring 2-4(half heater,R=537um, gap=2.2mm)
mask::CSselect ("mcsWAVEGUIDE_ADS") ;

var ring_04 = ml::ring_BB_02( in0->block@org +[3500, 6500, 0] : 1.1, 2.2, 537);

ml::pxConnectorSBendAdiabatic(from->block@out14 , to->ring_04@in0 : 900);
ml::pxConnectorSBendAdiabatic(from->block@out15 , to->ring_04@in1 : 950);
ml::pxConnectorSBendAdiabatic(from->block@out43 , to->ring_04@out0 :7500);
ml::pxConnectorSBendAdiabatic(from->block@out44 , to->ring_04@out1 :8000);

mask::CSselect ("mcsLEAD") ;
ml::pxConnectorCurveDC(from->block@dc37 , to->ring_04@dc0 :);
ml::pxConnectorCurveDC(from->block@dc34 , to->ring_04@dc1 :);
//---------------------------------

//--------------------------------- bottom straight waveguide
mask::CSselect ("mcsWAVEGUIDE_ADS") ;
ml::pxConnectorManhattan(from->block@out2 ,p0->block@org+[1250,900,0] ,p1-
>block@org+[14650,1400,0],to->block@out34: 2);
//---------------------------------

//--------------------------------- top straight waveguide
mask::CSselect ("mcsWAVEGUIDE_ADS") ;
ml::pxConnectorManhattan(from->block@out29 , p0->block@org+[1250,15000,0] ,p1-
>block@org+[14650,14500,0],to->block@out61: 2);
//---------------------------------

//--------------------------------- Coupling alignment layout 1, case 1
layout PC_layout_01(w=1.1, w1=1.1, w2=6.9, input_straight_length=1000.,
input_taper_length=50., output_taper_length=1000., output_straight_length=1000.)

{
 mask::CSselect("mcsWAVEGUIDE_ADS");
 ml::LxStraight( : input_straight_length, w, 0.5) In1;
```

```
 ml::LxTaper( in0 -> In1@out0: input_taper_length, w, w1, 0.5) Taper1;

 ml::LxTaper( bil -> Taper1@bol: output_taper_length, w2, w, 0.5) Taper4;
 ml::LxStraight( in0 -> Taper4@out0: output_straight_length, w, 0.5) Out1;

 ml::LxTaper( bol -> Taper4@bir: input_taper_length, w, w1, 0.5) Taper2;
 ml::LxStraight( out0 -> Taper2@in0: input_straight_length, w, 0.5) In2;

 ml::LxTaper( bil -> Taper2@bor: output_taper_length, w2, w, 0.5) Taper5;
 ml::LxStraight( in0 -> Taper5@out0: output_straight_length, w, 0.5) Out2;

 ml::LxTaper( boc -> Taper5@bic: input_taper_length, w, w1, 0.5) Taper3;
 ml::LxStraight( out0 -> Taper3@in0: input_straight_length, w, 0.5) In3;

ml::setPort(In1 : in0 -> this@in0);
ml::setPort(Out1 : out0 -> this@out0);
ml::setPort(In2 : in0 -> this@in1);
ml::setPort(Out2 : out0 -> this@out1);
ml::setPort(In3 : in0 -> this@in2);
}

var pcl_01 = ml::PC_layout_01(in0->block@org+[2000, 1500] : 1.1, 1.1, 6.9, 1000., 50.,1000.,
1000.);

mask::CSselect ("mcsWAVEGUIDE_ADS") ;
ml::pxConnectorSBendAdiabatic(from ->pcl_01@out1, to->block@out35: 9100);
ml::pxConnectorSBendAdiabatic(from ->pcl_01@out0, to->block@out36: 9000);

ml::pxConnectorSBendAdiabatic(from->pcl_01@in0 , to->block@out5 :500);
ml::pxConnectorSBendAdiabatic(from->pcl_01@in1 , to->block@out4 :550);
ml::pxConnectorSBendAdiabatic(from->pcl_01@in2 , to->block@out3 :600);
//---------------------------------

//---------------------------------- Coupling alignment layout 1, case 2
var pcl_02 = ml::PC_layout_01(in0->block@org+[2000, 2000] : 1.1, 2., 6., 1000., 250.,1000.,
1000.);

mask::CSselect ("mcsWAVEGUIDE_ADS") ;
ml::pxConnectorSBendAdiabatic(from ->pcl_02@out1, to->block@out37: 8600);
ml::pxConnectorSBendAdiabatic(from ->pcl_02@out0, to->block@out38: 8500);
```

```
ml::pxConnectorSBendAdiabatic(from->pcl_02@in0 , to->block@out8 :350);
ml::pxConnectorSBendAdiabatic(from->pcl_02@in1 , to->block@out7 :400);
ml::pxConnectorSBendAdiabatic(from->pcl_02@in2 , to->block@out6 :450);
//---------------------------------

//---------------------------------- Coupling alignment layout 1, case 3
var pcl_03 = ml::PC_layout_01(in0->block@org+[2000, 2500] : 1.1, 3., 7., 1000., 350.,1000.,
1000.);

mask::CSselect ("mcsWAVEGUIDE_ADS") ;
ml::pxConnectorSBendAdiabatic(from ->pcl_03@out1, to->block@out39: 8300);
ml::pxConnectorSBendAdiabatic(from ->pcl_03@out0, to->block@out40: 8200);

ml::pxConnectorSBendAdiabatic(from->pcl_03@in0 , to->block@out11 :200);
ml::pxConnectorSBendAdiabatic(from->pcl_03@in1 , to->block@out10 :250);
ml::pxConnectorSBendAdiabatic(from->pcl_03@in2 , to->block@out9 :300);
//---------------------------------

//---------------------------------- Coupling alignment layout 2, case 1
layout PC_layout_02(w=1.1, w1=1.1, w2=6.9, input_straight_length=1000.,
input_taper_length=50., output_taper_length=1000., output_straight_length=1000.)

{
 mask::CSselect("mcsWAVEGUIDE_ADS");
 ml::LxStraight( : input_straight_length, w, 0.5) In1;
 ml::LxTaper( in0 -> In1@out0: input_taper_length, w, w1, 0.5) Taper1;

 ml::LxTaper( bil -> Taper1@bor: output_taper_length, w2, w, 0.5) Taper4;
 ml::LxStraight( in0 -> Taper4@out0: output_straight_length, w, 0.5) Out1;

 ml::LxTaper( bor -> Taper4@bir: input_taper_length, w, w1, 0.5) Taper2;
 ml::LxStraight( out0 -> Taper2@in0: input_straight_length, w, 0.5) In2;

 ml::LxTaper( bic -> Taper4@bic - [0, w2+w1,0]: output_taper_length, w2, w, 0.5) Taper5;
 ml::LxStraight( in0 -> Taper5@out0: output_straight_length, w, 0.5) Out2;

 ml::LxTaper( boc -> Taper5@bic: input_taper_length, w, w1, 0.5) Taper3;
 ml::LxStraight( out0 -> Taper3@in0: input_straight_length, w, 0.5) In3;
```

```
ml::setPort(In1 : in0 -> this@in0);
ml::setPort(Out1 : out0 -> this@out0);
ml::setPort(In2 : in0 -> this@in1);
ml::setPort(Out2 : out0 -> this@out1);
ml::setPort(In3 : in0 -> this@in2);
}

var pcl2_01 = ml::PC_layout_02(in0->block@org+[2300, 9250] : 1.1, 1.1, 6.9, 1000., 50.,1000.,
1000.);

mask::CSselect ("mcsWAVEGUIDE_ADS") ;
ml::pxConnectorSBendAdiabatic(from ->pcl2_01@out1, to->block@out45: 1500);
ml::pxConnectorSBendAdiabatic(from ->pcl2_01@out0, to->block@out46: 1600);

ml::pxConnectorSBendAdiabatic(from->pcl2_01@in0 , to->block@out18 :350);
ml::pxConnectorSBendAdiabatic(from->pcl2_01@in1 , to->block@out17 :300);
ml::pxConnectorSBendAdiabatic(from->pcl2_01@in2 , to->block@out16 :250);
//----------------------------------

//---------------------------------- Coupling alignment layout 2, case 2
var pcl2_02 = ml::PC_layout_02(in0->block@org+[2300, 9500] : 1.1, 2., 6., 1000., 250.,1000.,
1000.);

mask::CSselect ("mcsWAVEGUIDE_ADS") ;
ml::pxConnectorSBendAdiabatic(from ->pcl2_02@out1, to->block@out47: 1700);
ml::pxConnectorSBendAdiabatic(from ->pcl2_02@out0, to->block@out48: 1800);

ml::pxConnectorSBendAdiabatic(from->pcl2_02@in0 , to->block@out21 :500);
ml::pxConnectorSBendAdiabatic(from->pcl2_02@in1 , to->block@out20 :450);
ml::pxConnectorSBendAdiabatic(from->pcl2_02@in2 , to->block@out19 :400);
//----------------------------------

//---------------------------------- Coupling alignment layout 2, case 3
var pcl2_03 = ml::PC_layout_02(in0->block@org+[2300, 10000] : 1.1, 3., 7., 1000., 350.,1000.,
1000.);

mask::CSselect ("mcsWAVEGUIDE_ADS") ;
ml::pxConnectorSBendAdiabatic(from ->pcl2_03@out1, to->block@out49: 1900);
ml::pxConnectorSBendAdiabatic(from ->pcl2_03@out0, to->block@out50: 2000);
```

```
ml::pxConnectorSBendAdiabatic(from->pcl2_03@in0 , to->block@out24 :650);
ml::pxConnectorSBendAdiabatic(from->pcl2_03@in1 , to->block@out23 :600);
ml::pxConnectorSBendAdiabatic(from->pcl2_03@in2 , to->block@out22 :550);
//---------------------------------

///-------------------------  MMI-MZI(delay=2x1695um,2x2 MMI,50Ghz/0.4nm FSR, two heaters)
layout LioniX_MMI_MZI_01(double T=20)

{
  mask::setLayoutPort(this, "in0", "out0");
  var RoutingGridElectrical = Tech.getDefaultOrNewAutoRouterGrid(this, "Electrical",
"LioniX_MZIElectrical", 40, 40);
  var RoutingGrid = Tech.getDefaultOrNewAutoRouterGrid(this, "Optical",
"LioniX_MZIOptical", 40, 40);

   layout LioniX_MMI (wMMI = 10., LMMI2x2 = 230., wWG=1.1, LWG = 200, wt = 3.5, Lt =
200)
   {
  //MMI design-Peng - March 21, based on OptoDesigner manual (User_manual_ALL, page
1133)
  //Dimentions
  // wMMI: widht of the box body; LMMI2x2: the lenght of the box body;
  // wt: the taper end with, Lt: lenght of the taper waveguide lagnth
  // LWG: input straight waveguide length,

  // Box body of MMI
     mask::CSselect("mcsWAVEGUIDE_ADS");
     var boxmmi = ml::LxStraight(cin->[0] : LMMI2x2, wMMI);

  //inputs
     var taperInpBot = ml::LxTaper(bol->boxmmi@bil : Lt, wWG, wt);
     var inpBotStraight = ml::LxStraight(out0->taperInpBot@in0 : LWG, wWG);
     var inpBotArc = ml::LxBendS(out0->inpBotStraight@in0 : -127.);

     var taperInpTop = ml::LxTaper(bor->boxmmi@bir : Lt, wWG, wt);
     var inpTopStraight = ml::LxStraight(out0->taperInpTop@in0 : LWG, wWG);
     var inpTopArc = ml::LxBendS(out0->inpTopStraight@in0 : 127.);

  //outputs
     var taperOutBot = ml::LxTaper(bil->boxmmi@bol : Lt, wt, wWG);
```

```
    var outBotStraight = ml::LxStraight(last : LWG, wWG);
    var oupBotArc = ml::LxBendS(last : 127.);

    var taperOutTop = ml::LxTaper(bir->boxmmi@bor : Lt, wt, wWG);
    var outTopStraight = ml::LxStraight(last : LWG, wWG);
    var oupTopArc = ml::LxBendS(last : -127.);

  //set ports
    ml::setPort(inpTopArc : in0 -> this@in0);
    ml::setPort(oupTopArc : out0 -> this@out0);
    ml::setPort(inpBotArc : in0 -> this@in1);
    ml::setPort(oupBotArc : out0 -> this@out1);
  }

  mask::CSselect("mcsWAVEGUIDE_ADS");
  ml::LxArc(: 90,100.0,mcsGetWidth(),1.55,0.5) LxArc1;
  mask::CSselect("mcsWAVEGUIDE_ADS");
  ml::LxArc(: -90,100.0,mcsGetWidth(),1.55,0.5) LxArc2;
  mask::CSselect("mcsWAVEGUIDE_ADS");
  ml::LxArc(: -90,100.0,mcsGetWidth(),1.55,0.5) LxArc3;
  mask::CSselect("mcsWAVEGUIDE_ADS");
  ml::LxArc(: 90,100.0,mcsGetWidth(),1.55,0.5) LxArc4;
  mask::CSselect("mcsWAVEGUIDE_ADS");
  ml::LxArc(: -90,100.0,mcsGetWidth(),1.55,0.5) LxArc5;
  mask::CSselect("mcsWAVEGUIDE_ADS");
  ml::LxArc(in0->LxArc5@out0: 90,100.0,mcsGetWidth(),1.55,0.5) LxArc6;
  mask::CSselect("mcsWAVEGUIDE_ADS");
  ml::LxArc(: 90,100.0,mcsGetWidth(),1.55,0.5) LxArc7;
  mask::CSselect("mcsWAVEGUIDE_ADS");
  ml::LxArc(in0->LxArc7@out0: -90,100.0,mcsGetWidth(),1.55,0.5) LxArc8;
  mask::CSselect("mcsWAVEGUIDE_ADS");
  ml::LioniX_MMI(out0->LxArc5@in0, out1->LxArc1@in0: ) mmi1;
  mask::CSselect("mcsWAVEGUIDE_ADS");
  ml::LioniX_MMI(in0->LxArc8@out0, in1->LxArc4@out0: ) mmi3;
  mask::CSselect("mcsWAVEGUIDE_ADS");
  ml::LxPhaseModulator(in0->LxArc6@out0, out0->LxArc7@in0:
2000,2100,mcsGetWidth(),0,0,0,0,T,0.5,"yes") LxPhaseModulator1;
  mask::CSselect("mcsWAVEGUIDE_ADS");
  ml::LxPhaseModulator(in0->LxArc2@out0, out0->LxArc3@in0:
2000,2100,mcsGetWidth(),0,0,0,0,T,0.5,"yes") LxPhaseModulator2;
```

```
  mask::CSselect("mcsWAVEGUIDE_ADS");
  ml::LxStraight(out0->mmi1@in1: 100,mcsGetWidth(),0.5) LxStraight1;
  mask::CSselect("mcsWAVEGUIDE_ADS");
  ml::LxStraight(in0->mmi3@out1: 100,mcsGetWidth(),0.5) LxStraight3;
  mask::CSselect("mcsWAVEGUIDE_ADS");
  ml::LxStraight(in0->LxArc1@out0, out0->LxArc2@in0: 1695,mcsGetWidth(),0.5)
LxStraight4;
  mask::CSselect("mcsWAVEGUIDE_ADS");
  ml::LxStraight(in0->LxArc3@out0, out0->LxArc4@in0: 1695,mcsGetWidth(),0.5)
LxStraight5;
  mask::CSselect("mcsWAVEGUIDE_ADS");
  ml::LxStraight(out0->mmi1@in0: 100,mcsGetWidth(),0.5) LxStraight6;
  mask::CSselect("mcsWAVEGUIDE_ADS");
  ml::LxStraight(in0->mmi3@out0: 100,mcsGetWidth(),0.5) LxStraight7;

  // Stored element connections

  ml::setPort(LxStraight1 : in0->this@in0);
  ml::setPort(LxStraight6 : in0->this@in1);

  ml::setPort(LxStraight3 : out0->this@out0);
  ml::setPort(LxStraight7 : out0->this@out1);

  ml::setPort(LxPhaseModulator1 : dc1->this@dc0);
  ml::setPort(LxPhaseModulator1 : dc0->this@dc1);
  ml::setPort(LxPhaseModulator2 : dc1->this@dc2);
  ml::setPort(LxPhaseModulator2 : dc0->this@dc3);

  // Persist routing parameters into the MoML file
  this = Tech.populateAutoRouterInformation(this);

  // Set the promoted I/O ports domain
  mask::elementPortRegexSetDomain(this, "(in|out)([[:int:]])", OpticsDomain);

  mask::port2layout(&this);
}

ml::LioniX_MMI_MZI_01(in0->block@org+[7500, 10500] : ) mmimzi_01;

ml::pxConnectorSBendAdiabatic(from ->block@out26, to->mmimzi_01@in0: 300);
```

```
ml::pxConnectorSBendAdiabatic(from ->block@out25, to->mmimzi_01@in1: 350);
ml::pxConnectorSBendAdiabatic(from ->mmimzi_01@out1, to->block@out51: 500);
ml::pxConnectorSBendAdiabatic(from ->mmimzi_01@out0, to->block@out52: 550);

mask::CSselect("mcsLEAD");
ml::pxConnectorCurveDC(from ->block@dc33, to->mmimzi_01@dc1:);
ml::pxConnectorCurveDC(from ->block@dc21, to->mmimzi_01@dc0:);
ml::pxConnectorCurveDC(from ->block@dc31, to->mmimzi_01@dc3:);
ml::pxConnectorCurveDC(from ->block@dc23, to->mmimzi_01@dc2:);
//---------------------------------

///---------------------------------  1x2 splitter + delay line + 2x2 MMI(delay=2x1695um,2x2 MMI)
layout LioniX_SP1x2_MMI2x2_01(double T=20, delayline_Length=1695.)

{
  mask::setLayoutPort(this, "in0", "out0");
  var RoutingGridElectrical = Tech.getDefaultOrNewAutoRouterGrid(this, "Electrical",
"LioniX_MZIElectrical", 40, 40);
  var RoutingGrid = Tech.getDefaultOrNewAutoRouterGrid(this, "Optical",
"LioniX_MZIOptical", 40, 40);

   layout LioniX_MMI2x2 (wMMI = 22., LMMI2x2 = 417.65, LWG=100., wWG=1.1, wt=3.,
Lt=600., In1_location=2.72+3./2, In2_location=2.72+3.+6.04+3./2, Op1_location= 7.24+3./2,
Op2_location=7.24+3.+6.04+3/2)
   {

  // Box body of MMI
     mask::CSselect("mcsWAVEGUIDE_ADS");
     var boxmmi = ml::LxStraight(cin->[0] : LMMI2x2, wMMI);

  //inputs
     var taperInpBot = ml::LxTaper(boc->boxmmi@bil + [0, -In2_location, 0] : Lt, wWG, wt);
     var inpBotStraight = ml::LxStraight(out0->taperInpBot@in0 : LWG, wWG);
     var inpBotArc = ml::LxBendS(out0->inpBotStraight@in0 : 127./2-(6.04+3)/2);

     var taperInpTop = ml::LxTaper(boc->boxmmi@bil + [0, -In1_location, 0] : Lt, wWG, wt);
     var inpTopStraight = ml::LxStraight(out0->taperInpTop@in0 : LWG, wWG);
     var inpTopArc = ml::LxBendS(out0->inpTopStraight@in0 : -127./2+(6.04+3)/2);

  //outputs
```

```
    var taperOutBot = ml::LxTaper(bic->boxmmi@bol + [0, -Op2_location, 0] : Lt, wt, wWG);
    var outBotStraight = ml::LxStraight(last : LWG, wWG);
    var oupBotArc = ml::LxBendS(last : -127./2+(6.04+3)/2);

    var taperOutTop = ml::LxTaper(bic->boxmmi@bol + [0, -Op1_location, 0] : Lt, wt, wWG);
    var outTopStraight = ml::LxStraight(last : LWG, wWG);
    var oupTopArc = ml::LxBendS(last : 127./2-(6.04+3)/2);

  //set ports
    ml::setPort(inpTopArc : in0 -> this@in0);
    ml::setPort(oupTopArc : out0 -> this@out0);
    ml::setPort(inpBotArc : in0 -> this@in1);
    ml::setPort(oupBotArc : out0 -> this@out1);
  }

  mask::CSselect("mcsWAVEGUIDE_ADS");
  ml::LxArc(: 90,100.0,mcsGetWidth(),1.55,0.5) LxArc1;
  mask::CSselect("mcsWAVEGUIDE_ADS");
  ml::LxArc(: -90,100.0,mcsGetWidth(),1.55,0.5) LxArc2;
  mask::CSselect("mcsWAVEGUIDE_ADS");
  ml::LxArc(: -90,100.0,mcsGetWidth(),1.55,0.5) LxArc3;
  mask::CSselect("mcsWAVEGUIDE_ADS");
  ml::LxArc(: 90,100.0,mcsGetWidth(),1.55,0.5) LxArc4;
  mask::CSselect("mcsWAVEGUIDE_ADS");
  ml::LxArc(: -90,100.0,mcsGetWidth(),1.55,0.5) LxArc5;
  mask::CSselect("mcsWAVEGUIDE_ADS");
  ml::LxArc(in0->LxArc5@out0: 90,100.0,mcsGetWidth(),1.55,0.5) LxArc6;
  mask::CSselect("mcsWAVEGUIDE_ADS");
  ml::LxArc(: 90,100.0,mcsGetWidth(),1.55,0.5) LxArc7;
  mask::CSselect("mcsWAVEGUIDE_ADS");
  ml::LxArc(in0->LxArc7@out0: -90,100.0,mcsGetWidth(),1.55,0.5) LxArc8;
  mask::CSselect("mcsWAVEGUIDE_ADS");
  ml::LxYjunction(out0->LxArc5@in0, out1->LxArc1@in0: ) mmi1;
  mask::CSselect("mcsWAVEGUIDE_ADS");
  ml::LioniX_MMI2x2(in1->LxArc8@out0, in0->LxArc4@out0: ) mmi3;
  mask::CSselect("mcsWAVEGUIDE_ADS");
  ml::LxStraight(in0->LxArc6@out0, out0->LxArc7@in0: 500,mcsGetWidth(),0.5)
LxPhaseModulator1;
  mask::CSselect("mcsWAVEGUIDE_ADS");
```

```
  ml::LxStraight(in0->LxArc2@out0, out0->LxArc3@in0: 500,mcsGetWidth(),0.5)
LxPhaseModulator2;
  mask::CSselect("mcsWAVEGUIDE_ADS");
  ml::LxStraight(out0->mmi1@in0: 100,mcsGetWidth(),0.5) LxStraight1;
  mask::CSselect("mcsWAVEGUIDE_ADS");
  ml::LxStraight(in0->mmi3@out1: 100,mcsGetWidth(),0.5) LxStraight3;
  mask::CSselect("mcsWAVEGUIDE_ADS");
  ml::LxStraight(in0->LxArc1@out0, out0->LxArc2@in0:
delayline_Length,mcsGetWidth(),0.5) LxStraight4;
  mask::CSselect("mcsWAVEGUIDE_ADS");
  ml::LxStraight(in0->LxArc3@out0, out0->LxArc4@in0:
delayline_Length,mcsGetWidth(),0.5) LxStraight5;
//  mask::CSselect("mcsWAVEGUIDE_ADS");
//  ml::LxStraight(out0->mmi1@in0: 100,mcsGetWidth(),0.5) LxStraight6;
  mask::CSselect("mcsWAVEGUIDE_ADS");
  ml::LxStraight(in0->mmi3@out0: 100,mcsGetWidth(),0.5) LxStraight7;

  // Stored element connections

  ml::setPort(LxStraight1 : in0->this@in0);
 // ml::setPort(LxStraight6 : in0->this@in1);

  ml::setPort(LxStraight3 : out0->this@out0);
  ml::setPort(LxStraight7 : out0->this@out1);
  // Persist routing parameters into the MoML file
  this = Tech.populateAutoRouterInformation(this);

  // Set the promoted I/O ports domain
  mask::elementPortRegexSetDomain(this, "(in|out)([[:int:]])", OpticsDomain);

  mask::port2layout(&this);
}
ml::LioniX_SP1x2_MMI2x2_01(in0->block@org+[1500, 11500] : ) spmmi_01;
ml::pxConnectorSBendAdiabatic(from ->block@out27, to->spmmi_01@in0: 250);

ml::pxConnectorManhattan(from ->spmmi_01@out1 ,p0->block@org+[8000,13300,0] ,p1-
>block@org+[13700,13000,0],to->block@out54: 2);
ml::pxConnectorManhattan(from ->spmmi_01@out0 ,p0->block@org+[8100,13100,0] ,p1-
>block@org+[13600,12800,0],to->block@out53: 2);
```

```
//---------------------------------

///---------------------------------  1x2 splitter + delay line + 3x3 MMI(delay=2x1695um, 3x3MMI)
layout LioniX_SP1x2_MMI3x3_01(double T=20, delayline_Length=1695.)

{
  mask::setLayoutPort(this, "in0", "out0");
  var RoutingGridElectrical = Tech.getDefaultOrNewAutoRouterGrid(this, "Electrical",
"LioniX_MZIElectrical", 40, 40);
  var RoutingGrid = Tech.getDefaultOrNewAutoRouterGrid(this, "Optical",
"LioniX_MZIOptical", 40, 40);

   layout LioniX_MMI3x3 (wMMI = 22., LMMI2x2 = 695.5, LWG=100., wWG=1.1, wt=2.5,
Lt=600., In1_location=2.18+2.5/2, In2_location=2.18+2.5+5.07+2.5/2,
In3_location=2.18+2.5+5.07+2.5+5.07+2.5/2, Op1_location= In1_location,
Op2_location=In2_location, Op3_location=In3_location)
   {
   //Dimensions
   // wMMI: widht of the box body; LMMI2x2: the lenght of the box body;
   // wt: the taper end with, Lt: length of the taper waveguide
   // LWG: input straight waveguide length,
   // In1_location, In2_location, In3_location, Op1_location, Op2_location, O32_location: input
and output center location reference to the top of MMI box body

   // Box body of MMI
      mask::CSselect("mcsWAVEGUIDE_ADS");
      var boxmmi = ml::LxStraight(cin->[0] : LMMI2x2, wMMI);

   //inputs
      var taperInpBot = ml::LxTaper(boc->boxmmi@bil + [0, -In3_location, 0] : Lt, wWG, wt);
      var inpBotStraight = ml::LxStraight(out0->taperInpBot@in0 : LWG, wWG);
      var inpBotArc = ml::LxBendS(out0->inpBotStraight@in0 : 127./2-(2.5+5.07));

      var taperInpCt = ml::LxTaper(boc->boxmmi@bil + [0, -In2_location, 0] : Lt, wWG, wt);
      var inpCtStraight = ml::LxStraight(out0->taperInpCt@in0 : LWG+100., wWG);

      var taperInpTop = ml::LxTaper(boc->boxmmi@bil + [0, -In1_location, 0] : Lt, wWG, wt);
      var inpTopStraight = ml::LxStraight(out0->taperInpTop@in0 : LWG, wWG);
      var inpTopArc = ml::LxBendS(out0->inpTopStraight@in0 : -127./2+(2.5+5.07));
```

```
//outputs
   var taperOutBot = ml::LxTaper(bic->boxmmi@bol + [0, -Op3_location, 0] : Lt, wt, wWG);
   var outBotStraight = ml::LxStraight(last : LWG, wWG);
   var oupBotArc = ml::LxBendS(last : -127./2+(2.5+5.07));

   var taperOutCt = ml::LxTaper(bic->boxmmi@bol + [0, -Op2_location, 0] : Lt, wt, wWG);
   var outCtStraight = ml::LxStraight(last : LWG+100., wWG);

   var taperOutTop = ml::LxTaper(bic->boxmmi@bol + [0, -Op1_location, 0] : Lt, wt, wWG);
   var outTopStraight = ml::LxStraight(last : LWG, wWG);
   var oupTopArc = ml::LxBendS(last : 127./2-(2.5+5.07));

//set ports
   ml::setPort(inpTopArc : in0 -> this@in0);
   ml::setPort(inpCtStraight : in0 -> this@in1);
   ml::setPort(inpBotArc : in0 -> this@in2);
   ml::setPort(oupTopArc : out0 -> this@out0);
   ml::setPort(outCtStraight : out0 -> this@out1);
   ml::setPort(oupBotArc : out0 -> this@out2);
}

mask::CSselect("mcsWAVEGUIDE_ADS");
ml::LxArc(: 90,100.0,mcsGetWidth(),1.55,0.5) LxArc1;
mask::CSselect("mcsWAVEGUIDE_ADS");
ml::LxArc(: -90,100.0,mcsGetWidth(),1.55,0.5) LxArc2;
mask::CSselect("mcsWAVEGUIDE_ADS");
ml::LxArc(: -90,100.0,mcsGetWidth(),1.55,0.5) LxArc3;
mask::CSselect("mcsWAVEGUIDE_ADS");
ml::LxArc(: 90,100.0,mcsGetWidth(),1.55,0.5) LxArc4;
mask::CSselect("mcsWAVEGUIDE_ADS");
ml::LxArc(: -90,100.0,mcsGetWidth(),1.55,0.5) LxArc5;
mask::CSselect("mcsWAVEGUIDE_ADS");
ml::LxArc(in0->LxArc5@out0: 90,100.0,mcsGetWidth(),1.55,0.5) LxArc6;
mask::CSselect("mcsWAVEGUIDE_ADS");
ml::LxArc(: 90,100.0,mcsGetWidth(),1.55,0.5) LxArc7;
mask::CSselect("mcsWAVEGUIDE_ADS");
ml::LxArc(in0->LxArc7@out0: -90,100.0,mcsGetWidth(),1.55,0.5) LxArc8;
mask::CSselect("mcsWAVEGUIDE_ADS");
ml::LxYjunction(out0->LxArc5@in0, out1->LxArc1@in0: ) mmi1;
mask::CSselect("mcsWAVEGUIDE_ADS");
```

```
  ml::LioniX_MMI3x3(in2->LxArc8@out0, in0->LxArc4@out0: ) mmi3;
  mask::CSselect("mcsWAVEGUIDE_ADS");
  ml::LxStraight(in0->LxArc6@out0, out0->LxArc7@in0: 500,mcsGetWidth(),0.5)
LxPhaseModulator1;
  mask::CSselect("mcsWAVEGUIDE_ADS");
  ml::LxStraight(in0->LxArc2@out0, out0->LxArc3@in0: 500,mcsGetWidth(),0.5)
LxPhaseModulator2;
  mask::CSselect("mcsWAVEGUIDE_ADS");
  ml::LxStraight(out0->mmi1@in0: 100,mcsGetWidth(),0.5) LxStraight1;
  mask::CSselect("mcsWAVEGUIDE_ADS");
  ml::LxStraight(in0->LxArc1@out0, out0->LxArc2@in0:
delayline_Length,mcsGetWidth(),0.5) LxStraight4;
  mask::CSselect("mcsWAVEGUIDE_ADS");
  ml::LxStraight(in0->LxArc3@out0, out0->LxArc4@in0:
delayline_Length,mcsGetWidth(),0.5) LxStraight5;
//  mask::CSselect("mcsWAVEGUIDE_ADS");
//  ml::LxStraight(out0->mmi1@in0: 100,mcsGetWidth(),0.5) LxStraight6;
  mask::CSselect("mcsWAVEGUIDE_ADS");
  ml::LxStraight(in0->mmi3@out0: 100,mcsGetWidth(),0.5) LxStraight7;
  ml::LxStraight(in0->mmi3@out1: 100,mcsGetWidth(),0.5) LxStraight17;
  ml::LxStraight(in0->mmi3@out2: 100,mcsGetWidth(),0.5) LxStraight27;

  // Stored element connections

  ml::setPort(LxStraight1 : in0->this@in0);
 // ml::setPort(LxStraight6 : in0->this@in1);

  ml::setPort(LxStraight7 : out0->this@out0);
  ml::setPort(LxStraight17 : out0->this@out1);
  ml::setPort(LxStraight27 : out0->this@out2);
  // Persist routing parameters into the MoML file
  this = Tech.populateAutoRouterInformation(this);

  // Set the promoted I/O ports domain
  mask::elementPortRegexSetDomain(this, "(in|out)([[:int:]])", OpticsDomain);

  mask::port2layout(&this);
}

ml::LioniX_SP1x2_MMI3x3_01(in0->block@org+[3000, 12550] : ) spmmi_02;
```

```
ml::pxConnectorManhattan(from ->block@out28 ,p0->block@org+[1300,13700,0] ,p1-
>block@org+[2700,13500,0],to->spmmi_02@in0: 2);

ml::pxConnectorManhattan(from ->spmmi_02@out2 ,p0->block@org+[7350,13700,0] ,p1-
>block@org+[14000,13500,0],to->block@out55: 2);
ml::pxConnectorManhattan(from ->spmmi_02@out1 ,p0->block@org+[7250,13800,0] ,p1-
>block@org+[14100,13600,0],to->block@out56: 2);
ml::pxConnectorManhattan(from ->spmmi_02@out0 ,p0->block@org+[7150,13900,0] ,p1-
>block@org+[14200,13700,0],to->block@out57: 2);
//---------------------------------

//1. Set OBFN4x1.

// Menu: Element / User lib / Foundry / LioniX / ADS Platform / Composite /
LxOpticalBeamFormerNetwork4x1
var obfn = ml::LxOpticalBeamFormerNetwork4x1( in0 -> laser @ out0 + [1000,700] :
            /* MZR_input_pitch_um        = */ 250.0,
            /* MZR_output_pitch_um       = */ mask::CSattr("wgToHeater_pitch"),
            /* heater_Length_um          = */ 2000.0,
            /* input_pitch_um            = */ 250.0,
            /* output_pitch_um           = */ 250.0,
            /* distanceQ_from_dirCoupler_to_OBFN1x2 = */ 700.0);

//---------
//2. Set Optical Connectors.

//do not show the ports of the connectors in Viewer.
mask::docObj_lSet("hideport",1);

//--
// OBFN to SSC: ConnectorSine.

// Menu: Element / User lib / PDA-BB / Connector / pxConnectorSine
ml::pxConnectorSine( from -> laser @ out0
                , to   -> obfn @ in0 : );

// Menu: Element / User lib / PDA-BB / Connector / pxConnectorSine
for(int i=0; i<4; i++)
{
```

```
  int j=3+i;
  ml::pxConnectorSine( from -> obfn @ "out"+i , to -> block @ "out"+j : );
}

// OBFN to SSC: Connector U-shape
int nu=3;

for(int i=0; i<nu; i++)
{
  int j=i+1;
  var pp[nu], arc[nu], vectorDiff[nu], str[nu] ;
  double dp[nu];
  pp[i] = ml::Offset( cin -> obfn @ "in"+j : 0,0,180 );
  arc[i] = ml::BendPolar ( last : wfix(wwg),wR*((nu+1)-i),-90);
  vectorDiff[i]  = ml::diffPort ( arc[i] @ cout , obfn @ dc7 ); //printf("\n--\nvectorDiff[i]=",
vectorDiff[i], "\n--\n");
  dp[i] = abs(vectorDiff[i].x);
  str[i] = ml::pxStraight ( in0 -> arc[i] @ cout : dp[i] );
  ml::LxArc ( last : -90, wR*((nu+1)-i) );
  var nstr = ml::pxStraight ( last : 100 ); // to stabilize mode field after SBoffset.
  int k = 9-i ; // to connect to SSC port out7,8,9.
  ml::LxConnectorSine( from -> block @ "out"+k , to -> nstr @ in0 : );
}

//---------
//3. Set Electrical Connectors.

mask::CSselect("mcsLEAD");

// Menu: Element / User lib / Foundry / LioniX / ADS Platform / Connector /
LxConnectorCurveDC
//ml::LxConnectorCurveDC( from -> obfn @ dc0 , to -> block @ dc13 : );
//ml::LxConnectorCurveDC( from -> block @ dc13, to -> obfn @ dc9 : );
//ml::LxConnectorCurveDC( from -> block @ dc5, to -> obfn @ dc8 : );

#endif

// ---------------------------------------------------------------------
// DESIGN RULE CHECK AND EXPORT TO GDS
```

Bibliography

1. Cisco, “Cisco visual networking index: Forecast and Methodology 2018–2023”, 2021.
2. P. J. Winzer and D. T. Neilson, “From scaling disparities to integrated parallelism: a decathlon for a decade”, *Journal of Lightwave Technology*, vol. 35, pp. 1099–1115 2017.
3. M. Xu, M. He, H. Zhang, J. Jian, Y. Pan, X. Liu, L. Chen, X. Meng, H. Chen, Z. Li, X. Xiao, “High-performance coherent optical modulators based on thin-film lithium niobate platform”, *Nature communications*, vol. 6, no. 1, pp. 1-7, 2020.
4. K. Kikuchi, “Fundamentals of coherent optical fiber communications”, *Journal of Lightwave Technology,* vol. 34, pp. 157–179, 2016.
5. G. Raybon et al., “High symbol rate coherent optical transmission systems: 80 and 107 Gbaud”, *Journal of Lightwave Technology,* vol. 32, pp. 824–831, 2014.
6. ITU, "Measuring Digital Development- Facts and figures 2021” https://www.itu.int/en/ITU-D/Statistics/Documents/facts/FactsFigures2021.pdf
7. J. Carolan, C. Harrold, C. Sparrow, N. J. Russell, P. J. Shadbolt, N. Matsuda, M. Oguma, M. Itoh, G. D. Marshall, M. G. Thompson, J. C. F. Matthews, T. Hashimoto, and A. Laing, “Universal linear optics,” *Science*, vol. 349 no. 6249, pp. 711-716, 2015.
8. A. Rahim, S. Schwarz, J. Brunsand K. Petermann, “Terabit optical OFDM demultiplexer in SiP,” *Optical Fiber Communication Conference*, OSA, pp. JTh2A–28, 2013.
9. H. Yu, H. Yu, H. Chen and S. Xi, “All-optical OFDM demultiplexer based on an integrated silicon-on-insulator technique,” *IEEE Photonics Journal*, vol. 8, no. 1, pp. 1–7, 2016.
10. R. Schmogrow, M. Winter, D. Hillerkuss, B. Nebendahl, S. Ben-Ezra, J. Meyer, M. Dreschmann, M. Huebner, J. Becker, C. Koos, “Real-time OFDM transmitter beyond 100 Gbit/s,” *Optics express*, vol. 19, no. 13, pp. 12740–12749, 2011.
11. R. Basilio, M. Hasan, R. Guemri, F. Lucarz, and T. J. Hall, “Generalized Mach–Zehnder interferometer architectures for radio frequency translation and multiplication: suppression of unwanted harmonics by design,” *Optics Communications*, vol. 354, pp. 122–127, 2015.
12. M. Hasan, R. Maldonado-Basilio, and T. Hall, “Studies in an optical millimeter-wave generation scheme via two parallel dual-parallel MachZehnder modulators,” *Journal of Modern Optics*, vol. 62, no. 7, pp. 581–583, 2015.
13. X. Liu, Y. Yu, H. Tang, L. Xu, J. Dong, and X. Zhang, “Silicon-on-insulator-based microwave photonic filter with narrowband and ultrahigh peak rejection,” *Optics letters*, vol. 43, no. 6, pp. 1359–1362, 2018.
14. R. Maram, S. Kaushal, J. Azana, and L. R. Chen, “Recent trends and advances of silicon-based integrated microwave photonics,” *Photonics*, vol. 6, no. 1, 2019, p. 13.
15. M. Hasan, H. Nikkhah, and T. J. Hall, “Electro-optic up-conversion mixer amenable to photonic integration,” *Journal of Modern Optics*, vol. 62, no. 17, pp. 1405–1411, 2015.
16. H. Shen, M. H. Khan, L. Fan, L. Zhao, Y. Xuan, J. Ouyang, L. T. Varghese, and M. Qi, “Eight-channel reconfigurable microring filters with tunable frequency, extinction ratio and bandwidth,” *Optics express*, vol. 18, no. 17, pp. 18067–18076, 2010.

17. S. Song, S. X. Chew, X. Yi, L. Nguyen, and R. A. Minasian, "Tunable single-passband microwave photonic filter based on integrated optical double notch filter," *Journal of Lightwave Technology*, vol. 36, no. 19, pp. 4557–4564, 2018.
18. D. A. Miller, "Perfect optics with imperfect components," *Optica*, vol. 2, no. 8, pp. 747–750, 2015.
19. M. Hasan, P. Liu, T. J. Hall *et al.*, "Towards a universal RF photonic integrated circuit architecture for microwave applications," IEEE *Progress in Electromagnetic Research Symposium (PIERS)*, pp. 84–87, 2016.
20. K. Takiguchi and T. Miwa, "Integrated-optic OFDM signal multiplexer composed of optical IFFT circuit," *Electronics Letters*, vol. 51, no. 6, pp. 505–506, 2015.
21. E. Palushani, H. H. Mulvad, D. Kong, P. Guan, M. Galili, and L. K. Oxenløwe, "All-optical OFDM demultiplexing by spectral magnification and band-pass filtering," *Optics express*, vol. 22, no. 1, pp. 136–144, 2014.
22. H. Yamazaki, T. Saida, T. Goh, S. Mino, M. Nagatani, H. Nosaka, and K. Murata, "Dual-carrier dual-polarization IQ modulator using a complementary frequency shifter," *IEEE Journal of Selected Topics in Quantum Electronics*, vol. 19, no. 6, pp. 175–182, 2013.
23. T. J. Hall and M. Hasan, "Universal discrete fourier optics RF photonic integrated circuit architecture," *Optics express*, vol. 24, no. 7, pp. 7600–7610, 2016.
24. T. J. Hall and M. Hasan, "Universal photonic integrated circuit architecture: The discrete Fourier Transform case," IEEE *Photonics North (PN)*, pp. 1–1, 2016.
25. K. Takiguchi, T. Kitoh, M. Oguma, and H. Takahashi, "Integrated-optic OFDM demultiplexer using MMI coupler-based optical DFT circuit," *IEEE OFC*, pp. 1–3, 2012.
26. T. Naganuma and H. Uenohara, "Analytical investigation of adaptive dispersion control of optical fractional OFDM circuit with phase shift," *Optical Sensors*, pp. JTu4A–25, 2017.
27. A. Rahim, S. Schwarz, J. Bruns, S. J. Ahmed, C. G. Schaffer, and K. Petermann, "16-channel O-OFDM demultiplexer in silicon photonics," *IEEE OFC*, pp. 1–3, 2014.
28. S. Schwarz, C. G. Schaeffer, A. Rahim, J. Bruns, and K. Petermann, "All-optical discrete Fourier transform for OFDM demultiplexing and its sensitivity to phase errors," *IEEE International Conference on NuSOD,* pp. 135–136, 2012.
29. J. Zhou, "All-optical discrete fourier transform based on multimode interference couplers," *IEEE Photonics Technology Letters*, vol. 22, no. 15, pp. 1093–1095, 2010.
30. K. Takiguchi, T. Kitoh, A. Mori, M. Oguma, and H. Takahashi, "Integrated-optic OFDM demultiplexer using slab star coupler based optical DFT circuit," *IEEE European Conference and Exhibition on Optical Communication*, pp. 1–3, 2010.
31. J. Zhou and M. Zhang, "All-optical discrete sine transform and discrete cosine transform based on multimode interference couplers," *IEEE Photonics Technology Letters*, vol. 22, no. 5, pp. 317–319, 2010.
32. G. Cincotti, "Generalized fiber Fourier optics," *Optics letters*, vol. 36, no. 12, pp. 2321–2323, 2011.

33. G. Cincotti, “What else can an AWG do?” *Optics exp.*, vol. 20, no. 26, pp. 288–298, 2012.
34. S. Schwarz, C. Schaffer, A. Rahim, J. Bruns, and K. Petermann, “Comparison of phase error sensitivities of all-optical discrete Fourier transforms for OFDM demultiplexing,” *Optical and Quantum Electronics*, vol. 45, no. 7, pp. 775–781, 2013.
35. S.-J. Lim and J.-K. K. Rhee, “System tolerance of all-optical sampling OFDM using AWG discrete Fourier Transform,” *Optics express*, vol. 19, no. 14, pp. 13590–13597, 2011.
36. M. Hasan, R. Guemri, R. Maldonado-Basilio, F. Lucarz, T. Hall, “Theoretical analysis and modeling of a photonic integrated circuit for frequency 8-tupled and 24-tupled millimeter wave signal generation,” *Optics letters*, vol. 39, no. 24, pp. 6950–6953, 2014.
37. M. Hasan and T. J. Hall, “Dual-function photonic integrated circuit for frequency octo-tupling or single-side-band modulation,” *Optics lett.*, vol. 40, no. 11, pp. 2501–2504, 2015.
38. D. Korn, R. Palmer, H. Yu, L. Alloatti, M. Baier, R. Schmogrow, W. Bogaerts, G. Lepage, “Silicon-organic hybrid IQ modulator using the linear electro-optic effect for transmitting 16QAM at 112 Gbit/s,” *Optics express*, vol. 21, no. 11, pp. 13219–13227, 2013.
39. J. Li, Z. Liu, Y. Tu, S.-T. Ho, I. W. Jung, L. E. Ocola, and B. W. Wessels, “Photonic crystal waveguide electro-optic modulator with a wide bandwidth,” *Journal of lightwave technology*, vol. 31, no. 10, pp. 1601–1607, 2013.
40. W. H. Pernice, C. Xiong, F. J. Walker, and H. X. Tang, “Design of a silicon integrated electro-optic modulator using ferroelectric BaTiO3 films,” *IEEE Photonics Technology Letters*, vol. 26, no. 13, pp. 1344–1347, 2014.
41. R. Halir, P. J. Bock, P. Cheben, A. Ortega-Monux, C. Alonso-Ramos, J. H. Schmid, J. Lapointe, D.-X. Xu, I. M. Fernandez, “Waveguide sub-wavelength structures: A review of principles and applications,” *Laser & Photonics Reviews*, vol. 9, no. 1, pp. 25–49, 2015.
42. S. Abdul-Majid, R. Maldonado-Basilio, C. Lei, H. Awad, I. Hasan, N. Y. Winnie, and T. J. Hall, “Performance analysis of a photonic integrated interferometer circuit based on lSOI,” *Optical and Quantum Electronics*, vol. 47, no. 7, pp. 1965–1971, 2015.
43. E. Kleijn, E. M. Van Vliet, D. Pustakhod, M. K. Smit, and X. J. Leijtens, “Amplitude and phase error correction algorithm for 3x3 MMI based Mach–Zehnder Interferometers,” *Journal of Lightwave Technology*, vol. 33, no. 11, pp. 2233–2239, 2015.
44. A. O. Mufutau, F. P. Guiomar, M. A. Fernandes, A. Oliveira, and P. P. Monteiro, “Demonstration of a hybrid optical fiber–wireless 5G fronthaul coexisting end-to-end 4G networks,” *Journal Optical Communications & Networking*, vol.12, no.3, pp. 72–78, 2020.
45. P. J. Winzer, D. T. Neilson, and A. R. Chraply, “Fiberoptic transmission and networking: previous 20 and next 20 years,” Optics express, vol. 26, no. 18, pp. 24 190– 24 239, 2018.
46. A. S. Raja, S. Lange, M. Karpov, K. Shi, X. Fu, R. Behrendt, D. Cletheroe, A. Lukashchuk, I. Haller, F. Karinou *et al.*, “Ultrafast optical circuit switching for data centers using integrated soliton microcombs,” *Nature communications*, vol. 12, no. 1, pp. 1–7, 2021.
47. N. Margalit, C. Xiang, S. M. Bowers, R. Blum, and J. E. Bowers, “Perspective on the future of silicon photonics and electronics,” *Applied Phys. Lett.*, vol. 118, no. 22, p. 220501, 2021.

48. Y. Yue, Q. Wang, and J. Anderson, “Experimental investigation of 400 Gb/s data center interconnect using unamplified high-baud-rate and high-order QAM single-carrier signal,” *Applied Sciences*, vol. 9, no. 12, p. 2455, 2019.
49. L. Cheng, S. Aditya, and A. Nirmalathas, “An exact analytical model for dispersive transmission in microwave fiberoptic links using Mach-Zehnder external modulator,” *IEEE Photonics Technology Letters*, vol. 17, no. 7, pp. 1525–1527, 2015.
50. L. Duvillaret, S. Rialland, and J. Coutaz, “Electro-optic sensors for electric field measurements-theoretical comparison among different modulation techniques,” *JOSA B*, vol. 19, no. 11, pp. 2692–2703, 2013.
51. H.-P. Lo, T. Ikuta, and H. Takesue, “Electro-optic modulators for photonic quantum information processing,” *Quantum and Nonlinear Optics*, vol. 11195, p. 111950P, 2019.
52. X. Xie, J. Khurgin, J. Kang, and F.-S. Chow, “Linearized Mach Zehnder intensity modulator,” *IEEE Photonics Technology Letters*, vol. 15, no. 4, pp. 531–533, 2014.
53. M. Gimeno-Segovia, H. Cable, G. J. Mendoza, P. Shadbolt, J. W. Silverstone, J. Carolan, M. G. Thompson and T. Rudolph, “Relative multiplexing for minimizing switching in linear-optical quantum *computing*” *New Journal of Physics*, vol. 19, no. 6, p. 063013, 2017.
54. R. Hamerly, L. Bernstein, A. Sludds and D. Englund, “Large-scale optical neural networks based on photoelectric multiplication,” *Physical Review X*, vol. 9, no. 2, p. 021032, 2019.
55. M. J. Deen and P. K. Basu, *Silicon photonics: fundamentals and devices*. John Wiley & Sons, vol. *44,* 2012.
56. M. Smit, K. Williams, and J. van der Tol, “Past, present, and future of InP-based photonic integration,” *APL Photonics*, vol. 4, no. 5, p. 050901, 2019.
57. D. J. Moss, R. Morandotti, A. L. Gaeta, and M. Lipson, “CMOS-compatible platforms based on silicon nitride and hydex for nonlinear optics,” *Nature photonics*, vol. 7, no. 8, pp. 597–607, *2018*.
58. T.-J. Lu, M. Fanto, H. Choi, P. Thomas, J. Steidle, S. Mouradian, W. Kong, D. Zhu, H. Moon, K. Berggren *et al.*, “Aluminum nitride integrated photonics platform for the ultraviolet to visible *spectrum*,” *Optics express*, vol. 26, no. 9, pp. 11 147–11 160, 2018.
59. D. M. Lukin, C. Dory, M. A. Guidry, K. Y. Yang, S. D. Mishra, R. Trivedi, M. Radulaski, S. Sun, D. Vercruysse, G. H. Ahn *et al.*, “4H-silicon-carbide-on-insulator for integrated quantum and nonlinear photonics,” *Nature Photonics*, vol. 14, no. 5, pp. 330–334, 2020.
60. T. Ding, Y. Zheng, and X. Chen, “On-chip solc-type polarization control and wavelength filtering utilizing periodically poled lithium niobate on insulator ridge waveguide,” *Journal of Lightwave Technology*, vol. 37, no. 4, pp. 1296–1300, 2019.
61. B. Desiatov, A. Shams-Ansari, M. Zhang, and C. Wang, “Ultra-low-loss integrated visible photonics using thin-*film* lithium niobate,” *Optica*, vol. 6, no. 3, pp. 380–384, 2019.
62. M. Xu, M. He, H. Zhang, J. Jian, Y. Pan, X. Liu, L. Chen, X. Meng, H. Chen, Z. Li *et al.*, “High-performance coherent optical modulators based on thin-film lithium niobate platform,” *Nature communications*, vol. 11, no. 1, pp. 1–7, 2020.

63. G. T. Reed, G. Mashanovich, F. Y. Gardes, and D. Thomson, “Silicon optical modulators,” *Nature photonics*, vol. 4, *no*. 8, pp. 518–526, 2018.
64. G. Roelkens, L. Liu, R. Jones, B. Koch, and J. Bowers, “III-V/silicon photonics for on-chip optical interconnects,” *Laser & Photonics Reviews*, vol. 4, no. 6, pp. 751–779, 2020.
65. O. Marshall, M. Hsu, Z. Wang, B. Kunert, and C. Koos, “Heterogeneous integration on silicon photonics,” *Proceedings of the IEEE*, vol. 106, no. 12, pp. 2258–2269, 2018.
66. A. E. Kaloyeros, Y. Pan, J. Goff, and B. Akles, “Silicon nitride and silicon nitride-rich thin film technologies: state of-the-art processing technologies, properties, and applications,” *ECS Journal of Solid State Science & Technology*, vol. 9, no. 6, p. 063006, 2020.
67. A. F. Braña, H. Gupta, R. K. Bommali, P. Srivastava, S. Ghosh, and R. P. Casero, “Enhancing efficiency of CSI solar cell by coating nano structured silicon rich silicon nitride films,” *Thin Solid Films*, vol. 662, pp. 21–26, 2018.
68. D. Blumenthal, R. Heideman, D. Geuzebroek, A. Leinse, and C. Roeloffzen, “Silicon nitride in silicon *photonics*,” *Proceedings of IEEE*, vol. 106, no. 12, pp. 2209–2231, 2018.
69. X. Zhang, B. A. Bell, C. Xiong, P. H. Leong, and B. J. Eggleton, “Integrated silicon nitride time-bin entanglement *circuits*,” *Optics letters*, vol. 43, no. 15, pp. 3469– 3472, 2018.
70. L. Chang, N. Volet, M. Zervas, J. D. Peters, E. J. Stanton, Y. Li, and J. E. Bowers, “Hybrid integration of lithium niobate and silicon nitride waveguides for wafer-scale photonic integrated circuits on silicon,” *Optics letters*, vol. 42, no. 4, pp. 803–806, 2017.
71. H. Lu, W. Qiu, C. Guyot, G. Ulliac, J.-M. Merolla, F. Baida, and M.-P. Bernal, “Optical and RF characterization of a lithium niobate photonic crystal modulator,” *IEEE Photonics Technology Letters*, vol. 26, no. 13, pp. 1332–1335, 2014.
72. K. Alexander, J. P. George, J. Verbist, K. Neyts, B. Kuyken, D. Van Thourhout, and J. Beeckman, “Nanophotonic Pockels modulators on a silicon nitride platform,” *Nature communications*, *vol*. 9, no. 1, pp. 1–6, 2018.
73. S. Jin, L. Xu, H. Zhang, and Y. Li, “LiNbO3 thin-film modulators using silicon nitride surface ridge waveguides,” *IEEE Photonics Techn. Lett.*, vol. 28, no. 7, pp. 736– 739, 2016.
74. K. K. Mehta, G. N. West, and R. J. Ram, “SiN-on-LiNbO3 integrated optical modulation at visible wavelengths,” *IEEE Conference on Lasers and Electro-Optics*, pp. 1–2, 2017.
75. A. N. R. Ahmed, S. Shi, A. J. Mercante, and D. W. Prather, “High-performance racetrack resonator in silicon nitride-thin film lithium niobate hybrid platform,” *Optics express*, vol. 27, no. 21, pp. 30741–*30751*, 2019.
76. A. N. R. Ahmed, S. Nelan, S. Shi, P. Yao, A. Mercante, and D. W. Prather, “Subvolt electro-optical modulator on thin film lithium niobate and silicon nitride hybrid platform,” *Optics letters*, vol. 45, no. 5, pp. 1112–1115, 2020.
77. A. Boes, B. Corcoran, L. Chang, J. Bowers, and A. Mitchell, “Status and potential of lithium niobate on insulator (LNOI) for photonic integrated circuits,” *Laser & Photonics Reviews*, vol. 12, no. 4, p. 1700256, 2018.

78. A. J. Mercante, S. Shi, P. Yao, L. Xie, R. M. Weikle, and D. W. Prather, "Thin film lithium niobate electro-optic modulator with terahertz operating bandwidth," *Optics express*, vol. 26, no. 11, pp. 14810–14816, 2018.
79. N. Boynton, H. Cai, M. Gehl, S. Arterburn, C. Dallo, A. Pomerene, A. Starbuck, D. Hood, and D. Trotter, "A heterogeneously integrated silicon photonic/lithium niobate travelling wave electro-optic *modulator*," *Optics express*, vol. 28, no. 2, pp. 1868–1884, 2020.
80. B. Dong, X. Luo, S. Zhu, T. Hu, M. Li, D. Hasan, L. Zhang, S. J. Chua, J. Wei, Y. Chang, "Thermal annealing study of the mid-infrared aluminum nitride on insulator (AlNoI) photonics platform," *Optics express*, vol. 27, no. 14, pp. 19815–19826, 2019.
81. H. Han, L. Cai, and H. Hu, "Optical and structural properties of single-crystal lithium niobate thin film," *Optical Materials*, vol. 42, pp. 47–51, 2016.
82. A. Rao, A. Patil, J. Chiles, M. Malinowski, S. Novak, P. Rabiei, and S. Fathpour, "Heterogeneous microring and mach-zehnder modulators based on lithium niobate and chalcogenide glasses on silicon," *Optics express*, vol. 23, no. 17, pp. 22 746–22 752, 2015.
83. M. Zhang, C. Wang, D. Zhu, and M. Lončar, "Integrated lithium niobate electro-optic modulators: when performance meets *scalability*" *Optica*, vol. 8, no. 5, pp. 652– 667, 2021.
84. C. Wang, M. Zhang, B. Stern, M. Lipson, and M. Lončar, "Nanophotonic lithium niobate electro-optic modulators," *Optics express*, vol. 26, no. 2, pp. 1547–1555, 2018.
85. Y. Li *et al*., "On-chip photonic microsystem for optical signal processing based on silicon and silicon nitride platforms," *Advanced Optical Technologies*, vol. 7, pp. 81-101, 2018.
86. M. Kita, H. lin, A. Agarwal, K. Richardson, I. Luzinov, T. Gu, and J. Hu, "On-chip infrared spectroscopic sensing: Redefining the benefits of scaling," *IEEE Journal of Selected Topics in Quantum Electronics*, vol. 23, pp. 340-349, 2017.
87. E. Heidari, X. Xu, Chi-Jui Chung, and R. T. Chen, "On-chip Fourier transform spectrometer on silicon-on-sapphire," *Optics Letter*, vol. 44, pp. 2883-2886, 2019.
88. X. Ma, M. Li and J. He, "CMOS-compatible spectrometer based on echelle diffraction grating and MSM photodetector array," *IEEE Photonics Journal*, vol. 5, pp. 807-809, 2013.
89. C. Xiang, P.A. Morton, J. Khurgin, C. Morton, and J. E. Bowers, "Widely tunable Si3N4 triple-ring and quadring resonator laser reflectors and filters," *IEEE International conference on group IV photonics*, *Cancun*, Mexico, pp. 1-2, 2018.
90. Roeloffzen et. al. "Low-loss Si3N4 TriPleX optical waveguides: technology and applications overview", *IEEE J. S. Topics Quantum Electronics*, vol. 24, p. 4400321, 2018.
91. Y. Xie and A. Lowery, "Picosecond optical pulse processing using a THz-bandwidth reconfigurable photonic *integrated* circuit," *Nanophotonics*, vol. 7, pp. 837-852, 2018.
92. Kleijn et. al., "Technological verification of size-optimized 160-channel silicon nitride-based AWG-spectrometer", *Applied Physics B*, vol. 125, article no. 88, 2019.
93. B. E. Little, T. Murphy, 'Design rules for maximally flat wavelength-insensitive optical power dividers using Mach–Zehnder structures', *IEEE Photonics Technology Lett*er, vol. 9, no. 12, pp. 1607-1609, 1999.